Engineering in the Optimization of Resolution of Nanohole Arrays in Metal Films for Refractive Index Sensing

by

Gabriela Andrea Cervantes Téllez
B.Sc., Instituto Tecnológico de Estudios Superiores de Monterrey, 2009

A Thesis Submitted in Partial Fulfillment
of the Requirements for the Degree of

MASTER OF APPLIED SCIENCE

in the Department of Electrical and Computer Engineering

Supervisory Committee

Engineering in the Optimization of Resolution of Nanohole Arrays in Metal Films for Refractive Index Sensing

by

Gabriela Andrea Cervantes Téllez
B.Sc., Instituto Tecnológico de Estudios Superiores de Monterrey, 2009

Supervisory Committee

Dr. Reuven Gordon (Department of Electrical and Computer Engineering)
Supervisor

Dr. Tao Lu (Department of Electrical and Computer Engineering)
Departmental Member

Dr. Rodney Herring (Department of Mechanical Engineering)
Outside Member

Abstract

Supervisory Committee

Dr. Reuven Gordon (Department of Electrical and Computer Engineering)
Supervisor

Dr. Tao Lu (Department of Electrical and Computer Engineering)
Departmental Member

Dr. Rodney Herring (Department of Mechanical Engineering)
Outside Member

Label free detection techniques such as surface plasmon resonance, carbon nanotubes, nanowires, and interferometry have been progressing rapidly for biosensing applications. Surface plasmon resonance is considered one of the most promising label free optical techniques. The use of nanohole arrays in a metal film allows for extraordinary transmission and has been motivated by their application as biosensors. Nanohole arrays present several advantages like smaller foot print, dense integration, lower limits of detection, and collinear optical detection.

This thesis presents the design parameters for the optimization of sensitivity and resolution of nanohole arrays for refractive index sensing. A systematic study is provided of the influence of the nanohole array periodicity, diameter, and gold thickness. Focused ion beam was used to fabricate the nanohole arrays. A microfluidic device with a set of embedded nanohole arrays was developed and used to measure the sensing characteristics. The results are encouraging for potential future biosensing tests.

Table of Contents

List of Figures

Acknowledgments

I would like to express my deepest gratitude and appreciation to my supervisor Dr. Reuven Gordon for his support and guidance throughout the length of this program and for giving me the opportunity to work with him.

I would like to thank to Dr. Elaine Humphrey and Adam Schuetze for their guidance and support in the nanofabrication process.

I would like to thank my current and past colleagues and friends for their support and fun provided along my studies that made the past years memorable.

I am also grateful for the financial support from the Natural Science and Engineering Research Council of Canada (NSERC).

Finally, I wish to express my love and gratitude to my parents and my sister for their love and encouragement in every stage of my life.

Dedication

To my parents

Glossary

Common Abbreviations

SP	Surface plasmon
SPR	Surface plasmon resonance
SPP	Surface plasmon polariton
LSP	Localized surface plasmon
EOT	Extraordinary optical transmission
RIU	Refractive index unit
FDTD	Finite difference time domain
FIB	Focused ion beam
SEM	Scanning electron microscopy
EDX	Energy dispersive X-ray spectroscopy
BSA	Bovine serum albumin
PDMS	Polydimethyl dimethylsiloxane
TIR	Total internal reflection
PMMA	Polymethyl methacrylate
PML	Perfectly matched layer
SNR	Signal to noise ratio
ATR	Attenuated total reflection
BSA	Bovine serum albumin
MUA	Mercaptoundecanoic acid
SAM	Self-assembled monolayer

Chapter 1: Introduction

Nanotechnology is the branch of technology that deals with dimensions of less than 100 nanometers, especially with the study of manipulating matter in the scale of several atoms. Over the past few decades the concept of nanotechnology has been earnestly applied to chemical and biological problems. For example, much interest has been focused on the development of lab-on-chip nanohole sensors [1].

Surface plasmons (SPs) are surface bound electromagnetic waves formed at the interface between a metal and a dielectric, which was first predicted in 1950s by R.H. Ritchie [2]. They are categorized into two classes: surface plasmons polaritons (SPPs) and localized surface plasmons (LSPs) [3]. SPs are very sensitive to near surface dielectric constant (index of refraction) and the use of nanohole arrays is well suited to the detection of surface binding events. This is the key physical principle of SP sensors [4]. Specific opportunities for nanohole arrays as sensors are the improvement in sensitivity and detection limits.

The present research work mainly focuses in the resolution optimization of nanohole arrays for refractive index sensing by increasing the sensitivity with modifications to the hole array parameters and by reducing the noise of the system. Such structures have been analyzed theoretically and fabricated using focused ion beam (FIB). Intensity measurements using the nanostructure are used for characterization. Details of experimental results to measure sensing characteristics are provided.

1.1 Organization of the thesis

Chapter 2 provides a brief account of the general theory behind SPs, the origin of extraordinary optical transmission (EOT), and the phenomenon of enhanced light transmission through nanohole arrays.

Chapter 3 gives a description of milling issues faced during the fabrication of nanohole arrays using FIB. A fabrication process of the microfluidic device with a set of embedded nanohole arrays and finite difference time domain simulations will be presented.

Chapter 4 describes the development of a nanohole sensor for refractive index change in metal-dielectric interference. A description of the optical setup will be presented as long with the optimization for resolution. Evaluation of test results from intensity measurements will be discussed.

Chapter 5 summarizes the work done and outlines the possible future research directions.

Chapter 2: Background theory

2.1 Surface plasmon resonance

Surface plasmons (SPs) are collective oscillations of free electron gas density that propagate along the planar interface between two media with dielectric constants of opposite sign, for instance, a metal and a dielectric [5]. They are two varieties of SPs, the localized surface plasmons (LSPs) and the surface plasmons polaritons (SPPs).

When SPs are localized to a particle of a size smaller than the wavelength of the light like a metal nanoparticle this is named LSPs (Figure 2.1). By solving the boundary conditions at the metal nanoparticle surface, a resonant condition can be found with a dramatic local field enhancement. This local field enhancement near a metal nanoparticle is called localized surface plasmon resonance (LSPR) [6].

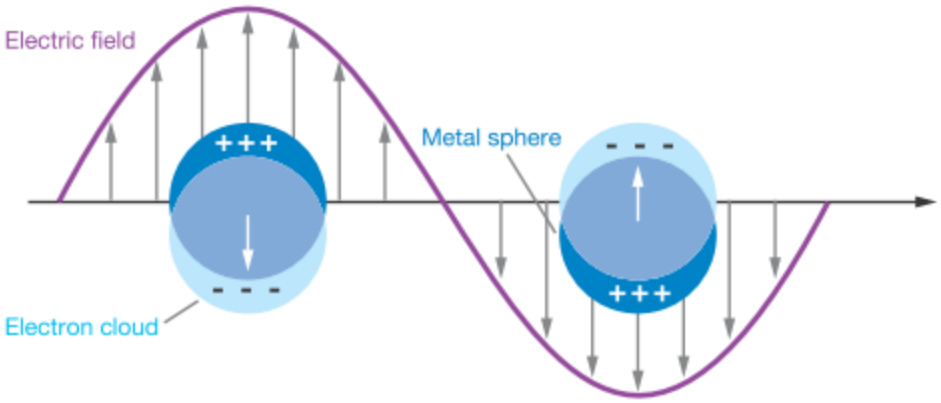

Figure 2.1 Illustration of the localized surface plasmon resonance effect [7].

SPPs are defined like electromagnetic waves that are confined to the vicinity of an interface between a metal and a dielectric. SPPs can be resonantly excited by p-polarized light that decays exponentially into the metal and towards the dielectric in a normal direction to the interface until the energy is lost via absorption in metal or radiation in free space [8] (Figure 2.2).

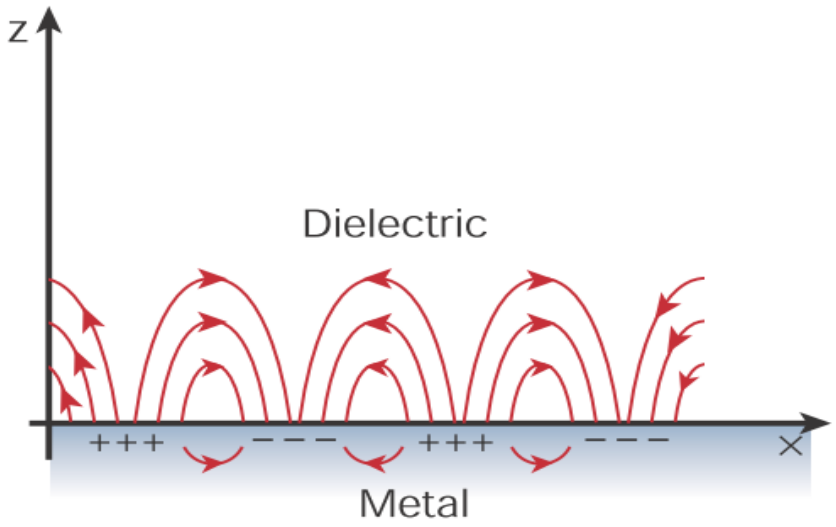

Figure 2.2 Surface plasmon polaritons that are confined near vicinity at the interface between a metal and a dielectric material. Surface plasmon waves decay along the z direction and propagates in the x direction [9].

In order to achieve plasmon excitation, a matching condition between the incident light and the SP wave vector is required:

$$k_{light} = k_{SP} \tag{2.1}$$

On a semi-infinite planar boundary between a metal and a dielectric, the wave vector is given by the following expression:

$$k_{SP} = \frac{\omega}{c}\sqrt{\frac{\varepsilon_m \varepsilon_d}{\varepsilon_m + \varepsilon_d}} \tag{2.2}$$

where ω is the angular frequency, c is the velocity of the light in free space, ε_m is the relative permittivity of the metal $(\varepsilon_m = \varepsilon_{mr} + i\varepsilon_{mi})$, and ε_d is the relative permittivity of the dielectric. The wave vector (Equation 2.2) is sensitive to the change on the index of refraction of the dielectric medium local to the surface, which makes it well-suited for surface-binding tests [10].

In order for SPs to exist the real part of the dielectric constant of the metal must be negative. For ε_m to be negative, ω has to be less than the plasma frequency. Metals such as gold, silver, and aluminum exhibit a negative real part of permittivity in the visible and near-infrared regions of the spectrum. The real part of k_{SP} is plotted in Figure 2.3. Since k_{SP} is real and greater than the wave vector of light $\left(k_o = \omega / c\right)$ in the dielectric, special momentum matching techniques needs to be adapted to coupled light and SPPs together.

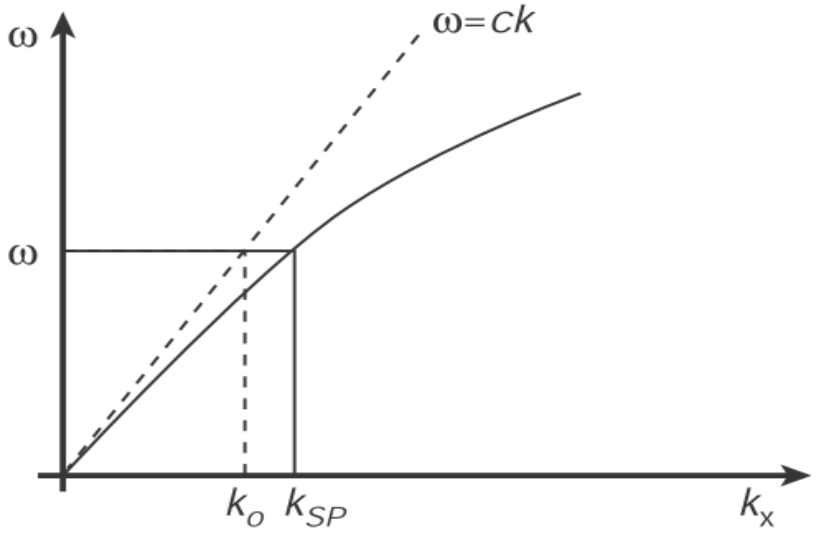

Figure 2.3 Dispersion relation of surface plasmons polaritons at a metal-dielectric interface. The dotted line corresponds to the light line in air, at low frequencies the surface mode approaches the light line asymptotically, and the fields associated with the mode expand into the vacuum [9].

2.2 Excitation of surface plasmons polaritons

The optical excitation of SPPs includes the attenuated total reflection (ATR) method where a light beam is first propagated through a prism (with permittivity ε_d) and then is reflected on a glass and metal interface, with a wave vector component parallel to the metal surface given by

$$k_x = \frac{\omega}{c}\sqrt{\varepsilon_o}\sin\theta \tag{2.3}$$

where θ is the angle between the surface normal and incoming light. In this way, SPPs with propagation constants between the light lines of air and the higher index dielectric can be excited (Figure 2.4). Matching between the wave vector of the incoming photons and the SPP wave vector at the metal and air interface can be achieved by tuning θ [11].

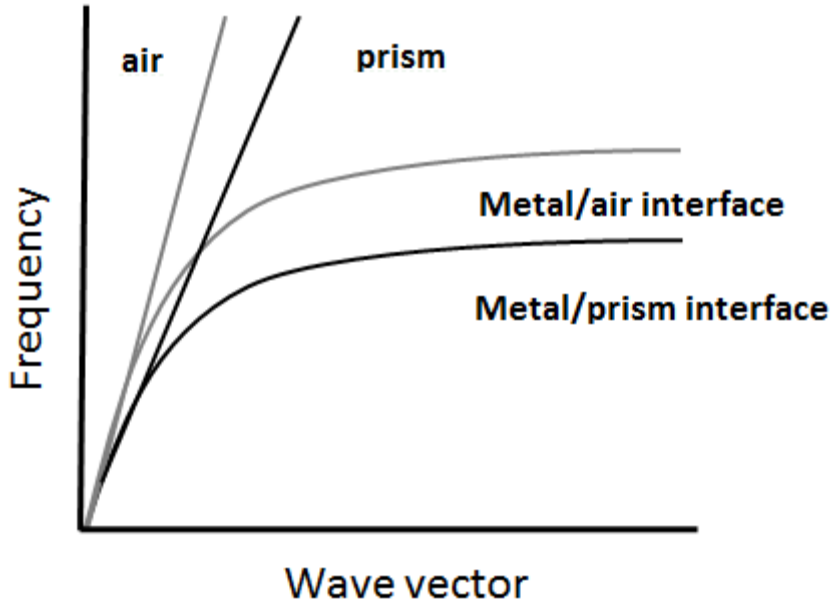

Figure 2.4 Prism coupling and surface plasmon polariton dispersion.

Two configurations have been proposed to excited SPPs by means of an ATR setup, one of them is the Otto configuration [12] and the other is the Kretschmann configuration [13] (Figure 2.5).

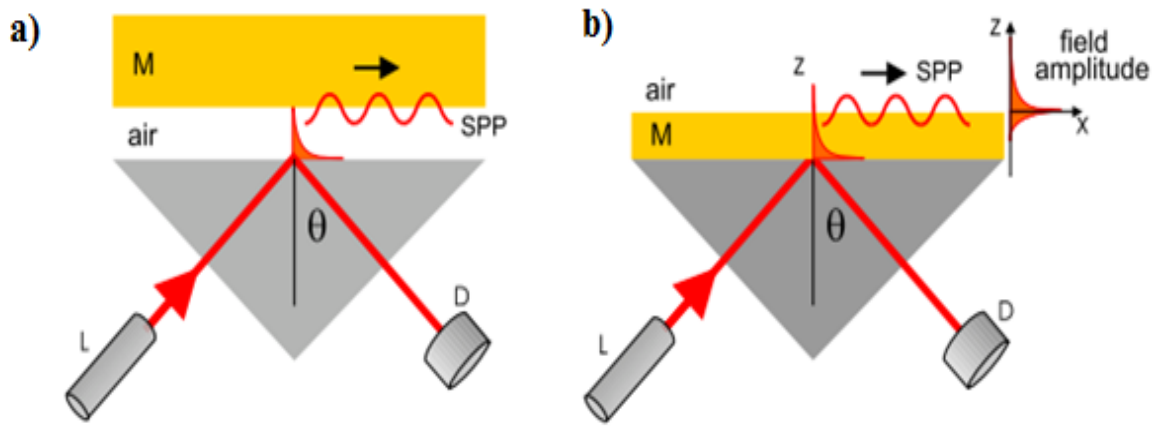

Figure 2.5 Otto and Kretschmann configurations for the optical excitation of surface plasmons polaritons by attenuated total reflection method. a) Otto configuration. b) Kretschmann configuration [14].

In the Otto configuration, a light beam is reflected off the base of the prism; adjacent to the base is a gap of low refractive index material. On the other side of the gap there is a silver film of optically infinite thickness. Total internal reflection (TIR) takes place for angles equal to or larger than the critical angle. Since the distance between metal and TIR surface reduces the SPR efficiency, this configuration is less useful.

The Kretschmann configuration has been become the most widely used geometry mainly because it has a practical application and commercial use of SPR. In the Kretschmann configuration, SPPs are excited on top of a silver film deposited on a glass substrate by light being totally reflected on the backside of the silver film, and the reflected intensity is measured.

2.2.1 Surface plasmon resonance sensors based on angular interrogation

SPR sensors based on angular interrogation, a beam of monochromatic light is used to excite SPPs (Figure 2.6). The coupling strength between the incident light wave vector and the SPP changes are determined by measuring the intensity of reflected light at multiple angles of incidence of the light wave.

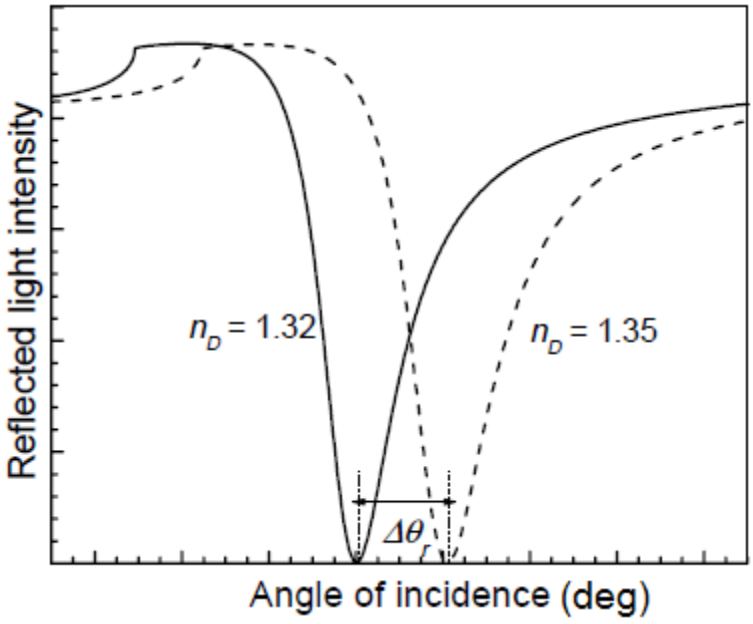

Figure 2.6 Intensity of reflected light as a function of angle of incidence for two refractive indices [15].

2.2.2 Surface plasmon resonance sensors based on wavelength interrogation

The wavelength modulation technique utilizes a beam of polychromatic light incident on the metal film under a fixed angle of incidence (Figure 2.7). By measuring the intensity of reflected light at multiple wavelengths and determining the wavelength at which a strongest coupling occurs, the wave vector of SPP and its changes can be determinate.

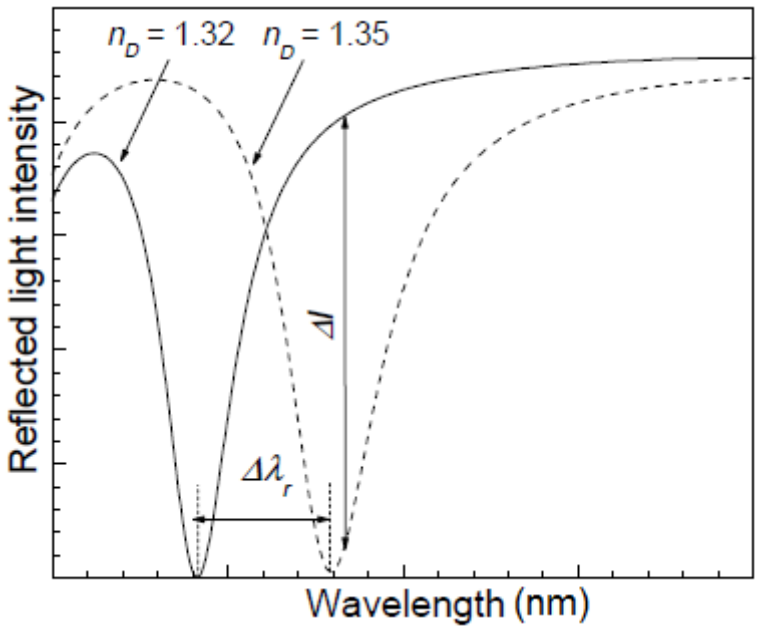

Figure 2.7 Intensity of reflected light as a function of wavelength for two refractive indices [15].

2.2.3 Surface plasmon resonance sensors based on intensity interrogation

The intensity modulation technique utilizes a beam of monochromatic light incident on the metal film where both the angle of incidence and its wavelength are kept constant. This technique measures the change in intensity of the light.

2.2.4 Surface plasmon resonance sensors based on phase interrogation

The angle of incidence of the light onto the metal film and its wavelength are fixed. The phase characteristics of light reflected for different polarizations are measured.

2.3 Extraordinary optical transmission

The transmission through subwavelength apertures has been characterized theoretically and experimentally in the last decades. In 1944, Bethe studied the optical transmission enhancement of an aperture in an infinitely thin perfect electric conductor [16] (Figure 2.8). The results from Bethe indicated that when the wavelength

λ of the transmitted light is larger than the circular hole of radius r, the transmission decays as

$$T \propto \left(\frac{r}{\lambda}\right)^4 \tag{2.4}$$

The idea that the amount of transmitted light decreases with the hole radius according to Bethe's law and this remained unchallenged until Ebbesen and co-workers discovered and demonstrated extraordinary optical transmission (EOT) through periodic nanohole arrays in silver and gold films where the amount of transmitted light at certain wavelengths was much larger than the predicted by Bethe's theory [17] (Figure 2.9).

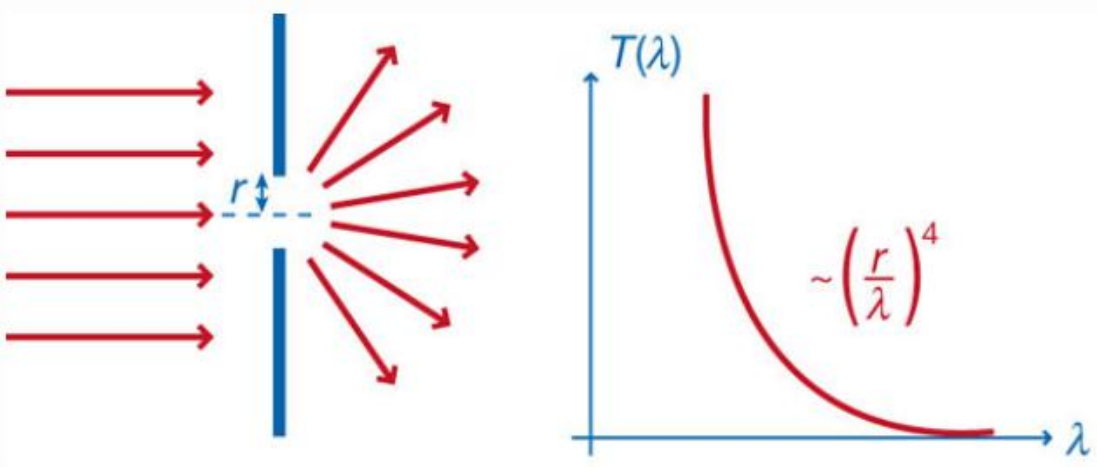

Figure 2.8 Diffraction of light and transmission spectrum through a subwavelength circular hole [18].

The transmission spectra are determinate by the role of periodicity, film thickness, and aspect ratio of the subwavelength apertures [19]. Figure 2.9 shows the zero-order (normal incidence) transmission spectra of a circular nanohole array in Ag film.

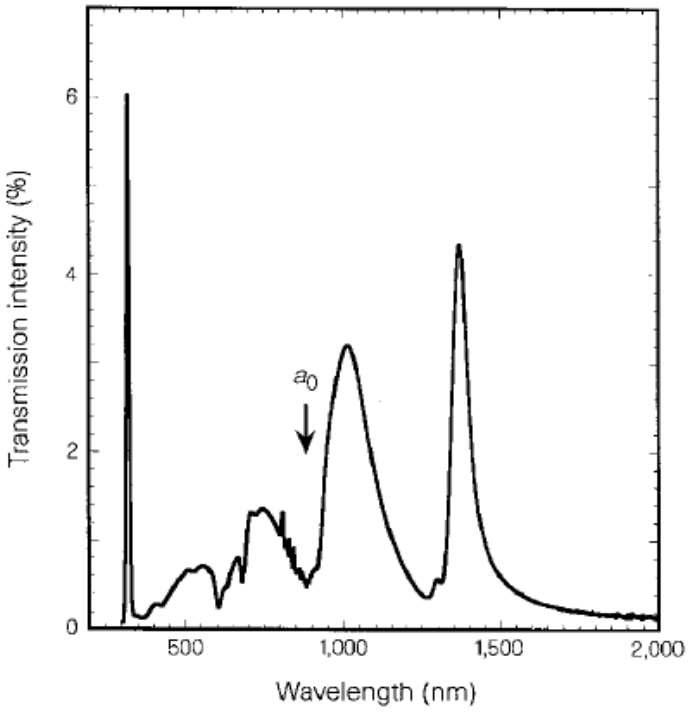

Figure 2.9 Zero-order transmission spectra for a square array of 150 nm holes in a Ag film [17].

Ghaemi *et.al* .[20] showed that metal films perforated with periodic nanohole arrays show exceptional zero order transmission spectra that are characterized by well-defined maxima and minima of which the positions are determined by the geometry of the nanohole array. The minima are due to Wood's anomaly, which is observed in diffraction gratings when a diffracted order becomes tangent to the plane of the grating. The maxima are the result of a resonant excitation of SPs due to the use of diffraction gratings from a periodic structure. The incident light will couple with SPs when satisfying the Bragg resonance condition given by:

$$\vec{k}_{SP} = \vec{k}_x \pm i\vec{G}_x \pm j\vec{G}_y \tag{2.5}$$

where $\vec{k}_x = (2\pi/\lambda)\sin\theta$ is the component of the incident photon's wave vector in the plane of the grating, i, j are Bragg resonant orders, $\vec{G}_x$ and $\vec{G}_y$ are the reciprocal lattice vectors for a square lattice with $\left|\vec{G}_x\right| = \left|\vec{G}_y\right| = 2\pi/a_o$ where a_o is the periodicity. At normal incidence $\theta = 0$, Equation 2.2 and Equation 2.5 reduce to

$$\lambda^{SP}(i,j) = a_o\left(i^2 + j^2\right)^{-\frac{1}{2}}\left(\frac{\varepsilon_d\varepsilon_m}{\varepsilon_d + \varepsilon_m}\right)^{\frac{1}{2}} \tag{2.6}$$

Equation 2.6 is for SPs on a smooth metal and dielectric interface.

EOT was also observed for single holes, and contributions from LSPs play a key role in these cases [21]. Figure 2.10 shows a single circular aperture in a 100 nm gold film and the CCD image of the aperture's light intensity.

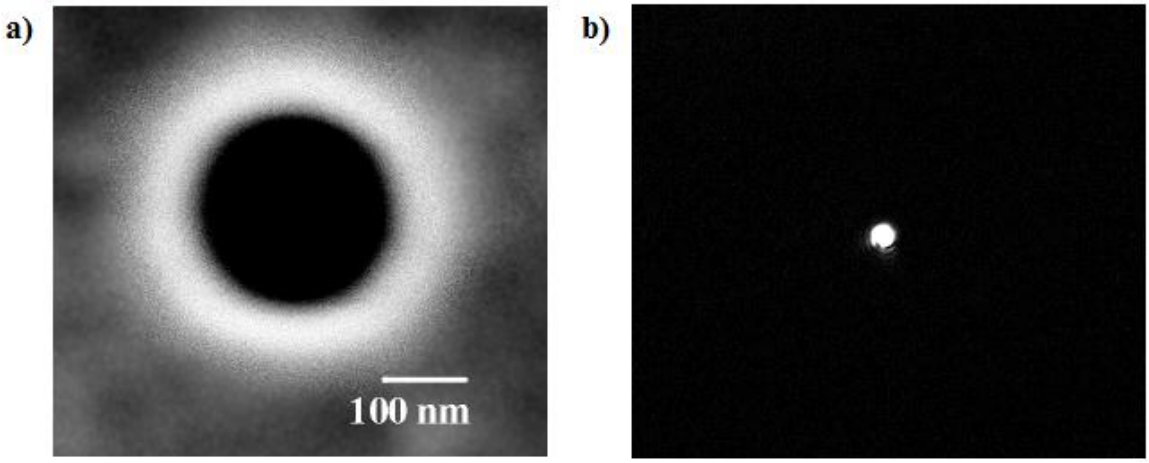

Figure 2.10 Single nanohole aperture. a) Scanning electron microscopy image of a circular aperture in a 100 nm gold film. b) CCD image of the light intensity of the circular aperture.

2.4 Surface plasmon as a sensor element

Since the discovery of EOT transmission through nanohole arrays in metal films [17] and its relation, SPR sensing has become an important area of research. Enhanced sensitivity sensors are desired for many applications including food safety

[22], medical diagnosis [23, 24], environmental applications [25], and drug development [26].

There have been two major approaches to optical excitation of SPs sensors: ATR in prism coupler based structures and diffraction gratings systems. Nylander and Liedberg *et. al.*[27] used the ATR method for sensing. The main advantage of this method is the relative simplicity and has been widely applied for biochemical sensing. This approach has been developed into commercial sensor systems. Cullen *et.al.*[28] used diffraction grating based systems for SPR sensing. In general, it has been suggested that diffraction grating based systems exhibit lower sensitivities than prism coupler [29].

In 1990, Pharmacia Biosensor AB launched the first commercial SPR product, the Biacore instrument. Biacore by far is the most widely used SPR sensor with a resolution of 10^{-7} refractive index units (RIU) [30]. Biacore uses a convergent light cone that illuminates the detection spot on a gold film via prism coupling in TIR mode and measures the changes in the SPR excitation angle due to change in the refractive index near to the metal and dielectric interface [31].

Traditionally SP sensors can be used in reflection or transmission mode geometry. Transmission mode geometry works at normal incidence and helps to simplify the alignment and miniaturization of the device for the integration in lab-on-chip environment. Reflection mode geometry introduces distortion to the imaging.

2.4.1 Nanohole arrays as surface plasmon sensors

Periodic nanohole arrays as SP sensors are extremely promising for future technologies because it allows a small footprint for dense integration, a high degree of multiplexing, a collinear optical detection for facile integration, and combined optofluidic functionality [32-51] (Figure 2.11).

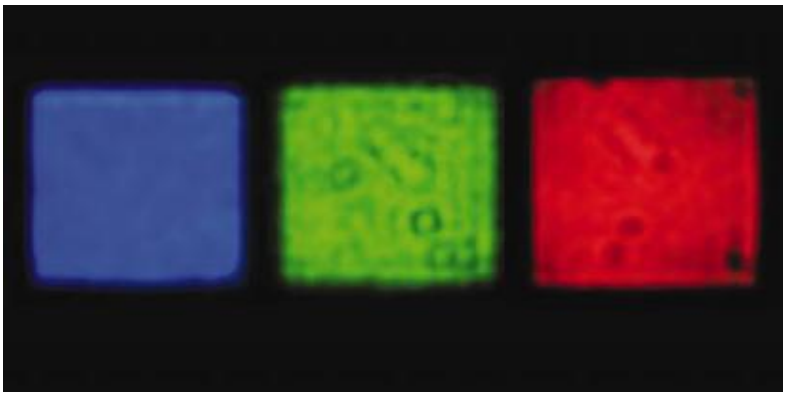

Figure 2.11 Normal incidence transmission of periodic nanohole arrays with hole diameters of 155 nm, 180 nm and 255 nm and periodicities of 300 nm, 450 nm and 550 nm [9].

Brolo *et.al.*[52] used nanohole arrays in a gold film to detect the molecular adsorption at both monolayer and multilayer levels. Circular nanohole arrays with a diameter of 200 nm and periodicities from 510 nm to 618 nm were used to measure the spectra of these nanohole arrays before and after molecular binding events using a white light source and a spectrometer (Figure 2.12).

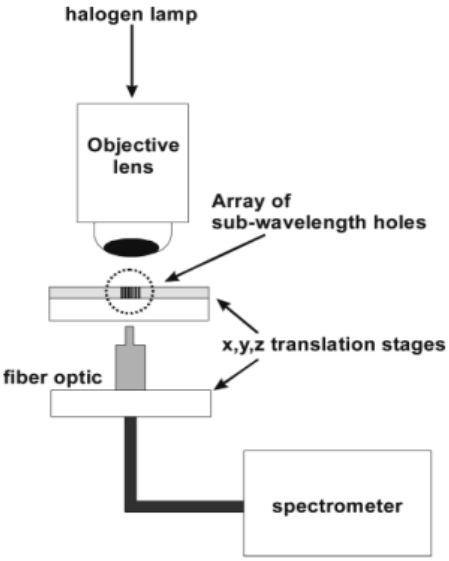

Figure 2.12 Experimental setup for light transmission measurements of circular nanohole arrays of diameter 200 nm and periodicities from 510 nm to 618 nm in a gold film [52].

Figure 2.13 shows the transmission spectra through a bare or clean nanohole arrays in a gold surface. When the gold surface was modified by immersing the nanohole arrays in an ethanoic solution of mercaptoundecanoic acid (MUA) there was a red shift in the wavelength of maximum transmission due to the changes in the dielectric properties of the surface. There was an additional wavelength shift when the nanohole arrays were immersed by bovine serum albumin (BSA). The sensitivity recorded in this experiment was 400 nm/RIU.

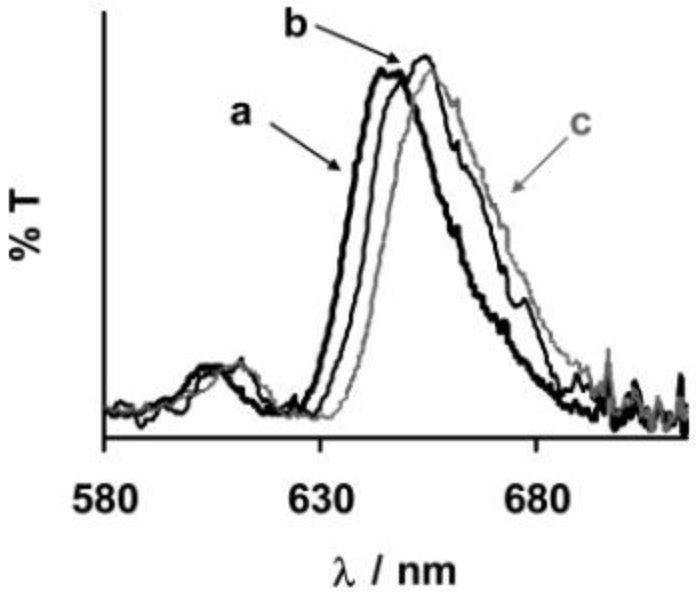

Figure 2.13 Normalized transmission spectra of normally incident light through a circular nanohole array of diameter 200 nm in a 100 nm gold film. a) Bare or clean Au surface. b) Au modified with a monolayer of MUA. c) Au-MUA modified with BSA [52].

Lesuffleur *et.al*.[53] demonstrated that the presence of sharp apexes in a double nanohole structure improves the local field intensity, transmission efficiency, and polarization selectivity compared to circular nanohole arrays. The double nanohole structures consisted of two overlapping circular holes with a 200 nm diameter and a center to center hole distance of 190 nm in a 100 nm thick gold film with a 5 nm Cr adhesion layer in a glass substrate. Figure 2.14 shows the transmission spectrum that was

collected from this double nanohole structures using a fiber-optic spectrometer. The sensitivity recorded in this experiment was 600 nm/RIU.

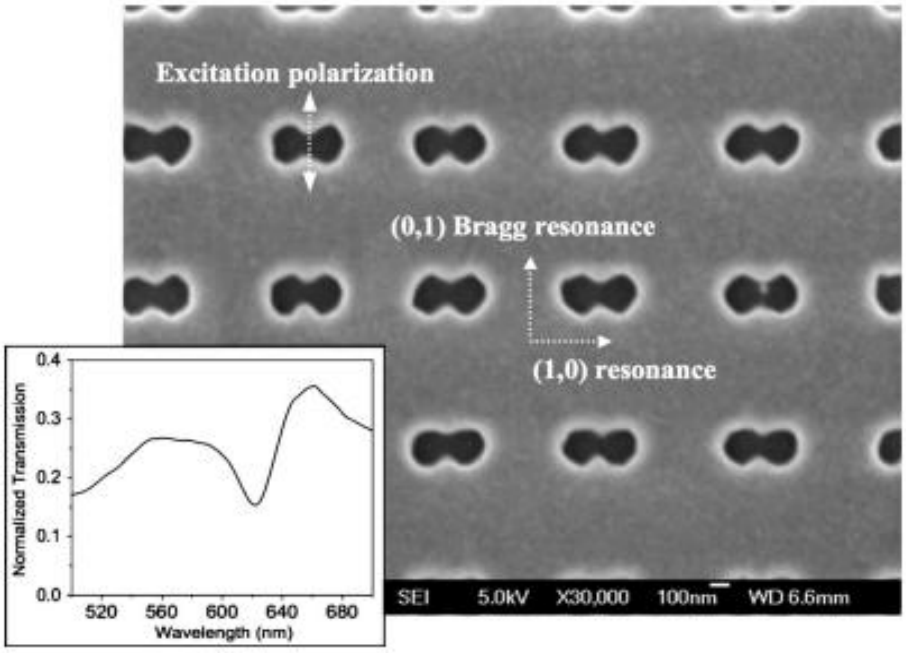

Figure 2.14 Scanning electron microscopy picture of the double hole array with a diameter of 200 nm and the center to center hole distance of 190 nm. (Inset) Transmission spectra of the double hole array [53].

Pang *et.al*.[54] studied theoretically and experimentally the spectral sensitivity of nanohole arrays and measured protein-protein bonding between BSA and monoclonal anti-BSA. Figure 2.15 shows the SPR wavelength versus time while different refractive indices were flowing on circular nanohole arrays with a diameter of 300 nm.

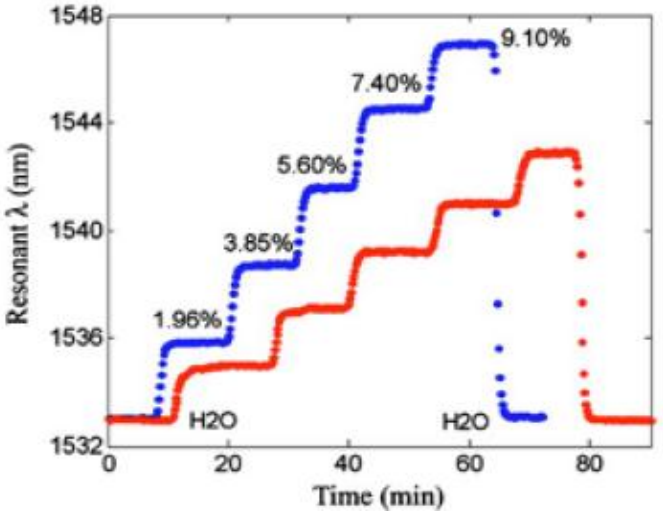

Figure 2.15 Sensitivity measurements of circular nanohole arrays with a diameter of 300 nm. SPP resonant wavelength evolves with time while ethylene glycol water solutions with different concentrations and deionized water flow through the nanohole arrays. The blue and red colors correspond to the (1,0) and (-1,-1) SPP modes. [54].

Tetz *et al.* [55] demonstrated an improvement in resolution using circular nanohole arrays with a diameter of 200 nm and a periodicity of 1400 nm in a 200 nm gold film (Figure 2.16). The result was a resolution close to 10^{-5} RIU comparable with Biacore.

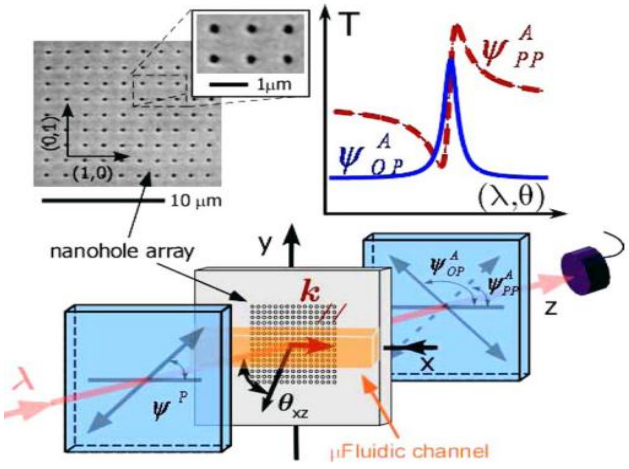

Figure 2.16 Experimental diagram of a nanohole array with a diameter of 200 nm and a periodicity of 1400 nm in a 200 nm gold film [55].

This improvement in resolution was obtained by using crossed polarizers to select between the coherent and incoherent contributions of EOT. The incoherent contribution is given by the interference between the direct transmissions through the nanohole arrays. The coherent contribution is given by SPs mediated transmission through the nanohole arrays. Figure 2.17 shows that after the beam passed through the sample, it was separated into two orthogonal linearly polarized beams, and their intensity was detected.

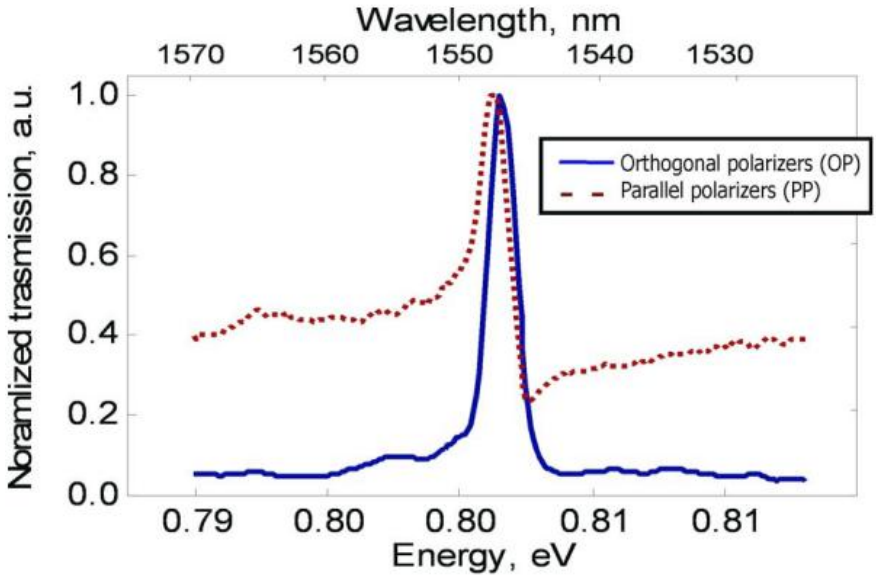

Figure 2.17 Surface plasmon resonance sensor with an improvement in resolution. Normalized transmission as a function of energy (Wavelength) [55].

2.4.2 Surface plasmon resonance sensors based on intensity interrogation

Despite the several advantages of nanohole arrays as SPs sensors, their sensitivity and resolution are lower compared to conventional SPR devices [55-58]. Although intensity interrogation has advantages like high speed and multi-channel applications, the low SNR limits its detection resolution which is one to two orders of magnitude compared to the ATR method. An intensity interrogation approach with one or several fixed wavelength sources has the advantage of providing a simple and more efficient system in a low cost environment.

Yang *et.al*.[59] performed multiplexed sensing on nanohole arrays using intensity interrogation with a monochromatic light, the change of transmission intensity is defined as the sensing signal. For this experiment the effect of absorption, scattering of particles and source fluctuations were taking in consideration to measure the change in index of refraction. Nanohole arrays were fabricated using a 100 nm gold film with a 75 nm Cr adhesion layer. Each nanohole array has a size of 5 μm × 5 μm. Transmission spectra and real time measurements were collected and the intensity value of the individual nanohole arrays from CCD images was extracted using a processing program (Figure 2.18). Contributions from molecular absorption, scattering and change in index of refraction were distinguished using different nanostructures like BSA, NaCl, and liposome solutions.

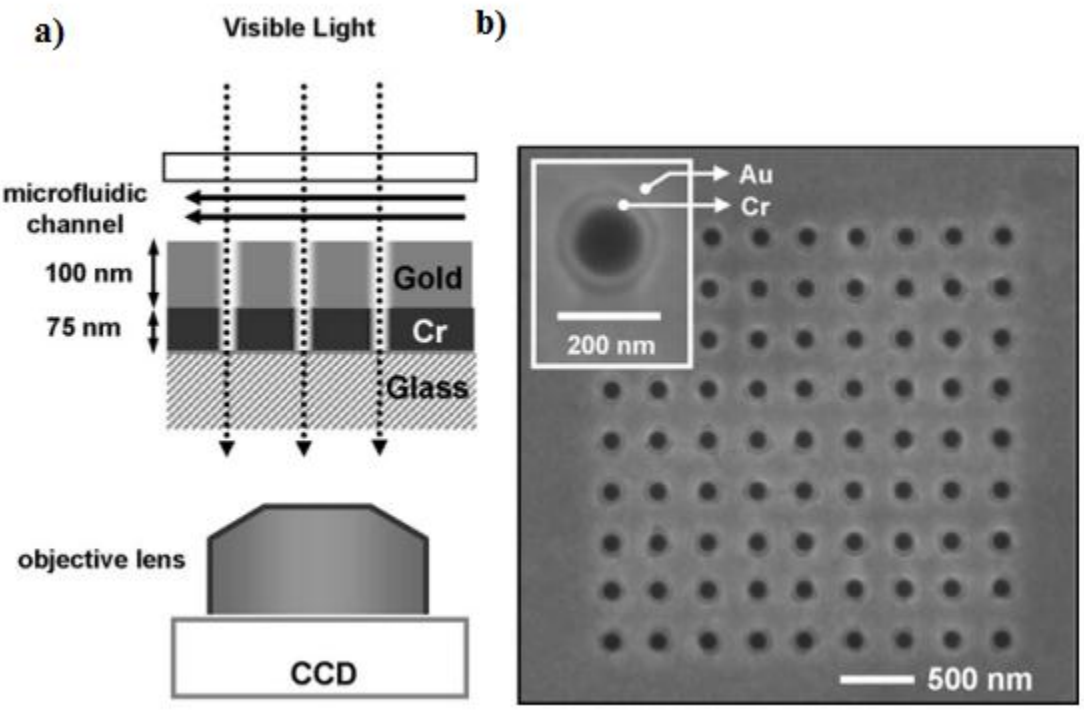

Figure 2.18 Surface plasmon resonance sensor based on intensity interrogation. a) Schematic of the optical setup of a nanohole array sensor. b) Scanning electron microscopy image of a 9 × 9 circular nanohole array with a diameter of 200 nm [59].

Figure 2.19 shows a CCD image of superwalength holes with a diameter of 1.6 μm and subwavelength hole arrays with diameters of 150, 160, 170 and 180 nm and the sensing

response upon introducing 4% NaCl of a superwavelength hole. A resolution close to 10^{-4} RIU was demonstrated.

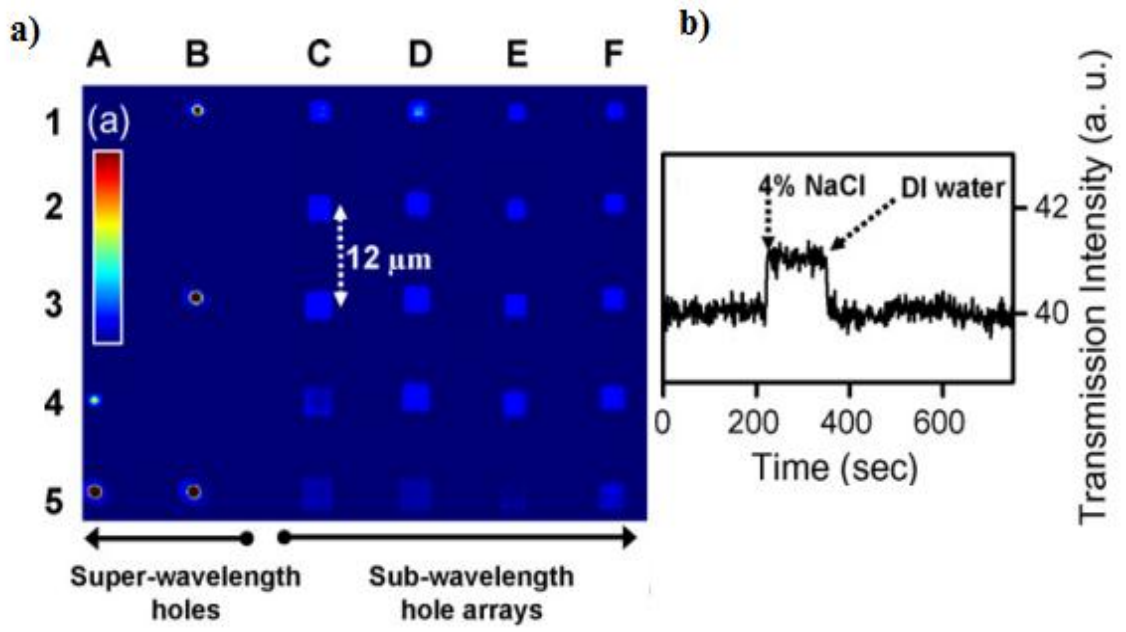

Figure 2.19 Surface plasmon resonance sensor of superwavelength holes and subwavelength hole arrays. a) CCD image of superwavelength holes with a diameter of 1.6 μm and nanohole arrays with diameters of 150 to 180 nm in steps of 10 nm. b) Sensing response of a superwavelength hole toward 4% NaCl solutions [59].

An important improvement in sensitivity and resolution was demonstrated by Stark *et.al.* [43] who used the changes in amplitude of transmission from a single wavelength source using a CCD camera. Circular nanohole arrays with a diameter of 150 nm and a periodicity of 350 nm in a 100 nm gold film and a 4 nm Cr adhesion layer was used for this experiment (Figure 2.20).

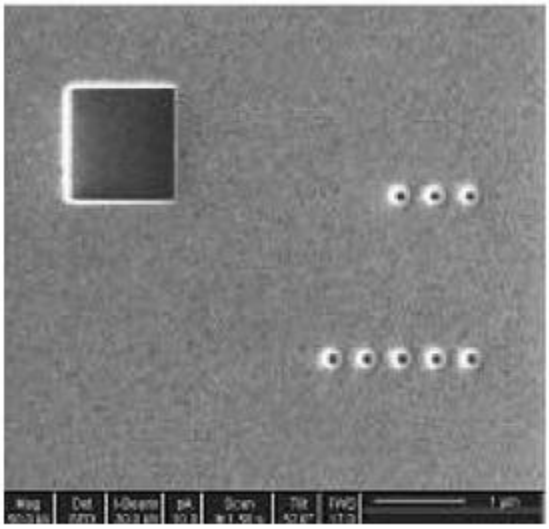

Figure 2.20 Scanning electron microscopy image of circular nanohole arrays with a diameter of 150 nm and a periodicity of 350 nm next to a superwavelength (1.5 µm × 1.5 µm) aperture [43].

Figure 2.21 shows a change in transmission ratio of about 0.8% with a change in index of refraction (From pure water to NaCl). A resolution of 9×10^{-6} RIU and a sensitivity of 88,000%/RIU was demonstrated.

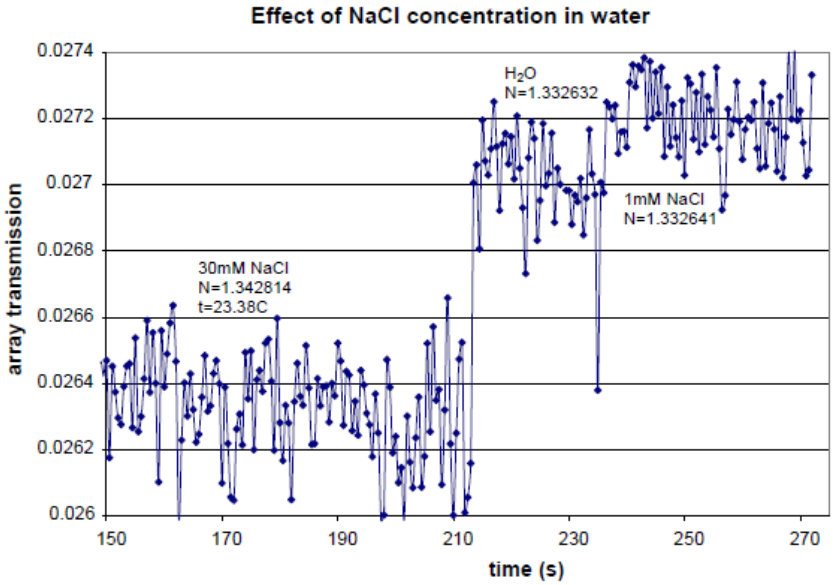

Figure 2.21 Response of the nanohole sensor to a change in index of refraction due to a change in NaCl concentration and water [43].

Lesuffleur *et.al*.[34] used SPR imaging with nanohole arrays illuminated by a HeNe laser source in order to achieve a higher resolution. A laser source was used to provide a higher intensity and stability that helped to improved detection sensitivity. Circular nanohole arrays were fabricated with a diameter of 200 nm in a 100 nm gold film with a 5 nm Cr adhesion layer and periodicities ranging from 380 nm to 460 nm. Figure 2.22 shows the transmission spectra of one of the circular nanohole array that was measured with a tungsten-halogen light source.

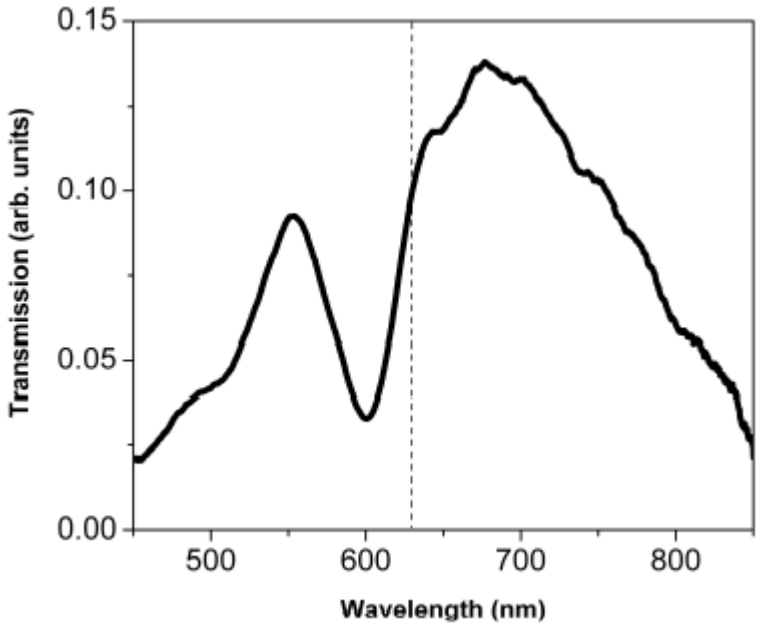

Figure 2.22 Transmission spectra of a circular nanohole array with a diameter of 200 nm and a periodicity of 380 nm. The dashed line represents the wavelength of the HeNe laser at 633 nm [34].

A self-assembled monolayer (SAM) of alkanethiolates was used as model system to characterize molecular binding kinetics on the gold surface on this nanohole sensor. The spectral shift $\Delta\lambda$ due to molecular binding is then given by

$$\Delta\lambda = S(\Delta n) \tag{2.5}$$

where S represents the spectral sensitivity that depends on the geometrical parameters of the nanohole arrays and of the dielectric functions of the media. For multiplex SPR

imaging, it can be more useful to measure the change of the transmitted intensity I_T at a fixed detection wavelength that is given by

$$\Delta I_T = -\left(\frac{dI_T}{d\lambda}\right)\cdot S(\Delta n) \tag{2.6}$$

For SPR imaging using a laser source, the sensitivity depends on the slope $dI_T / d\lambda$ that is related with the sharpness of the resonance peak and the spectral sensitivity. Figure 2.23 shows the normalized kinetics data from four individual nanohole arrays with periodicities of 380, 405, 430 and 460 nm. The estimated sensitivity of the nanohole arrays that was obtained in the experiment based on SPR imaging with a laser was 16,600%/RIU.

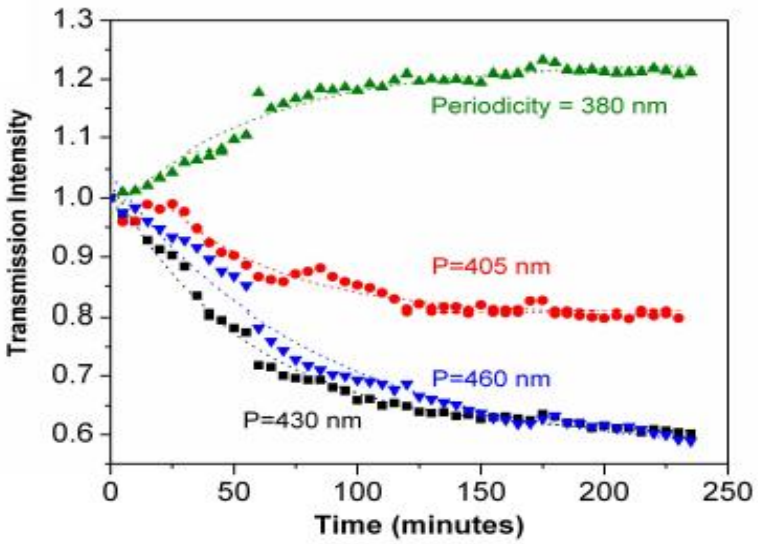

Figure 2.23 Normalized kinetics data from nanohole arrays with different periodicities. The laser transmission can either increase or decrease depending of the array periodicity. This is expected since the higher local refractive index of the bound SAM will red shift the transmission spectrum, and the measured intensity can increase or decrease depending on $dI_T / d\lambda$ whether is negative or positive [34].

Lindquist *et.al.*[60] demonstrated that to increase the scalability of a system several issues need to be addressed like if the size of the nanohole is reduced the detection

sensitivity suffers and if several nanohole arrays are brought close to each other the SPs interference introduces large sources of error. The use of plasmonic Bragg mirrors surrounding the nanohole arrays can improve the resolution and improve the scalability issues of a system. The surrounding Bragg mirrors reflect the outgoing SPs waves back into the nanohole array so the amount of transmission increases. For this experiment, samples were fabricated in a 200 nm gold film with a 5 nm Cr adhesion layer. Circular nanohole arrays with a diameter of 150 nm and periodicities from 370 to 450 nm were surrounded with four Bragg mirror grooves that were milled on a 100 nm wide and 50 nm deep. The surrounding Bragg mirrors sharpen the transmission resonance (Figure 2.24).

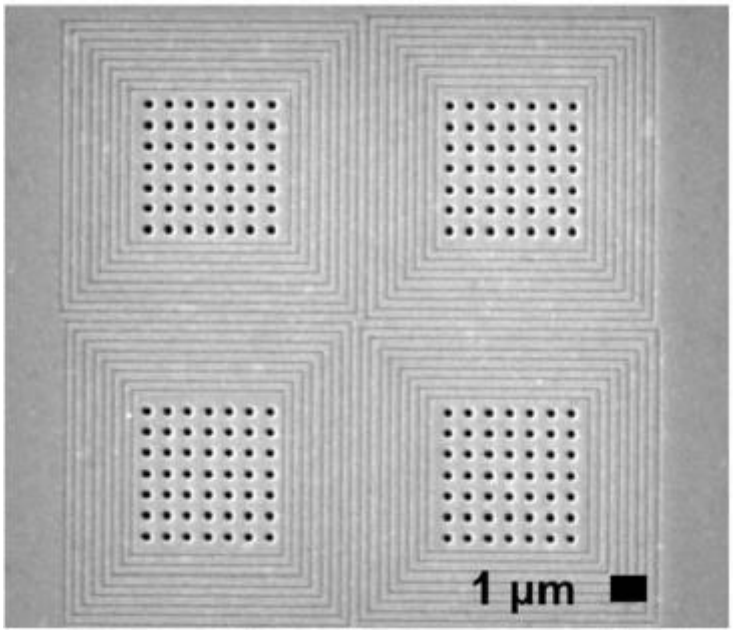

Figure 2.24 Scanning electron microscope image of nanohole arrays surrounding by Bragg mirror grooves in a 200 nm gold film [61].

The used of Bragg mirrors enhanced and sharpened the transmission resonance even if the number of nanohole was reduced without sacrificing the sensitivity. For a 7-by-7 array without surrounding Bragg mirror grooves, the largest transmitted intensity change was 30%, whereas with the addition of the Bragg mirror grooves, the largest transmitted intensity change was 55%.

Blanchard-Dionne *et.al.*[57] improved the resolution of a nanohole array sensor by using the transmission signal of two orthogonal polarization impinging on nanohole array with rectangular periodicities. This method allowed up to double the sensitivity of the sensor since it used the variation of two slopes instead of only one. Circular nanohole arrays with periodicities of 380 nm × 420 nm in a 100 nm gold film with a diameter of 200 nm were fabricated for this experiment. A change in the index of refraction close to the metal surface gave an increased in transmission for one polarization and a decreased for the other one, and the difference between the two corresponds to the detection signal (Figure 2.25).

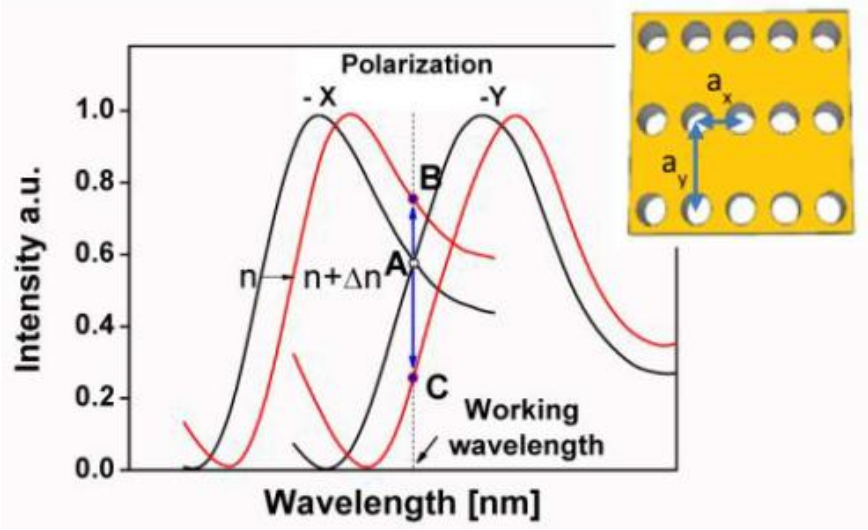

Figure 2.25 Circular nanohole arrays with two periodicities a_x and a_y. The transmission spectrum shows resonant peaks at different wavelength for two orthogonal polarizations [57].

A HeNe laser was used along with a polarizer and a quarter wave plate in order to change the state of polarization of light. An intensity sensitivity of 1700%/RIU for the first polarization was obtained and 1200%/RIU for the second polarization was obtained for a total of 2900%/RIU that was obtained by using the balanced detection. The sensitivity of this experiment was higher compared to nanohole arrays with square periodicities. Figure 2.26 shows that the SNR obtained from the single polarization is 5 times lower than the one obtained from the balanced detection of rectangular periodicities. The maximum

sensitivity obtained in this experiment was 6.4×10^{-6} RIU using balanced detection and 1.7×10^{-4} RIU for a single polarization.

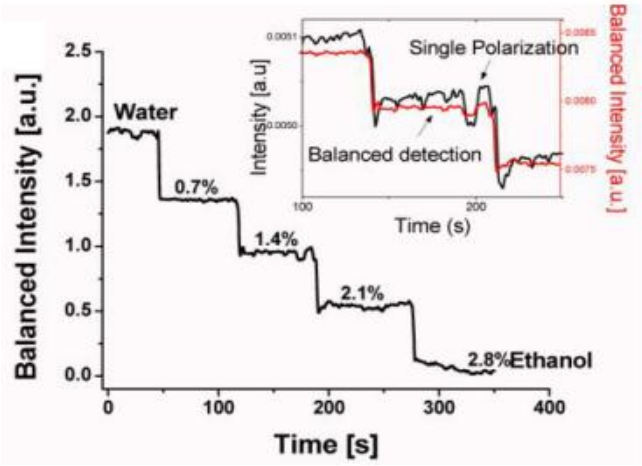

Figure 2.26 Intensity difference between two polarizations as a function of time while different concentrations of ethanol and water were used to measure the resolution of the system. (Inset) Difference intensity using a single polarization while different concentrations were used on a nanohole array [57].

2.5 Summary

This chapter started with a brief discussion on concepts like SPP and LSP. EOT has been described as the consequence of SPs in the previous sections. Then number of factors like hole shape, periodicity, and gold thickness has an influence in nanohole arrays were discussed. The last section of the chapter showed the application of nanohole array as a sensing element. The benefit of transmission mode geometry over the reflection mode geometry has been discussed in context of lab-on-chip application. Despite the several advantages of nanohole arrays as SPs sensors, their sensitivity and resolution are lower compared to conventional SPR devices. So far, the resolution of nanohole arrays has been demonstrated to be between 10^{-3}-10^{-6} RIU in complicated setups [55-58]. In this work, we optimize the resolution of nanohole arrays in metal films for refractive index sensing by increasing the sensitivity with modifications to the hole-array parameters and by reducing the noise of the sensor system, while maintaining simple setup geometry.

Chapter 3: Fabrication and simulation methods of nanohole arrays

3.1 Introduction

This chapter deals with the fabrication and simulation methods for nanohole arrays. The nanofabrication techniques for nanohole arrays can be mainly categorized into two groups: bottom up and top down methods. Focused ion beam (FIB) is a top down nanofabrication technique that is inherently destructive to the sample but allow a high degree of control in the fabrication of subwavelength apertures. Scanning electron microscope (SEM) has been employed for the imaging of nanohole arrays.

For the design of the nanohole arrays parameters like subwavelength aperture size, periodicity, and gold thickness can be varied by using finite difference time domain (FDTD) simulations. For the integration of microfluidics and nanohole arrays for the development of microchips rapid prototyping lithography was used. The background and details of these methods are explained in this chapter.

3.2 Scanning electron microscope

Scanning electron microscope (SEM) is an instrument that scans the surface of a sample with a finely converged electron beam in a vacuum and detects the information produced and presents an enlarged image of the surface of the sample on a monitor screen. The SEM uses secondary electrons, backscattered electrons, characteristic X-rays and other signals are used to form an image (Figure 3.1). Secondary electrons are produced near to the surface of the sample with lower energy and the secondary electrons obtained upon detecting these electrons reflect the fine topographical structure of the sample. Backscattered electrons are those reflected upon striking the atoms composing the sample and the number of these electrons is dependent on the composition of the sample. An X-ray detector can also be mounted to the SEM for conducting elemental analysis.

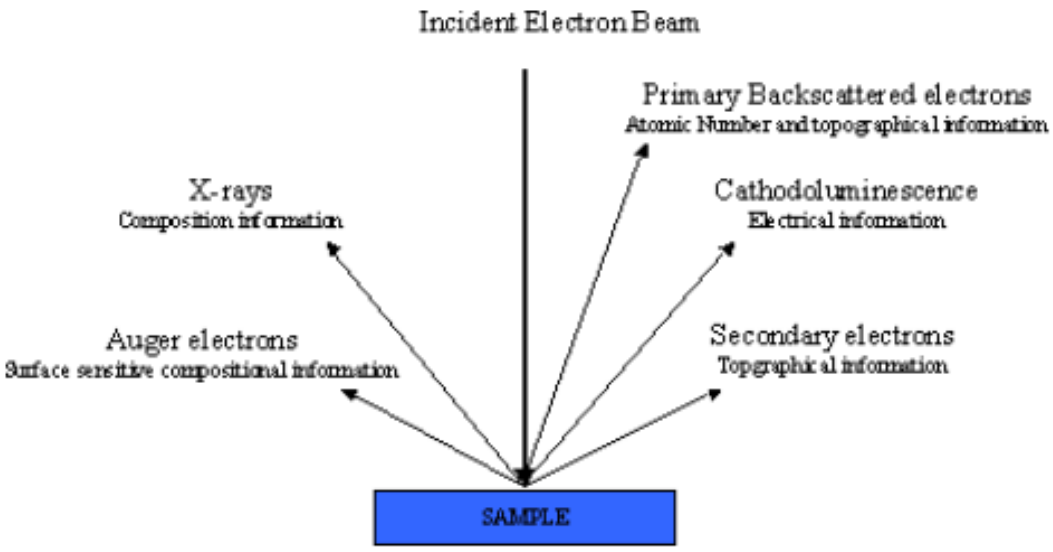

Figure 3.1 Signals produced from a sample when a sample is irradiated with an electron beam in a vacuum [62].

3.2.1 Structure of the scanning electron microscope

The SEM consists of a column, a specimen chamber, a display, and an operating section. The interior of the column is kept in a high vacuum. Here we have an electron gun fitted with tungsten filament cathode that emits electrons and accelerates them in a strong electric field. This electron beam is converged into a fine beam via the electromagnetic lenses (condenser and objective lenses). The electron beam has an energy ranging from .5 keV to 40 keV and the electromagnetic lenses produce an electron beam having a spot of .4 nm to 5 nm in diameter. The deflection coils are used to scan the electron beam in X and Y directions and change the area or magnification to be scanned. When the primary electron beam interacts with the sample, the electrons lose energy by repeated random scattering absorption. Finally, we have a vacuum pump that evacuates the column and specimen chamber to a high vacuum level (Figure 3.2).

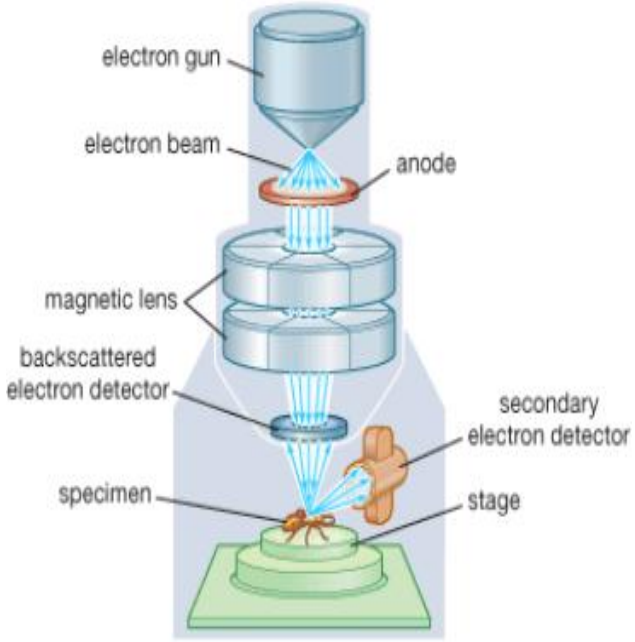

Figure 3.2 Schematics of a scanning electron microscope [63].

3.2.2 Configuration and operation principle for energy dispersive X-ray

One important feature of the SEM is that it has an X-ray analyzer for determining what elements are included in the sample. The energy dispersive X-ray is configured by a combination of solid state detector that is used as a Si(Li) detector in which Li +ions are diffused in a p-type single crystal Si to neutralize the acceptor and thereby forming an i layer (intrinsic layer) without an electric charge. When an X-ray is incident on the i layer, electron hole pairs are produced in proportion to the X-ray energy and they are moved to the respective electrodes by the reversed bias field, so a signal current flows. The energy of obtaining a pair of electron and holes in a Si(Li) detection device is about 3.9 eV. Now, we have electron hole pairs that are produced by dividing the incident X-ray energy with 3.9 eV. Since the i layer is formed in a thickness of several millimeters, characteristic X-rays having a wide energy range from a few hundred eV to few ten keV can be detected. The signal current is amplified with the preamplifier; its pulse waveform is shaped with the proportional amplifier and sent to the multi-channel pulse height analyzer (Figure 3.3).

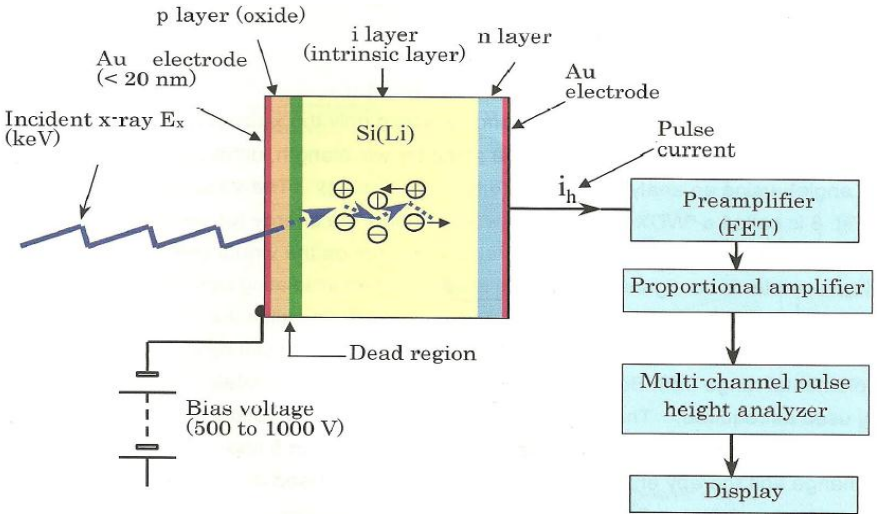

Figure 3.3 Operating principle of the Si(Li) detector for energy dispersive X-rays [64].

Figure 3.4 shows an image of a rectangular nanohole array in a 100 nm gold film and the results from energy dispersive X-ray spectroscopy where it shows that gold was removed.

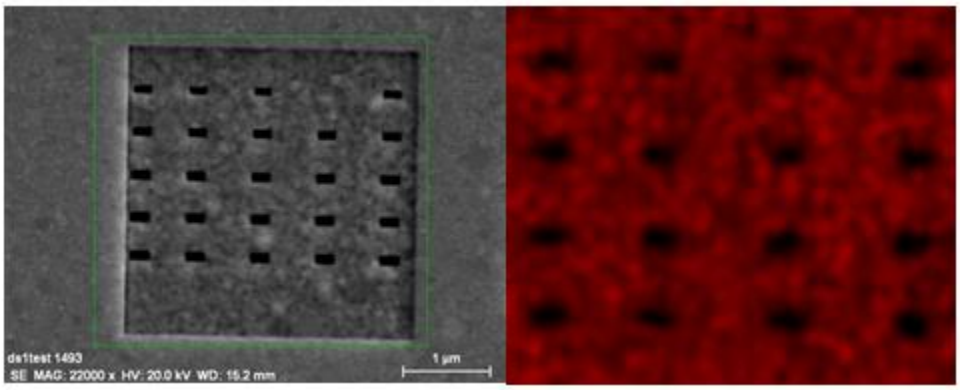

Figure 3.4 Energy dispersive X-ray image of a rectangular nanohole array in a 100 nm gold film.

3.2.3 Imaging problems in scanning electron microscope

Three main problems can affect the imaging process. The first one is the charge-up phenomenon (Figure 3.5). This occurs during observation of non-conductive samples, and this happened when scan speed or magnification is changed. In order to solve this

problem is necessary to reduce the accelerating voltage, the irradiating current or observe images in low vacuum mode.

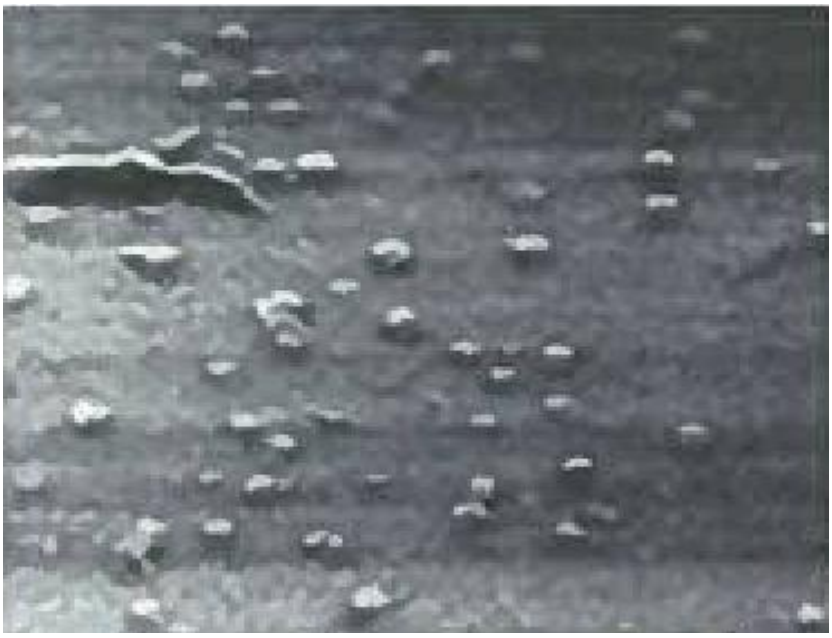

Figure 3.5 Line by line charging, electrons release from the sample randomly line by line causing bright streaks across the sample [64].

The second one is the contamination of the sample that occurs when gas molecules of hydrocarbons existing around the sample due the electron beam irradiation, then bond together and adhere to the sample surface. Figure 3.6 shows the darkness is thought to be the matter accumulated on the sample surface suppresses the discharge of secondary electrons from the sample. To solve this problem it is necessary to use the minimum amount of conductive paste when mounting the sample in the instrument and dry the conductive paste before inserting the sample into the instrument for observation and carry out focusing as quickly as possible and avoid observing the same location for a long time especially at high magnification.

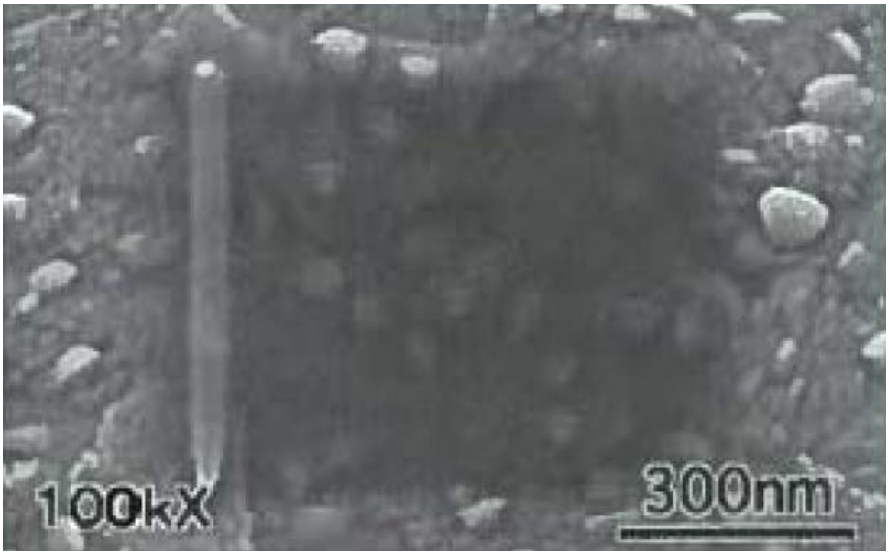

Figure 3.6 Scanning electron microscopy image of a contaminated layer of a gold sample [64].

The third one is the thermal change or chemical change occurring on a sample due to electron beam irradiation referred to as beam damage (Figure 3.7). The main steps to avoid this problem is to reduce the sample irradiating current, lower the accelerating voltage, and apply metal coating to the sample.

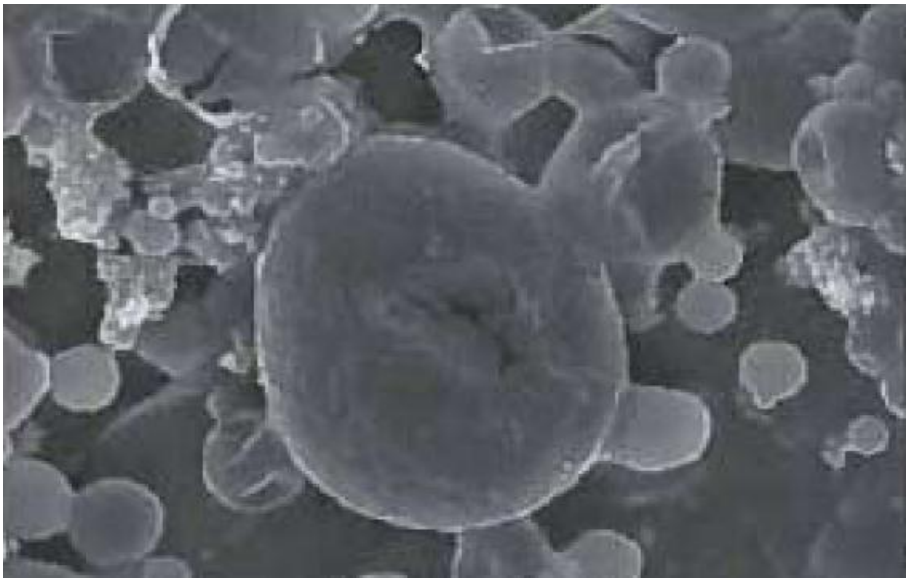

Figure 3.7 Scanning electron microscopy image of a biological damage sample caused by electron beam irradiation [64].

Another causes of image abnormalities are a movement in the sample, this happens because the sample is not fixed or is inserted incompletely onto specimen stage, and a poor focus that happens when we have an inadequate optical axis alignment or an objective aperture contaminated.

3.2.4 Imaging process using Hitachi S-4800

Sample preparation is the first step for imaging in SEM. For biological and polymer samples the preparation technique is more elaborate but for conductive metal samples is minimal. After the preparation it is necessary to put the sample inside the specimen chamber, set an acceleration voltage, current, and working distance according to the material and properties of the sample. Magnification can be controlled over a range up to six orders of magnitude from about 10 to 800,000 times.. Magnification is controlled by the current supplied to X and Y scanning coils or the voltage supplied to X and Y deflector plates. Working distance plays an important role, if it is not the right one the images are going to have good quality. Changing the working distance brings about changes in the focal length of objective lens and the divergence angle of electron beam. The main steps to obtain a quality image are: focusing, beam alignment, aperture alignment, X-alignment, Y-alignment, astigmatism. Figure 3.8 and Figure 3.9 show nanohole arrays images that were taken by using the SEM (Hitachi S-4800).

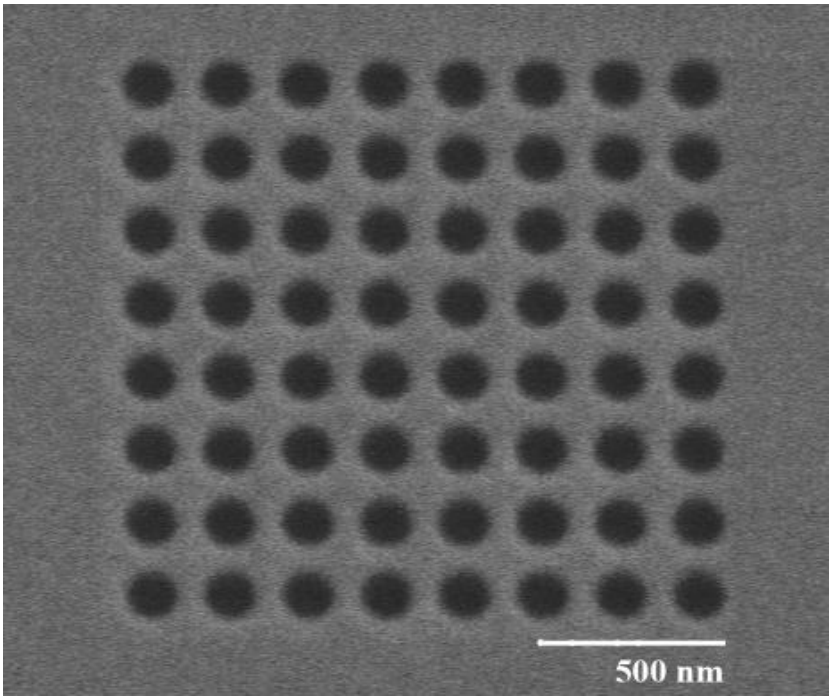

Figure 3.8 Scanning electron microscopy image of a circular nanohole array in a 300 nm thick gold film.

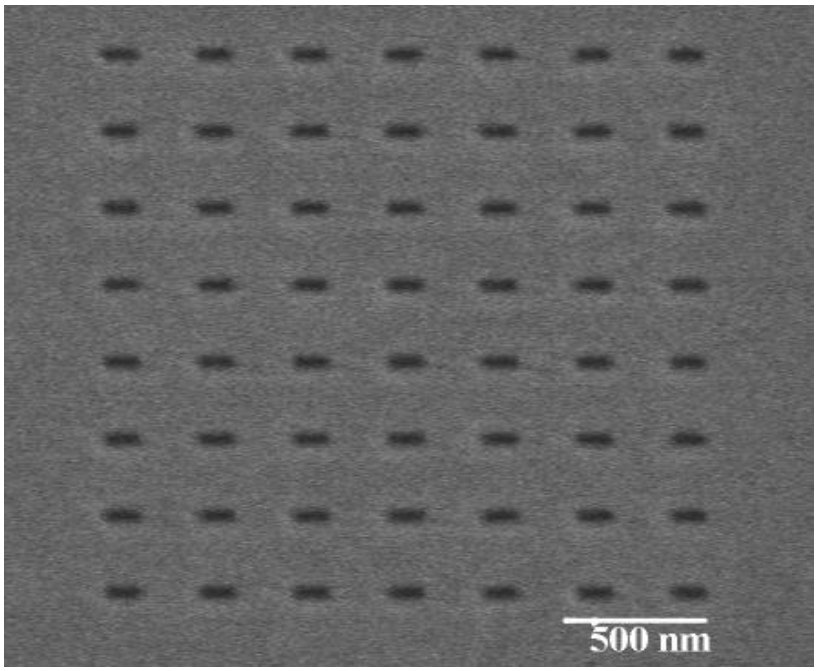

Figure 3.9 Scanning electron microscopy image of a rectangular nanohole array in a 300 nm thick gold film.

3.2.5 Summary

SEM is an essential research tool in the scientific and industry fields. The SEM has a large depth of field; the SEM offers the possibility to see a larger part of the object being studied. It is possible to obtain clear images and as SEM uses electromagnets rather than lenses, the researcher has control in the degree of magnification. Nanohole arrays are easy to image by using SEM mainly because samples require minimal preparation actions.

3.3 Focused ion beam

Focused ion beam (FIB) is a technique used in site specific analysis, milling, and deposition of materials. FIB scans the sample surfaces with finely focused beam of gallium ions, and by detecting generated secondary electrons, enabling the observation of microscope images and process sample surfaces (Figure 3.10). The main difference between SEM and FIB is that the first one uses a focused beam of electrons in order to image a sample in the chamber and the second one uses a focused beam of ions that can be operated at low beam currents for imaging or high currents for site milling. The applications demonstrated for FIB systems so far are implantation, milling, surface chemistry, lithography, microscopy, and material analysis.

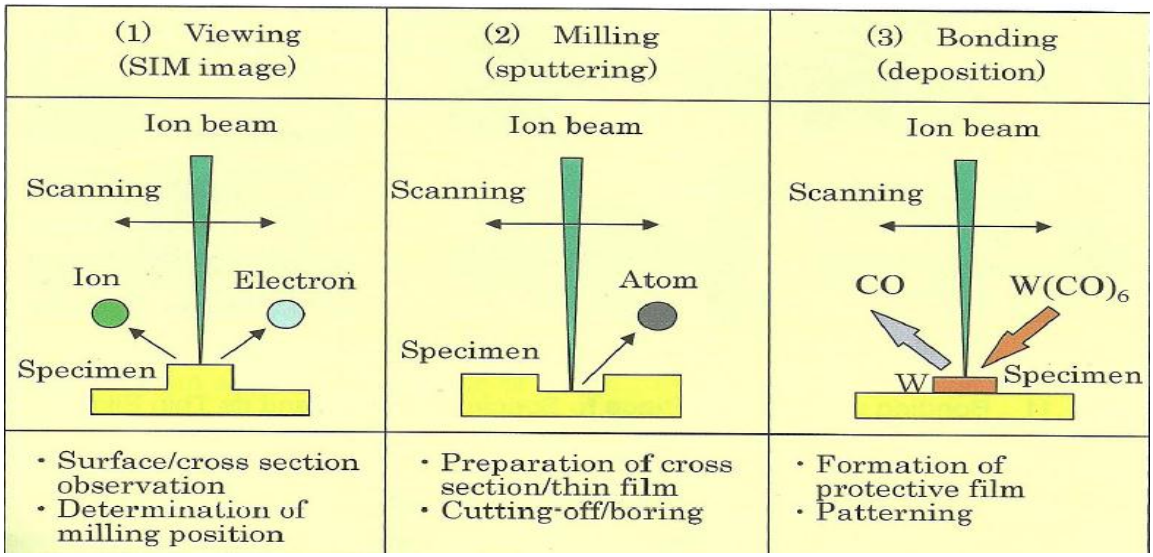

Figure 3.10 Three basic functions on focused ion beam milling: viewing, milling, and deposition [64].

3.3.1 Ions vs. electrons

Ions are positive and much larger than electrons and the penetration depth is much lower than the penetration of electrons even when they have the same energy. Ions can have a high momentum because they are heavier than electrons. Ions are able to remove atoms from the substrate and with a proper dwell time, beam position and size it is possible to remove material locally in an efficient controlled matter in nanometers scales.

3.3.2 Operation principle of focused ion beam

The principle of FIB is really simple; a gallium primary ion beam hits the surface of the sample and then sputters a small amount of material leaving the surface as either secondary ions or neutral atoms. The signal is collected from the secondary electrons that the primary beam produced in order to form an image. At low primary beam currents, FIB systems can easily achieve 5 nm imaging resolution and very little material is sputter. At higher primary currents it is possible to remove a lot of material but the precision milling decreases. FIB destructs part of the specimen that is why is used as a micro machining tool (Figure 3.11).

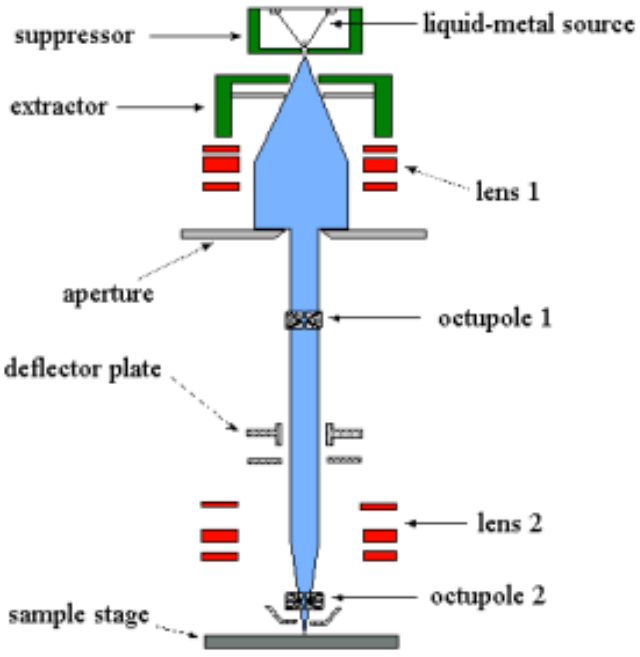

Figure 3.11 Operation principle of a focused ion beam system [65].

3.3.3 Fabrication of nanohole arrays using Hitachi FB-2100

Sample preparation is the first step for fabrication using focused ion beam. After the preparation it is necessary to put the sample inside the specimen chamber, set an acceleration voltage, current, and working distance according to the material and properties of the sample. It is necessary to select a beam for milling, the main steps for beam alignment are: set the magnification, focusing, X-alignment, Y-alignment, and turning on the Wobbler. In order to fabricate nanohole arrays, parameters such as dwell time, number of passes, and beam type must be selected. Imaging through FB-2100 is possible, however, once the sample is imaged there is not guarantee that it will not be destroyed (Figure 3.12).

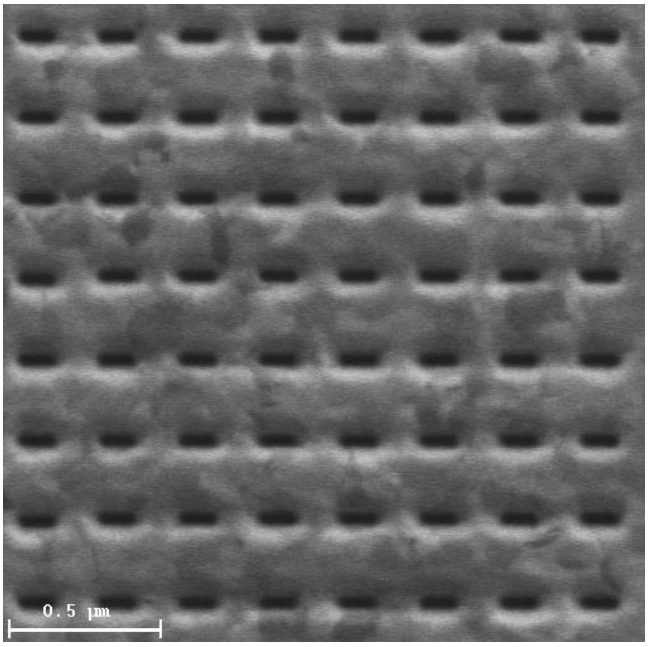

Figure 3.12 Image of a rectangular nanohole array in a 100 nm gold film using focused ion beam (Hitachi FB-2100).

Bitmaps can be used for the fabrication of nanohole arrays; FB-2100 takes bitmap inputs and cuts accordingly. For Hitachi FB-2100 bitmaps should be 2000 × 2000 pixels and be purely black and white with no grayscale tones (Figure 3.13).

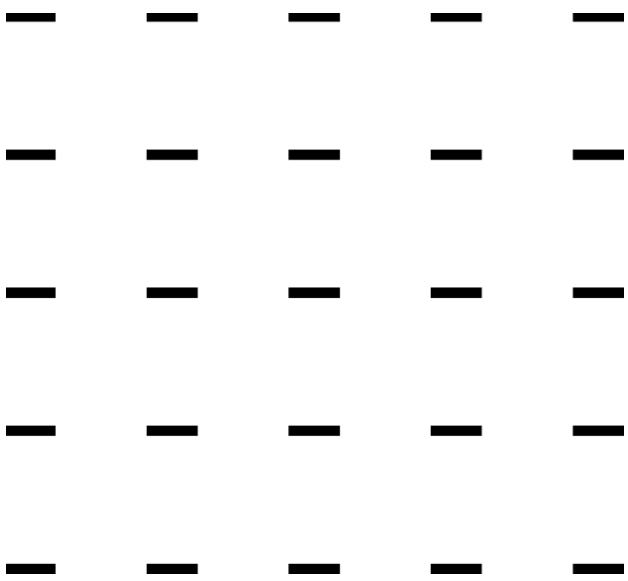

Figure 3.13 Bitmap of a rectangular nanohole array for focused ion beam fabrication.

3.3.4 Nanofabrication issues with focused ion beam

Astigmatism makes a challenge in obtaining a proper focus which will affect the shape and size of the subwavelength apertures. Astigmatism can cause changes in the fabricated samples. For example, instead of fabricating a circular nanohole we are obtaining an elliptical nanohole. In order to remove astigmatism, it is necessary to focus the ion beam properly. Focusing on a feature on the sample surface as an object can be a solution to this problem. As the magnification starts to increase is necessary to focus again and adjust the stigmator. This process has to be continued until a magnification of ten times higher than the final magnification has been reached.

3.3.5 Summary

Techniques like soft nanoimprint lithography, nanosphere lithography and electron beam lithography have been used to create nanohole arrays. The main advantage of FIB over those techniques is that it allows a precise tuning of the geometric parameters of the arrays. FIB provides a high degree of control and sample to sample reproducibility of the fabricated structures.

3.4 Photolithography

Photolithography is a process used in microfabrication that uses light to imprint a geometric pattern from a photomask to a light sensitive chemical photoresist (Figure 3.14).

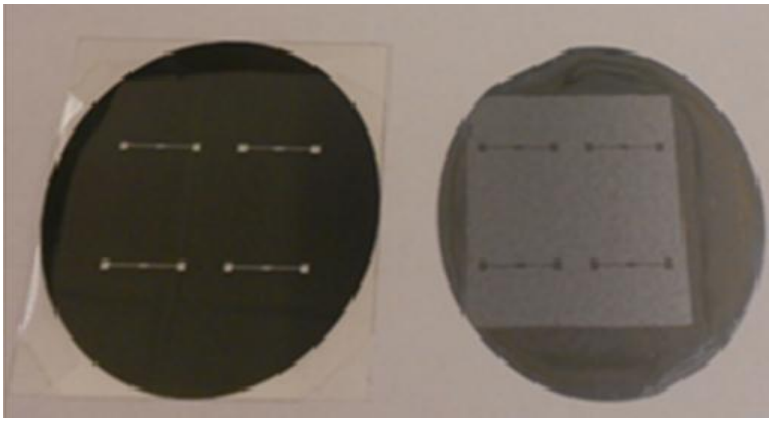

Figure 3.14 Photomask and a silicon wafer with a geometric pattern after using a photolithography process.

There are two types of photoresist: positive and negative (Figure 3.15). For positive photoresists, they become soluble after the exposure to the UV light. For negative photoresist, they behave in the opposite manner.

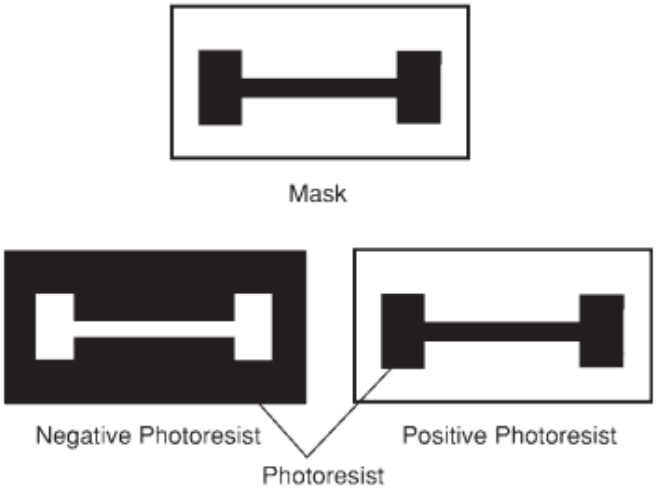

Figure 3.15 Resulting patterns after exposure and development of two types of photoresist: positive and negative [66].

The minimum size that can be achieved using photolithography is dictated by the scattering and diffraction of the photomask. The size of the area due to diffraction depends on the thickness of the layer of the photoresist and the wavelength of the incident light, which can be estimated by $\delta \approx 3\sqrt{\lambda h_{ph}}$, where λ is the wavelength of the incident light, h_{ph} is the height of the photoresist layer, and δ is the average width of the diffraction zone. The steps involved in the photolithographic process are: wafer cleaning, photoresist application, prebaking, photomask alignment, exposure, developing, and hard baking [66].

3.4.1 Wafer cleaning and photoresist application

Wafers are chemically cleaned in order to remove organic or inorganic contaminations on the surface. Before the photoresist is applied, a dehydration bake is performed to remove water from the surface of the wafer. After that, the wafer is covered with photoresist by spin coating (a spin speed between 1500 and 8000 rpm) that will produce a thin uniform layer of the photoresist on the wafer surface. The resulting polymer thickness is a function of spin speed, solution concentration, and molecular weight.

3.4.2 Prebaking

In this step, the photoresist coatings become photosensitive; an over prebaking will degrade the photosensitivity of the resists, and under prebaking will prevent light from reaching the sensitizer. A prebaking at 75-100 °C helps to promote adhesion of the photoresist layer to the wafer.

3.4.3 Mask alignment, exposure, developing, and hard baking

After prebaking, the mask is aligned with the wafer so the pattern can be transferred on to the wafer surface. Then the photoresist is exposed to a high intensity UV light. A post-exposure bake is performed before developing. Development can be done using a liquid (wet development), a gas, or plasma (dry development). For positive photoresists an aqueous alkaline solution (e.g., tetramethyl ammonium hydroxide) is used, for negative photoresists organic solvents are used. Finally, a hard baking is used to solidify the

remaining photoresist and make a more durable layer. Hard baking is usually done at higher temperatures (120°C) and for longer times than prebaking.

3.5 Microfluidics

Microfluidics deals with the manipulation of fluids that are constrained over micron or sub-micron length scales with precise control. Microfluidics is a vast and rapidly evolving research field in surface chemistry, biological analysis, and optics. Traditionally, silicon micromachining methods have been used to fabricate microfluidic channels from silicon and glass. Materials like Polydimethyl Dimethylsiloxane (PDMS) and Polymethyl Methacrylate (PMMA) have been employed successfully mainly because of their advantages like faster design times and low cost. Figure 3.16 shows an example of the integration of microfluidics with nanohole array sensors. Integration of nanohole arrays with microfluidics devices has evolved rapidly from single channel arrangements that facilitate fluid delivery to multiplexed arrays of nanohole arrays and service fluidics.

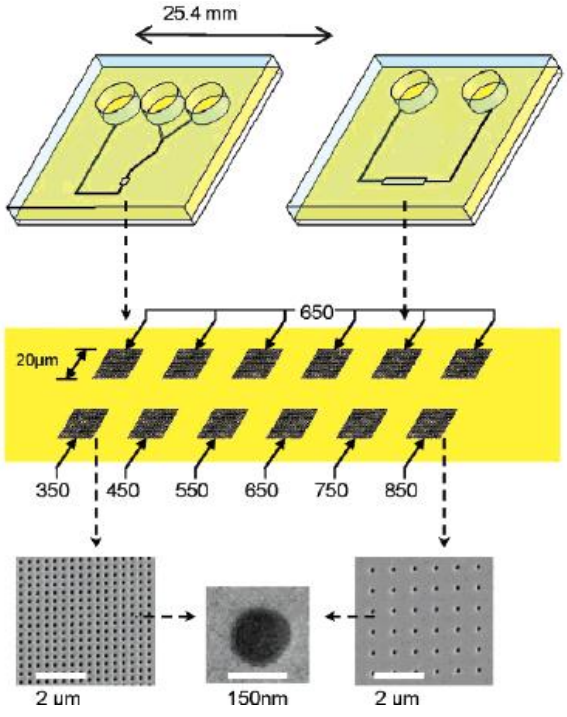

Figure 3.16 Schematic of a microfluidic chip embedded with nanohole arrays with different periodicities and the scanning electron microscopy images of the nanohole arrays [4].

3.5.1 Fabrication of microchip using PDMS

PDMS chips are commonly used in a microfluidic system to achieve the goal of lab-on-a chip. The use of PDMS has several advantages over silicon and glass. PDMS is inexpensive, flexible, optical transparent down to 230 nm, nontoxic, and features can be reproduced with high fidelity [67]. For our experiments of nanohole sensing, the designs of the microstructures were generated using computer aided design (CAD) software. By using transparencies printed from a high-resolution printer was possible to create the microstructures. To generate the master mold of the channel a transparency was used as a photomask in UV-photolithography. The master mold of the channel was patterned on a silicon wafer covered with SU-8 50 photoresist. For the development of the microchip a curing agent and PDMS (ratio 10:1) were used [68]. After peeling off the master the PDMS, it was possible to produce the final replica of the designed microstructures. Small holes were drilled into the PDMS to produce inlets and outlets. PDMS can seal to itself to a gold surface reversibly by conformal contact (via van der Waals forces) or irreversibly if the surfaces have been oxidized by plasma before contact. In our case, we used the first option. To ensure that there was no leakage the PDMS on the gold sample was sandwiched between two layers of hard acrylic PMMA (Figure 3.17).

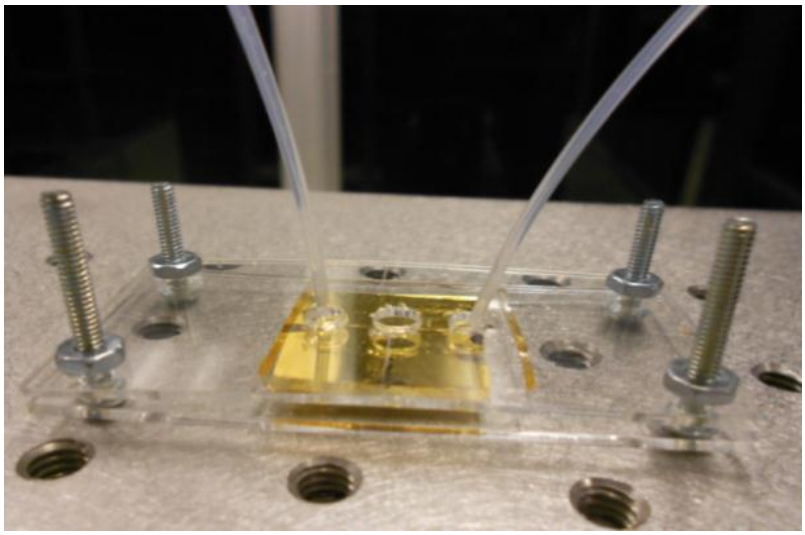

Figure 3.17 Microchip of a 500 nm thick gold film sample and with PDMS microfluidic over-channel sandwiched between acrylic layers.

3.5.2 Summary

Microfluidics devices integrated with nanohole arrays can be used as chemical and biological sensors. Integration of nanohole arrays with microfluidics devices has evolved rapidly from single channel arrangements that facilitate fluid delivery to multiplexed arrays of nanohole arrays and service fluidics.

3.6 Finite difference time domain

The finite difference time domain (FDTD) method was originally proposed in 1966 by Yee [69]. This numerical method is used for solving the Maxwell's curl equations in time domain for electric and magnetic fields. During the last years, FDTD method has become the most widely used simulation tool of electromagnetic phenomena and has been extensively applied to model and design circuits and photonic devices. We use a commercially available comprehensive FDTD simulating package (Lumerical FDTD) for the FDTD simulations. FDTD Solutions can calculate the electromagnetic fields as function of frequency or wavelength by performing Fourier transforms during the simulation. It has the ability to calculate a full range of useful quantities such as the Poynting vector, normalized transmission, and projections as a function of frequency or wavelength. For choosing the material, dispersive materials with tabulated refractive index (n,k) data as a function of wavelength can be used or alternatively specific theoretical models such as Drude can be used. To create a model of the actual experiment structure using Lumerical FDTD, material of the structure, appropriate simulation region and boundary conditions, sources and monitors have to be chosen [70].

3.6.1 Simulation boundaries

The boundary conditions that can be used to enclose the simulation region and that are supported by FDTD Solutions are perfectly matched layer (PML), metal, periodic, Bloch, symmetric and asymmetric (Figure 3.18). PML boundary conditions absorb electromagnetic energy incident upon them. PML can be used for absorbing the radiation at normal incidence; it can have significant reflection at grazing incidence. In order to solve this problem, it is necessary to increase the PML thickness. Metal boundary conditions are used for boundaries that are perfectly reflecting, this boundary condition

helps that no energy escapes the simulation region. Periodic boundary conditions are used when the electromagnetic fields and the structures that are analyzed are periodic and can be used in one or more directions. Bloch boundary conditions are used when the electromagnetic fields and the structures are periodic except for a phase shift between each period. The main advantage of Bloch boundary conditions is that can give the accurate reflection and transmission data when a plane wave is at an angle in a periodic structure. Symmetric and asymmetric boundary conditions are used when there are one or more planes of symmetry but both the structure and source must be symmetric. Symmetric boundary conditions are used as mirrors for the electric field and anti-mirrors for the magnetic field. Asymmetric boundary conditions are used as anti-mirrors for the electric field and mirrors for the magnetic field.

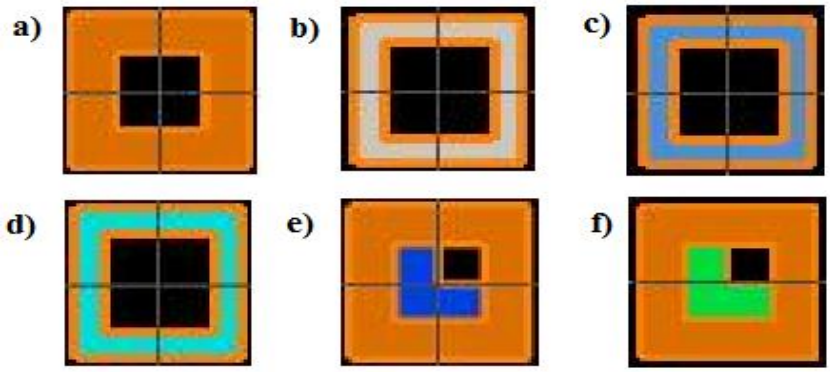

Figure 3.18 Boundary conditions of FDTD. a) Perfectly matched layer. b) Metal. c) Periodic. d) Bloch. e) Symmetric. f) Asymmetric

3.6.2 Excitation sources

The sources that can be supported by FDTD Solutions are plane wave, total-field scattered-field, mode, Gaussian, and point. A plane wave source is used to inject electromagnetic energy along a plane. A plane wave is the simplest source and can be used when the simulated structure is periodic. The total-field scattered-field source is used to separate the computation region into two regions. The first region contains the total field that is given by the sum of the scattered field and the incident field. The second region contains only the scattered field. A mode source is used to inject a guided mode into the FDTD simulation region. A Gaussian source defines the electromagnetic beam

radiation in a specific propagating direction. A point source is an oscillating dipole that acts as a source in Maxwell's equations to create electromagnetic fields. They can be placed at one or more points in the FDTD simulation region.

3.6.3 Mesh accuracy

A rectangular (Cartesian style) mesh is used in FDTD. A conformal mesh is used at metal boundaries to enforce an accurate boundary condition with a finite mesh grid and allows obtaining accurate results. A smaller mesh allows for more accurate results but the simulation time and memory will increase.

3.6.4 Monitors

The monitors that can be supported by FDTD Solutions are time-domain, index, global, movie, frequency-domain profile, frequency-domain power, and analysis groups. The time-domain monitors give the time-domain information for field components over the course of the simulation. The index monitors provides the n and k value as a function of the frequency or wavelength. The global monitor is where we can specify the resolution and range where we can obtain the frequency-domain information. A movie monitor can capture a desired field component over the FDTD region. Frequency-domain profile monitors will collect the field profile and data in the frequency domain from the simulation region. A frequency-domain power monitor can collect the power flow information in the frequency domain from the simulation data across some spatial region of the simulation. Analysis groups are used to group and process monitor data. The group object has a section that can contain code to set up the monitors and a section that can contain code to process the monitor data once the simulation is finished.

3.6.5 Transmission measurement using FDTD

The transmission function returns the amount of power that is transmitted through profile and power monitors that are normalized to the source power. The transmission is calculated by:

$$T(f) = \frac{\frac{1}{2}\int real(P(f)^{Monitor}) \cdot dS}{sourcepower} \tag{3.1}$$

where $T(f)$ is the normalized transmission as a function of frequency, $P(f)$ is the Poynting vector, and dS is the surface normal.

Figure 3.19 shows the simulation model of FDTD to measure the transmission spectra of circular nanohole arrays in a 100 gold film. To model the dispersive gold film a fit to the experimental data of Johnson and Christy was used [71]. The substrate was taken to have refractive index of 1.52 (for glass) and the refractive index of the background was varied to determine the sensitivity. The simulation domain used PML boundaries to prevent reflections and Bloch boundary conditions for the periodic structure. A plane wave source was used normally incident on the nanohole array. A frequency domain profile monitor collected the transmission through the holes in the visible and near infrared wavelength range. A mesh over-ride of 2 nm was used over the metal film, and this was confirmed to capture the SP dispersion by finite difference mode calculations. The sensitivity was determined by noting the change in the transmission characteristics for varying refractive index of the solution surrounding the holes (Figure 3.20).

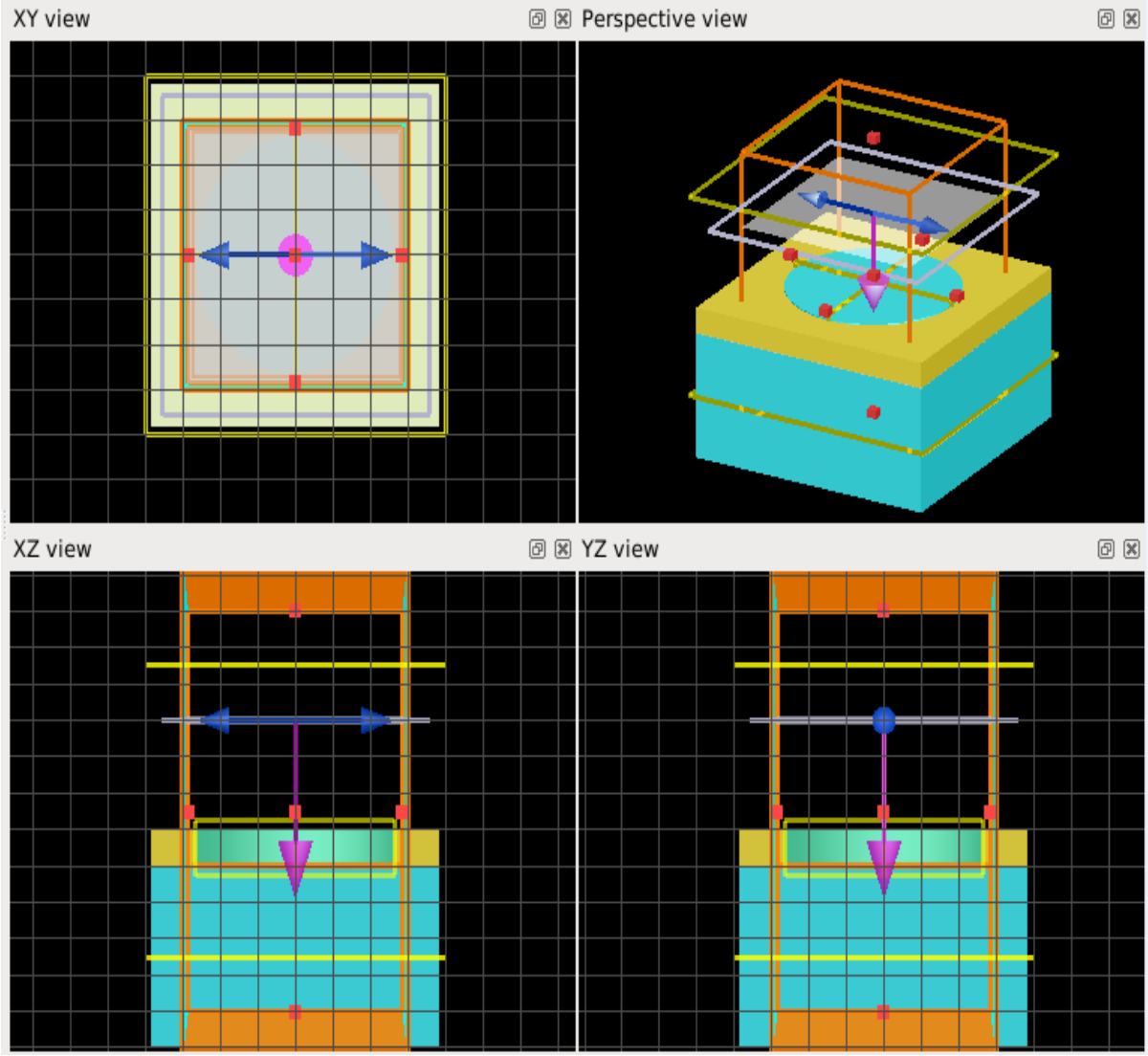

Figure 3.19 Simulation model of FDTD to measure the transmission spectra of circular nanohole arrays in a 100 nm gold film where Bloch boundary conditions was used and a plane wave source.

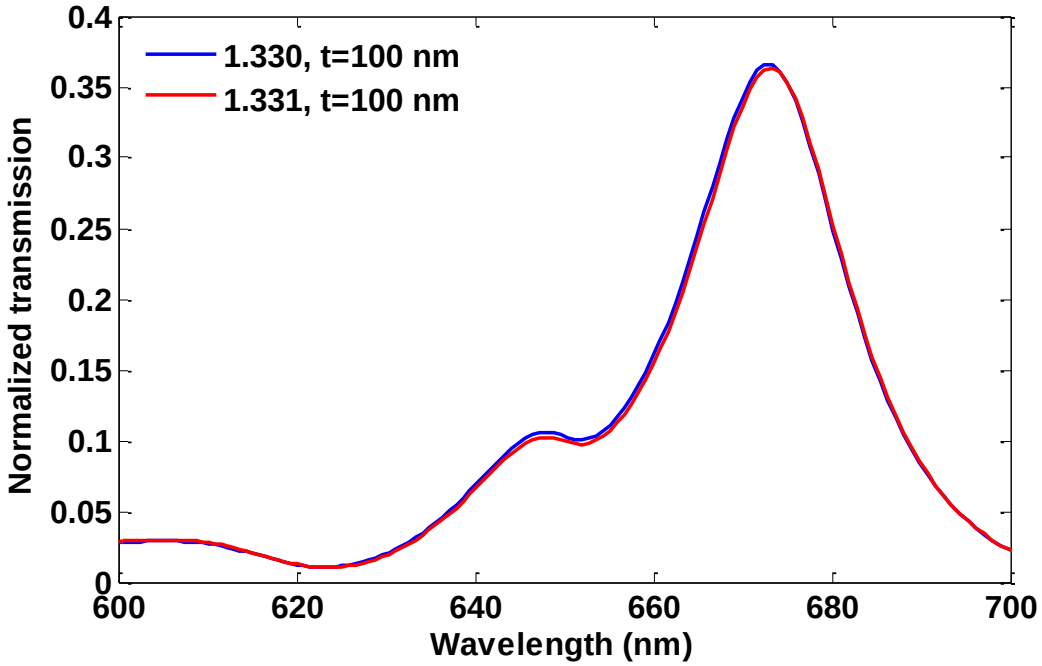

Figure 3.20 Transmission spectrum of a circular nanohole array of diameter 200 nm and periodicity 430 nm in a 100 nm gold film.

3.6.5 Summary

FDTD method has become the most widely used simulation tool of electromagnetic phenomena and has been extensively applied to model photonic structures because it predicts the behaviour of these structures prior to fabrication and actual experimental measurements. To create a model of the actual experiment structure using FDTD, material of the structure, appropriate simulation region, boundary conditions, sources, and monitors have to be chosen.

Chapter 4: Resolution optimization of a nanohole array sensor

An SPR sensor instrument consists of an optical system, supporting electronics, and a processing system. The main performance characteristics of SPR sensors include sensitivity, resolution, linearity, accuracy, and reproducibility [72].

Sensitivity of an SPR sensor is the ratio of the change in the sensor output to the change in the quantity to the measured (e.g., refractive index). Sensitivity to a refractive index S can be written as:

$$S = \frac{\delta Y}{\delta n_{ef}} \frac{\delta n_{ef}}{\delta n} \tag{4.1}$$

where Y denotes the sensor output. The first term describes the sensitivity of the sensor output (e.g., resonant angle or wavelength) to the effective index of a SP. The second term describes the sensitivity of the effective index of a SP to the refractive index. The second term is independent of the method of excitation [73].

Resolution is a key performance of an SPR sensor and limits the level of detection. Resolution is defined by the smallest change in the bulk refractive index that produces a detectable change in the sensor output. Resolution is limited by the noise in the intensity of the detected light. Dominant sources of noise are the fluctuations in the light intensity emitted by the light source, shot noise, and noise generated in the electronic circuitry of the detector. The shot noise is associated with the random arrival of photons on a detector and, in accordance with Poisson statistics; and is directly proportional to the square root of the detected light intensity. The detector noise is mainly generated from the electronic circuitry and is independent of the detected light intensity.

Improvements in the resolution of SPR sensors will allow the detection of lower concentration levels. The fundamental limit of the resolution of an SPR sensor system is set by the shot noise, as will be discussed below. So signal acquiring techniques and data processing algorithms are developed to minimize the effect of shot noise.

In this work, we optimize the resolution of nanohole arrays in metal films for refractive index sensing by increasing the sensitivity with modifications to the hole-array parameters and by reducing the noise of the sensor system. We achieve a bulk resolution of 4.45×10^{-7} RIU using a fast detector to monitor the change in transmission intensity. Theory of signal to noise ratio (SNR) for intensity imaging, the design of the nanohole arrays, the experimental setup, and the results that were obtained are presented in this chapter.

4.1 Calculation of the signal to noise ratio of a CCD camera

The following equation is commonly used to calculate the SNR of a CCD camera:

$$SNR = \frac{PQ_e t}{\sqrt{PQ_e t + Dt + Nr^2}} \tag{4.2}$$

where P is the incident photon flux (photons/pixel/second), Q_e represents the CCD quantum efficiency, D is the dark current value (electrons/pixel/second), t is the integration time (seconds), and Nr represents the readout noise (electrons rms/pixel) [74].

The dark noise and readout noise in high signal operations can be smaller than the shot noise so they can be considered negligible according to Equation 4.3.

$$SNR = \frac{PQ_e t}{\sqrt{PQ_e t}} \tag{4.3}$$

At higher intensities the detector overcomes readout noise and dark current noise of the detector so the shot noise can be limited [75]. Higher intensities allow higher photon collection efficiency and an improvement of the SNR and therefore an improvement of the resolution of a SPR sensor.

In the field of SPR sensors to reduce the light intensity noise during the data processing two types of averaging can be used. The averaging involves temporal or spatial averaging. When a time sequence of light intensities is averaged for each detector (e.g., CCD frames are averaged over time) is called temporal averaging. In time domain, all noise contributions behave independently. When light intensities measured with N detectors (e.g., detector pixels within one sensing channel) is called spatial averaging. Time averaging reduces the noise in the intensity of light by a factor of $\sqrt{M}$, where M is the number of averaged intensities in a certain span of time. Higher SNR can be obtained by advanced detectors with faster data transmission rates. The spatial averaging of N detector pixels used in SPR sensors the uncorrelated portion of noise is reduced, while the light intensity fluctuations that are correlated are not affected. Spatial averaging is less efficient and light fluctuations affect all the measured intensities in the same way and therefore cannot be eliminated by the spatial averaging [10].

4.2 Simulation methods of nanohole arrays and results

Periodicity of the array, hole-diameter, and metal thickness were varied to obtain the best performance of the nanohole array sensor. The simulation domain used perfectly matched layer boundaries to prevent reflections and Bloch boundary conditions for the periodic structure. A plane wave source was used normally incident on the nanohole array. A frequency domain profile monitor collected the transmission through the holes in the visible and near infrared wavelength range. A mesh over-ride of 2 nm was used over the metal film. The sensitivity was determined by noting the change in the transmission characteristics for varying refractive index of the solution surrounding the holes.

FDTD simulations were carried out for hole-diameters from 140 nm to 270 nm, periodicities from 415 nm to 575 nm, and gold film thicknesses from 100 nm to 500 nm.

Figure 4.1 shows the transmission spectrum of the optimized nanohole arrays for film thickness of 100 nm. The optimization was determined in terms of the resolution, assuming that shot noise is the dominant factor (For which the noise scales as the square root of the intensity). Considering this, the resolution, when changing the refractive index from $n_1 = 1.330$ to $n_2 = 1.331$ will be proportional to the resolution parameter, R:

$$R = \left| \frac{I_{n1} - I_{n2}}{\sqrt{I_{n1}}} \right| \tag{4.4}$$

Using Equation 4.4, we compare the performance between the nanohole arrays, where I_{n1} and I_{n2} are the transmission intensities for the different refractive index values.

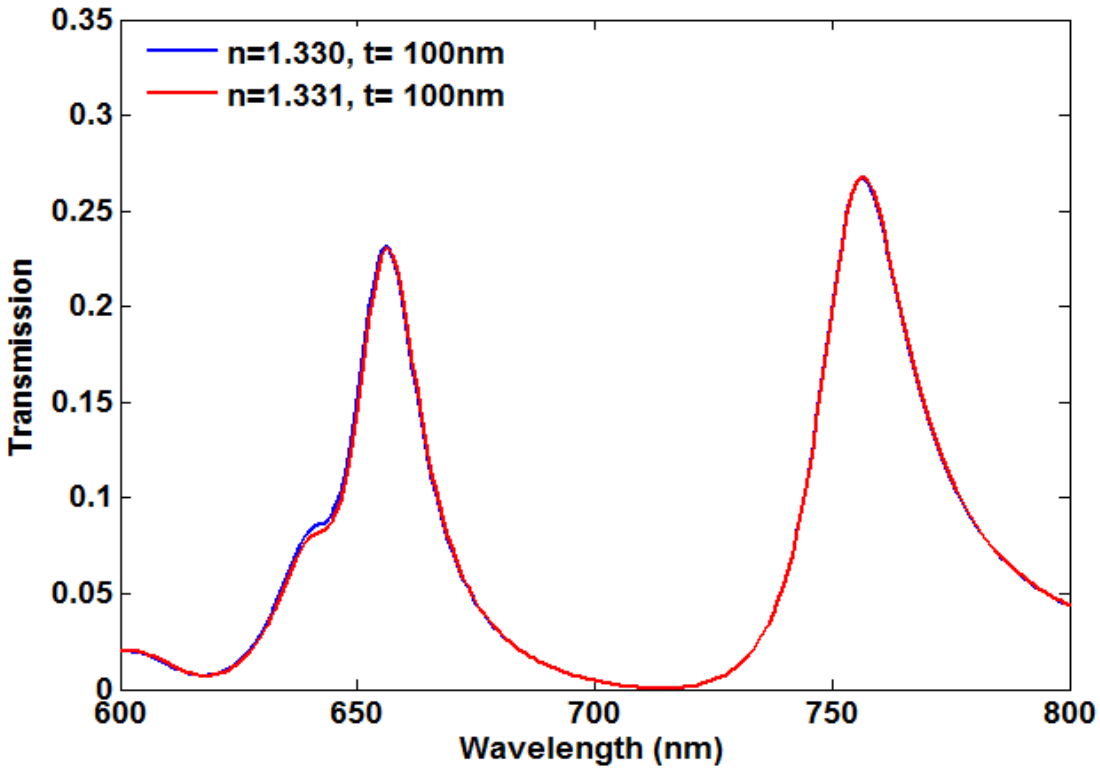

Figure 4.1 Spectrum of a circular nanohole array with diameter 150 nm and periodicity 425 nm in a 100 thick gold film.

Figure 4.2 shows that the optimal wavelength for operation is at 648 nm for this film thickness, and this occurs for a hole-diameter of 150 nm and a periodicity of 425 nm.

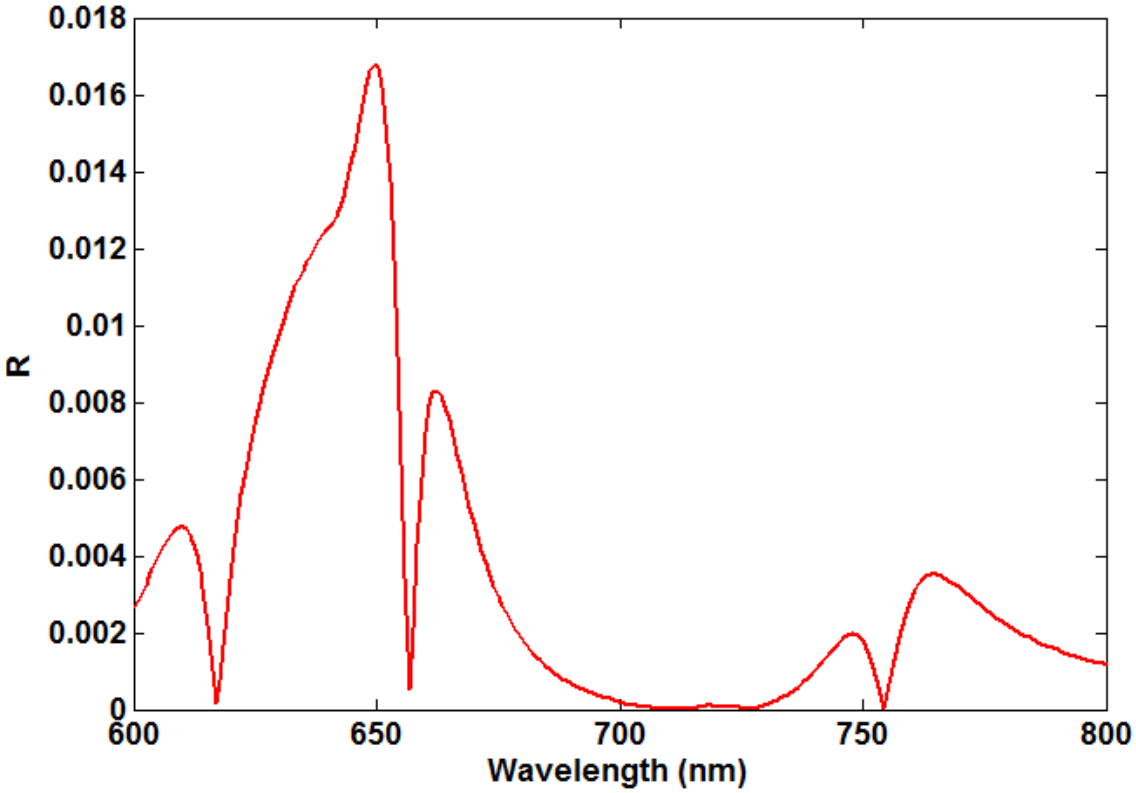

Figure 4.2 Optimal wavelength for operation is at 648 nm for a circular nanohole array with diameter 150 nm and periodicity 425 nm in a 100 nm thick gold film.

It is interesting to note here that the optimal periodicity for the 100 nm film is close to the expected lowest order Bragg resonance of the plasmon dispersion for this wavelength (Equation 2.4); however, this is not the case for the thicker films.

Figure 4.3 shows the transmission spectrum of the optimized nanohole arrays for film thickness of 300 nm. The optimal parameters found were hole-diameter of 260 nm, periodicity of 570 nm. The wavelength for the best performance was 655 nm (Figure 4.4).

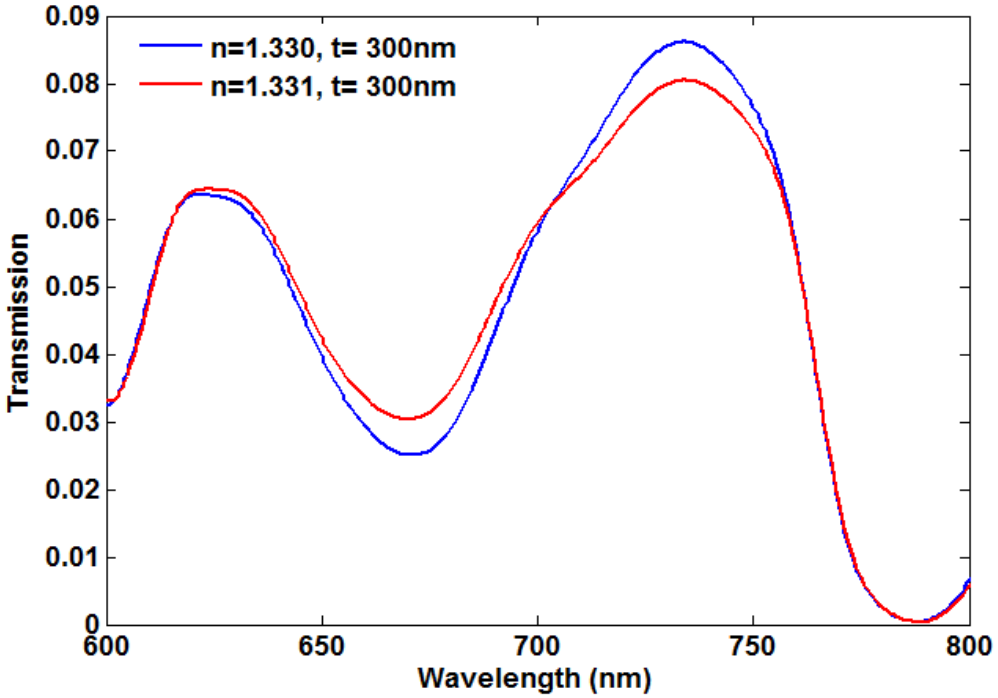

Figure 4.3 Spectrum of a circular nanohole array of diameter 260 nm and periodicity 570 nm in a 300 nm thick gold film.

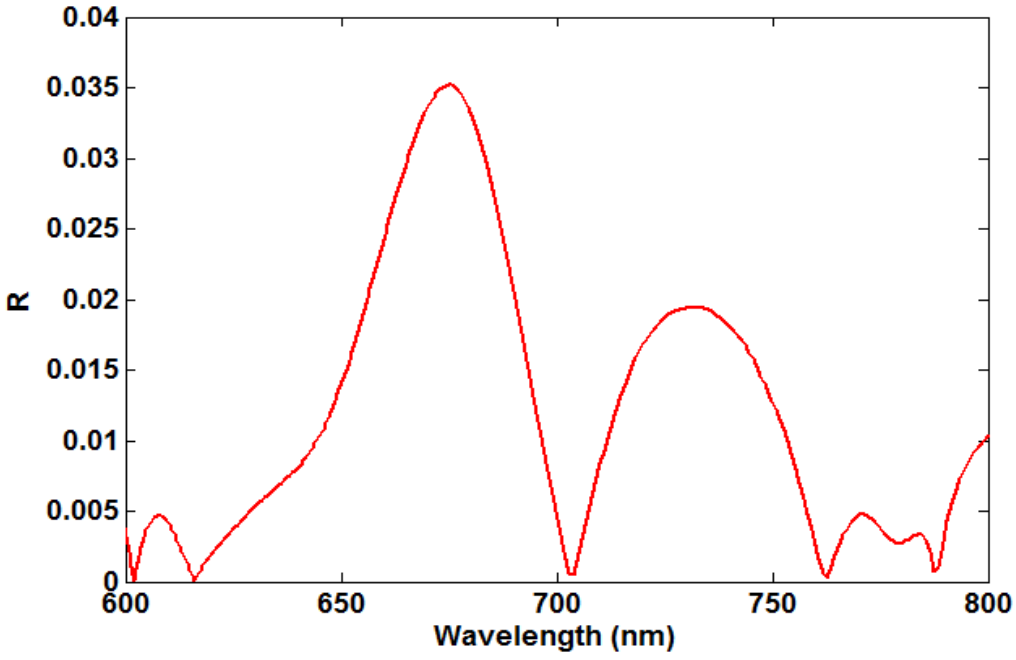

Figure 4.4 Optimal wavelength for operation is at 655 nm for a circular nanohole array with diameter 260 nm and periodicity 570 nm in a 300 nm thick gold film.

Figure 4.5 shows the transmission spectrum and resolution parameter for a 500 nm gold film thickness. The optimal parameters for this thickness were hole-diameter of 260 nm and periodicity of 570 nm. The largest R value change is at the wavelength of 655 nm (Figure 4.6).

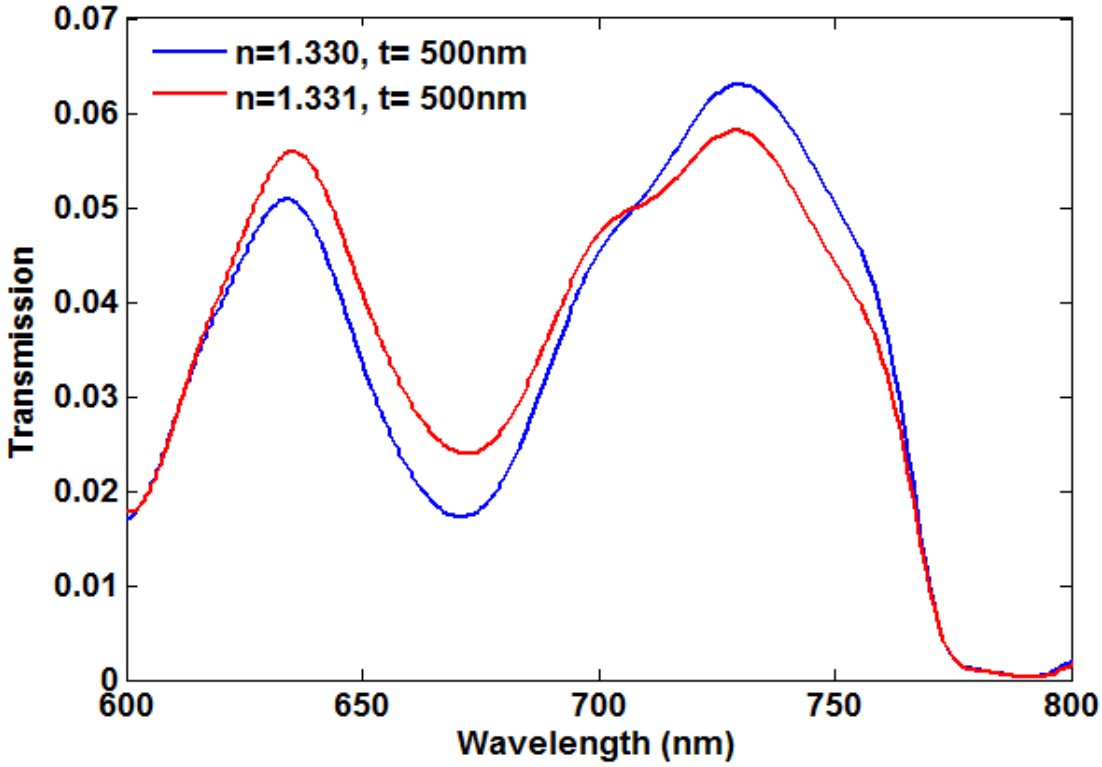

Figure 4.5 Spectrum of a circular nanohole array of diameter 260 nm and periodicity 570 nm in a 500 nm thick gold film.

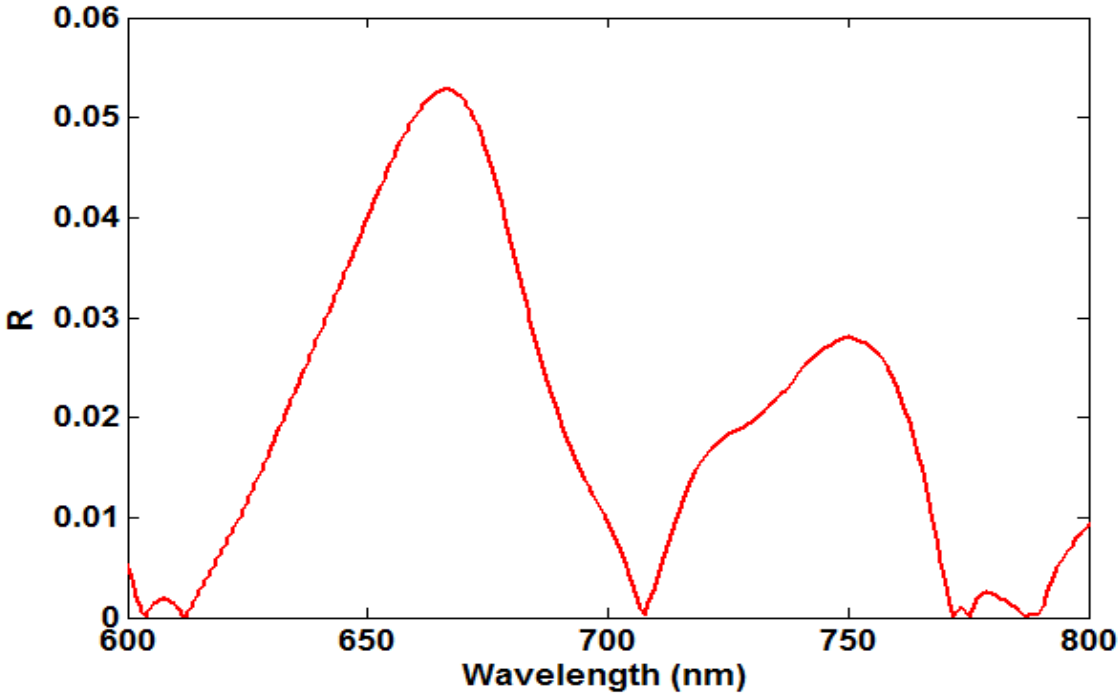

Figure 4.6 Optimal wavelength for operation is at 655 nm for a circular nanohole array with diameter 260 nm and periodicity 570 nm in a 500 nm thick gold film.

Comparing Figures 4.2, 4.4 and 4.6, it is clear that the thicker films provide better performance. In practice, however, we are limited by the ability to make high-aspect nanoholes in thick films and the duration of milling, and so we do not attempt larger thicknesses than 500 nm in this work.

It is also interesting to note that the optimal wavelength of operation was consistently around 655 nm for all of the film thicknesses, and this has important ramifications for the sensor performance.

4.3 Nanohole arrays fabrication

The nanohole arrays were fabricated by using a FB-2100 (Hitachi) focused ion beam with a gallium ion source. The ion beam was set to 40 keV for milling, and a beam current of 0.01 nA. To match the simulations, the nanohole arrays were milled in film thicknesses

of 100 nm, 300 nm and 500 nm. Figure 4.7 shows a SEM image of a circular nanohole array with a diameter of 270 nm in a 300 nm thick gold film.

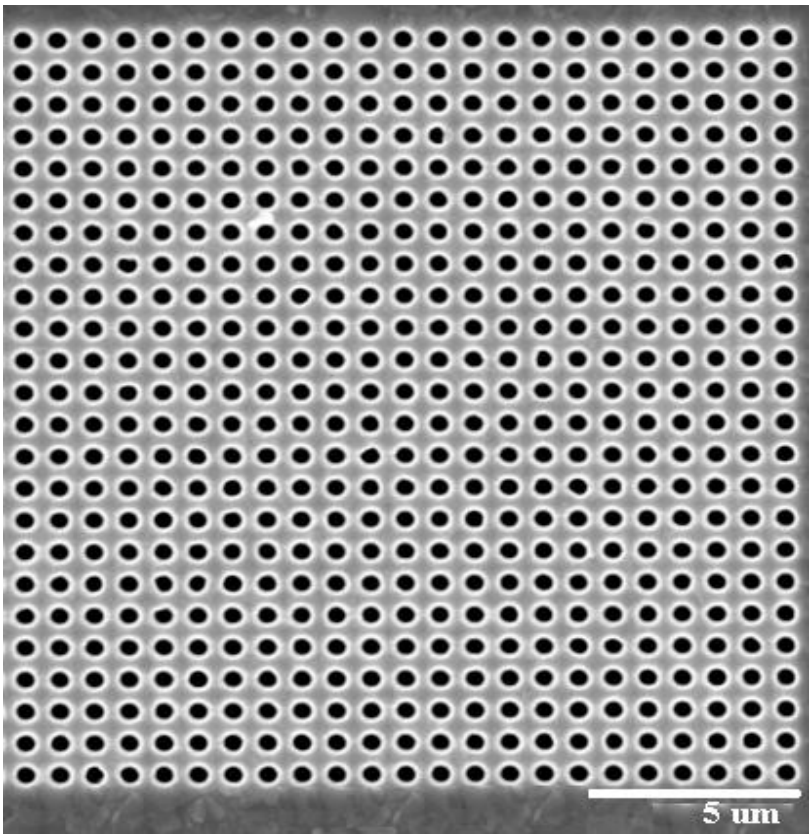

Figure 4.7 Scanning electron microscope image of circular nanohole arrays with a diameter of 270 nm in a 300 nm thick gold film.

Figure 4.8 shows a SEM image of a circular nanohole array with a diameter of 260 nm in a 500 nm thick gold film.

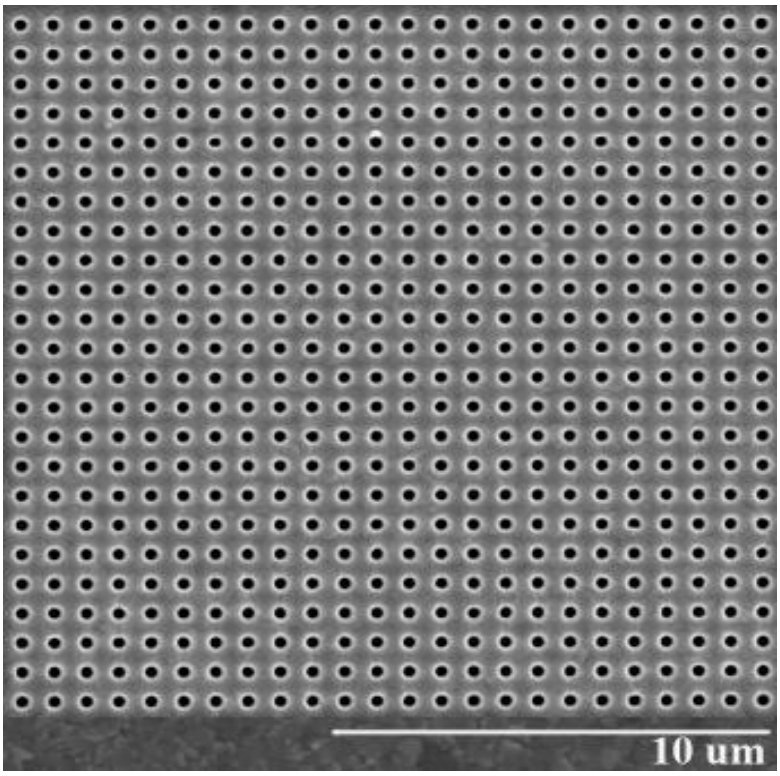

Figure 4.8 Scanning electron microscope image of circular nanohole arrays with a diameter of 260 nm and a periodicity of 570 nm in a 500 nm thick gold film.

Due to the cost of fabrication, the simulations were used to reduce the range of fabrication parameters. For the 100 nm film thickness, the periodicity was scanned from 415 nm to 435 nm in steps of 5 nm and the diameters used were 150 nm and 160 nm. For the 300 nm and 500 nm film thicknesses, the diameters used were 260 nm and 270 nm and the periodicity was scanned from 550 nm to 575 nm in steps of 5 nm.

Good verticality of the side-walls of thick gold films was confirmed by energy dispersive X-ray spectroscopy studies (Figure 4.9), which showed that the gold was removed from the region of precisely (to within 5 nm) the specified radius.

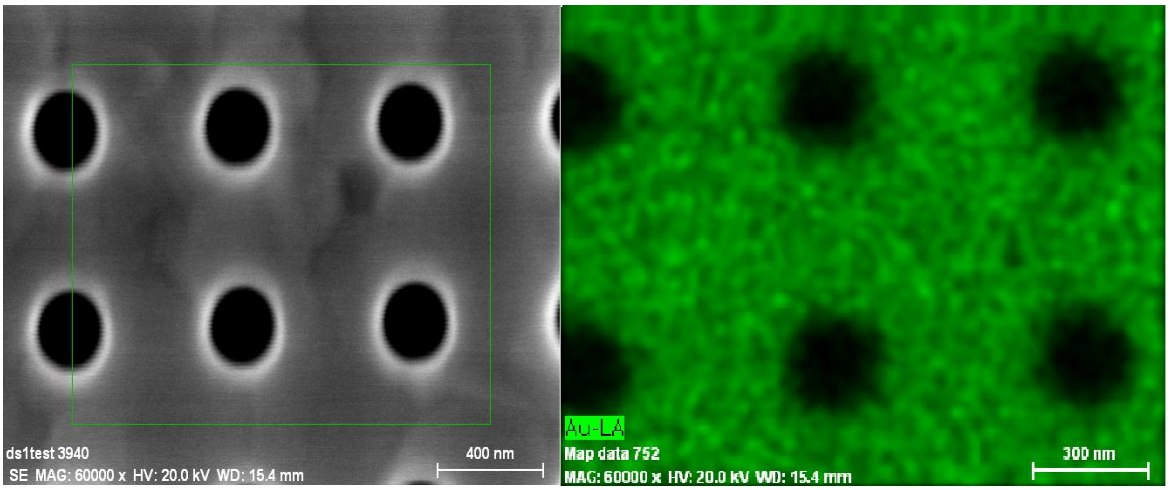

Figure 4.9 Energy dispersive X-ray image of circular nanohole arrays with a diameter of 260 nm and a periodicity of 570 nm in a 500 nm thick gold film.

4.4 Experimental setup for bulk sensing

Figure 4.10 shows the microchip that was used for measuring the change in intensity with refractive index change for nanohole arrays in a 100 nm, 300 nm, and 500 nm gold films.

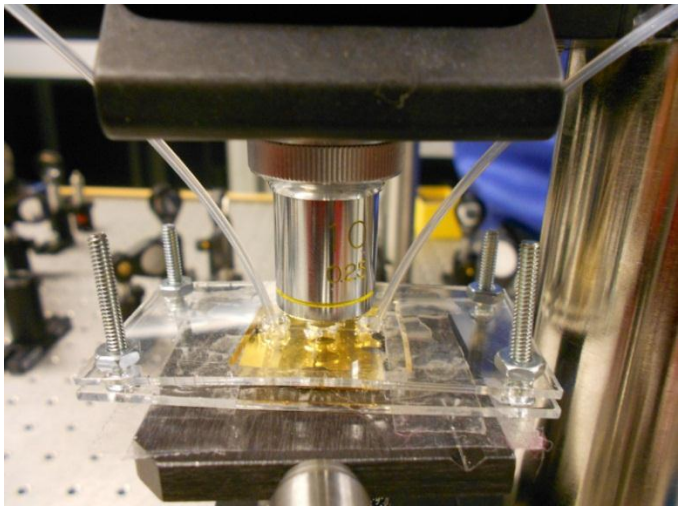

Figure 4.10 Microchip made by rapid prototyping lithography. A gold sample is sandwiched between two acrylic layers.

Figure 4.12 shows the experimental setup for measuring the fabricated gold samples. To enable scanning over a wide range of wavelengths, a supercontinuum light source

(Fianium SC400) was used. With the acousto-optic tunable filter (AOTF), any desired wavelength ranging from 400 nm to 1100 nm could be obtained. This source illuminated the top surface of the sub-wavelength apertures. A spatial filter was used to improve the spatial/spectral quality of the laser beam. Two objective lenses had been set up to measure the transmission of the nanohole arrays. First, the laser beam was focused using a microscope objective of 0.1 NA, and then it was collected with a microscope objective of 0.5 NA. We experimented with various objective lens combinations, and we found that this is a good configuration. In particular, the high NA objective below the glass substrate helps to acquire a larger number of photons (Figure 4.11). By contrast, the low NA objective above the microfluidic channel ensures a low angular deviation in the incident photons, so that the resonances (that are angle-sensitive) are more spectrally pure [20].

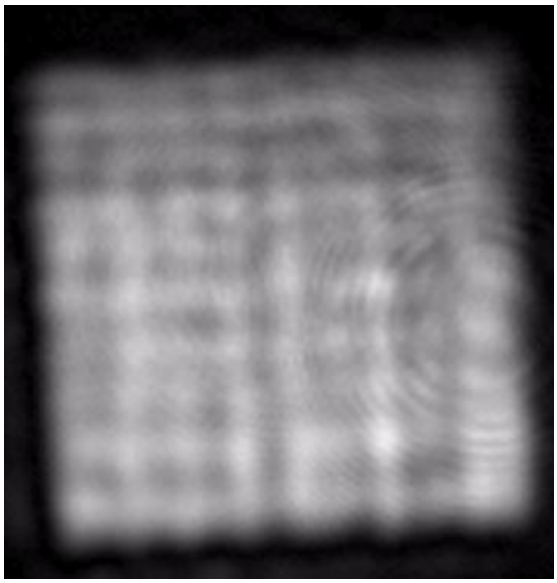

Figure 4.11 Image of a circular nanohole array in a 500 nm thick gold film captured on a CCD camera.

A CCD camera (Thorlabs DCU224C) was used to record a video of the sub-wavelength structures while flowing solutions of slightly different refractive index over the sample. Any change in the refractive index of the solution appears as a change in intensity. A syringe pump (Harvard apparatus 11 series) was used for a stable liquid flow rate of 7 µL/min. Avi video clips were recorded and the intensity change was measured using a MATLAB program [Appendix C].

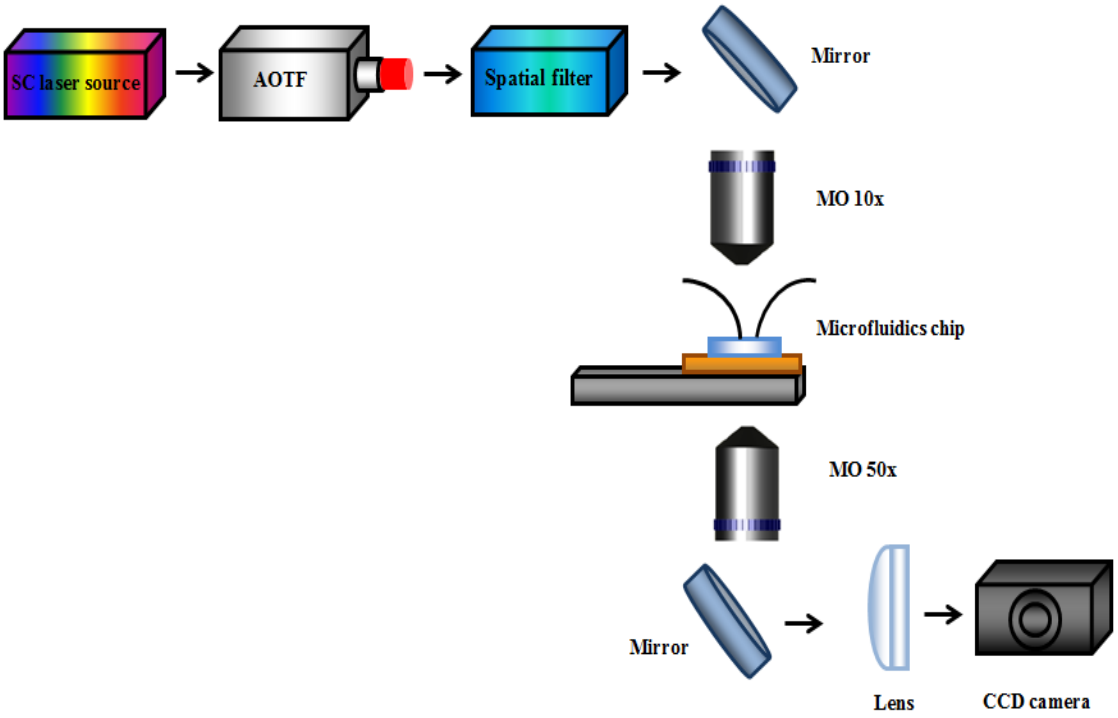

Figure 4.12 Schematic of optical setup used for measuring the change in intensity of the fabricated gold samples with a super continuum laser source tunable over the visible near infrared region.

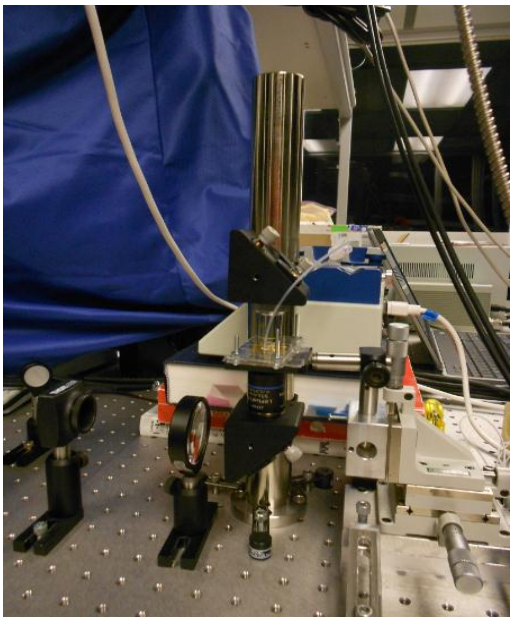

Figure 4.13 Image of the experimental setup for measuring the change in intensity with refractive index change.

4.5 Sensitivity optimization

In order to optimize the sensitivity of a nanohole array, it is important to determine at which wavelength is possible to obtain the highest difference of refractive indexes. Using the AOTF is possible to scan a wavelength range in real time while different refractive indexes are flowing through nanohole arrays. Figure 4.14 shows the wavelength scanning of a circular nanohole array with a diameter 270 nm and a periodicity of 550 nm in a 300 nm thick gold film while different refractive indexes were flowing. Figure 4.14 has a staircase appearance because it was acquired by scanning the AOTF in 5 nm steps for 5 second duration at each step. For convenience, the figure is plotted versus wavelength instead of time.

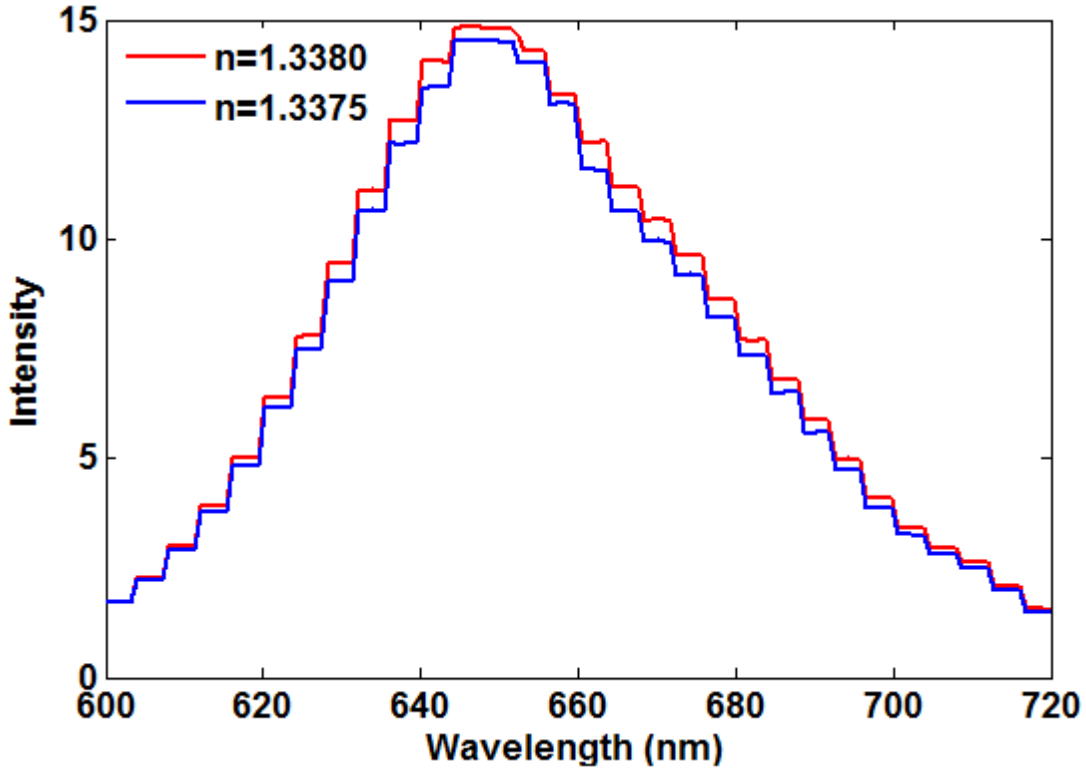

Figure 4.14 Representation in time of the spectrum of a circular nanohole array with a diameter of 270 nm and a periodicity of 550 nm in a 300 nm thick gold film for two different refractive index solutions.

Figure 4.15 shows the best result obtained among all the arrays, varying the refractive index to determine the sensitivity. Figure 4.15 corresponds to a circular nanohole array with a diameter of 260 nm with a periodicity of 570 nm in a 500 nm thick gold film.

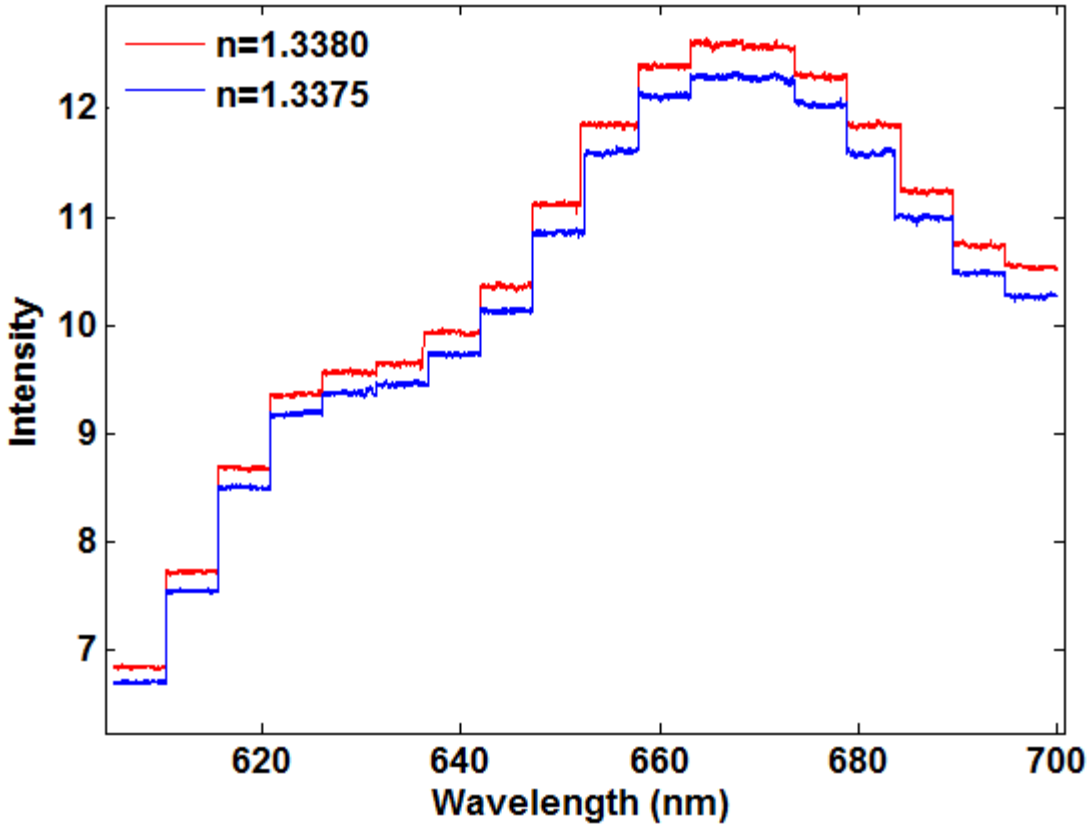

Figure 4.15 Representation in time of the spectrum of a circular nanohole array with a diameter of 260 nm with a periodicity of 570 nm in a 500 nm thick gold film for two different refractive index solutions.

Figure 4.16 shows optimal wavelength operation of the circular nanohole arrays subjected to refractive index change of 0.0005 is around at 655 nm.

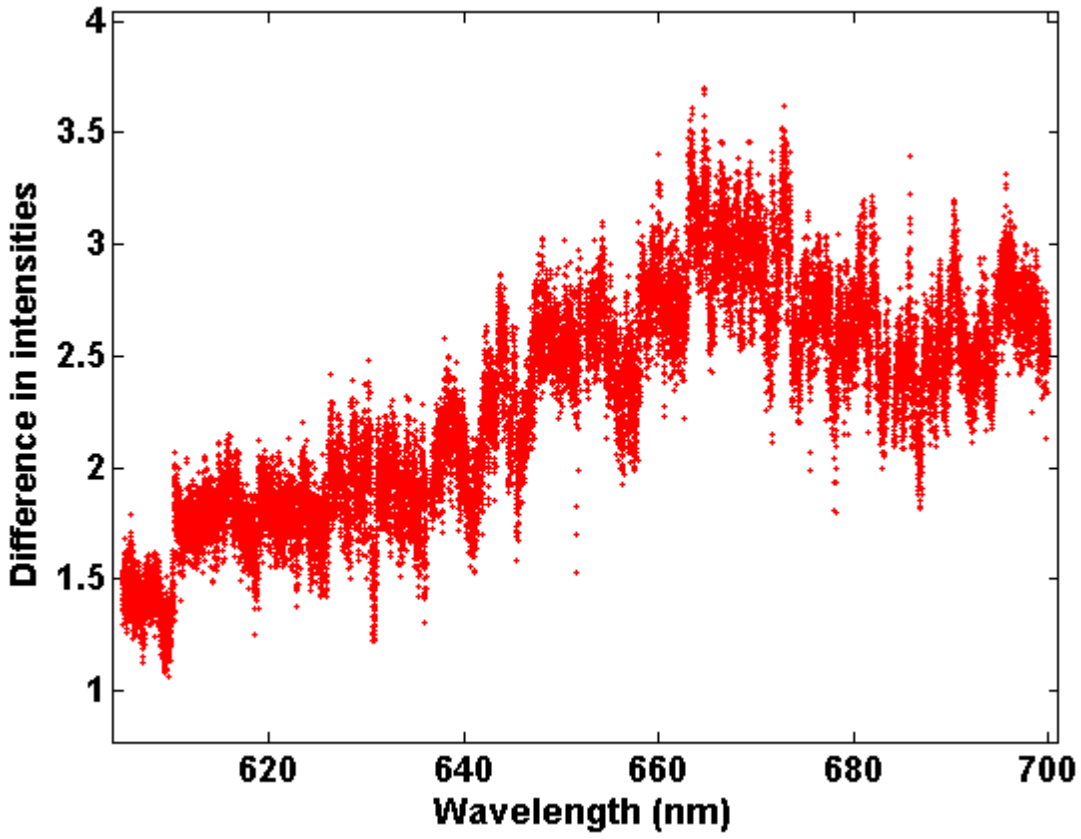

Figure 4.16 Difference in intensities of two refractive index solutions for a circular nanohole array with a diameter of 260 nm with a periodicity of 570 nm in a 500 nm thick gold film.

After choosing the optimal wavelength of operation for the nanohole array sensor measurements, by the procedure in Figure 4.15, bulk sensitivity measurements were carried out with a higher intensity of 3.6 mW and using a low-pass finite impulse response numerical filter. The numerical filtering reduced the time resolution to 0.5 frames per second. The highest resolution that was obtained was 6×10^{-7} RIU.

Resolution can be defined as:

$$Resolution = \frac{\Delta n}{SNR} \tag{4.5}$$

where Δn is the difference between refractive indexes (n_1 and n_2) and SNR is the signal to noise ratio. The SNR is determinate by taking the difference between the mean value of the signal for the top and bottom part of each step divided by the standard deviation of the standard deviation of the signal at those levels.

In the experiments, the 100 nm thick gold film showed the largest sensitivity for a hole-diameter of 150 nm and periodicity of 425 nm, with a resolution of 2×10^{-6} RIU (Figure 4.17). The fall in the intensity around 35s (Figure 4.17) is due to the change in the refractive index of the solution flowing through the PDMS channel.

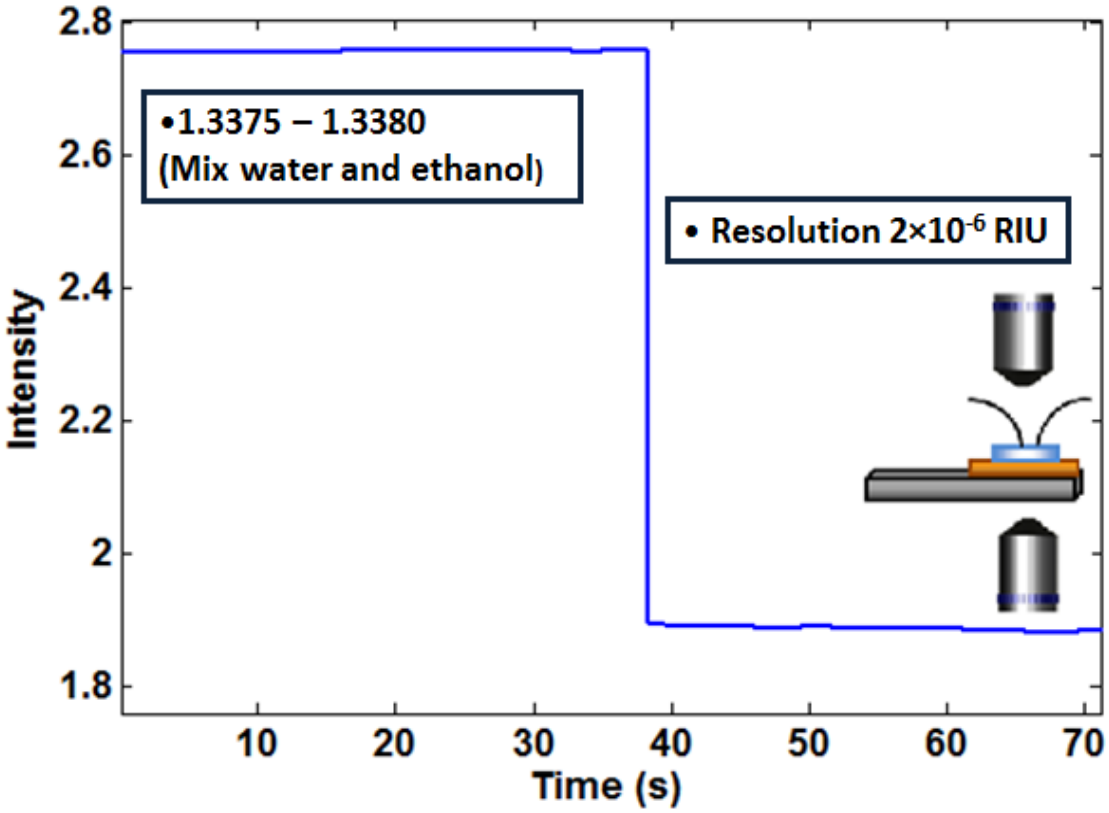

Figure 4.17 Experimental results for measuring the change in intensity at 648 nm wavelength for a 100 nm thick gold film. An array of circular holes with diameter of 150 nm and periodicity of 425 nm were used.

The 300 nm thick film showed largest sensitivity for a hole-diameter of 260 nm and periodicity of 570 nm with a resolution of 8.49×10^{-7} RIU (Figure 4.18).

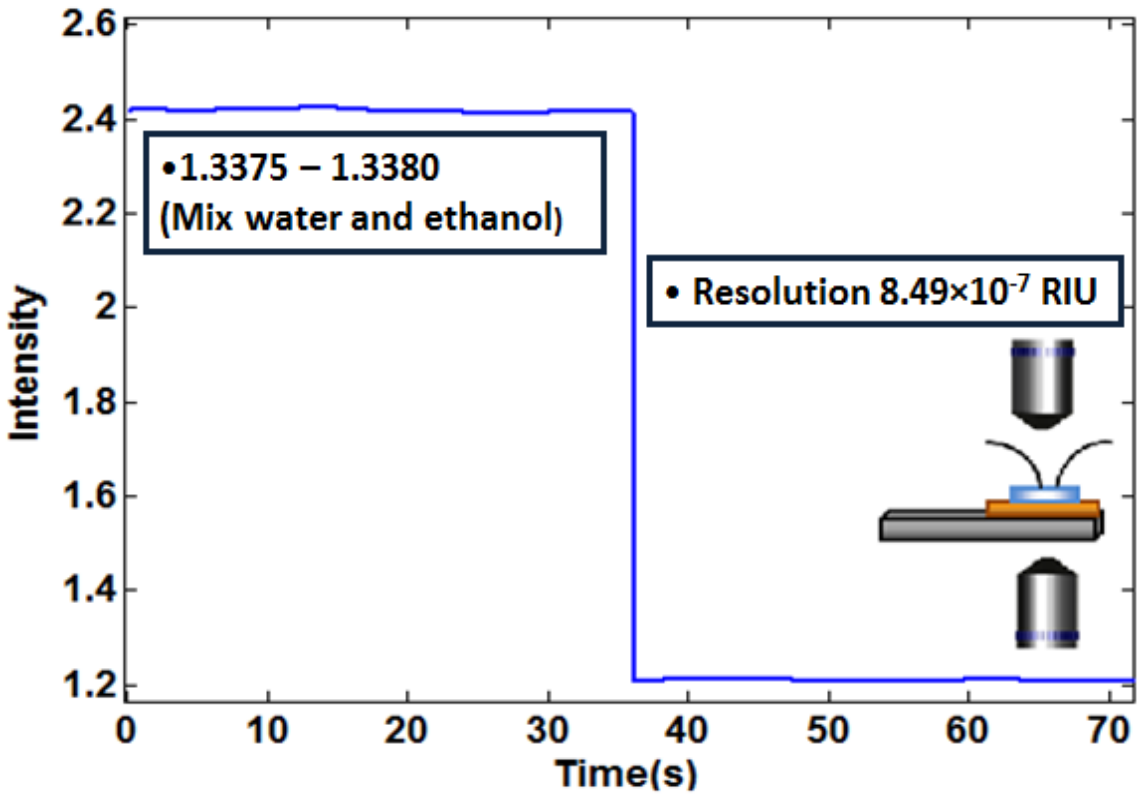

Figure 4.18 Experimental results for measuring the change in intensity at 655 nm wavelength for a 300 nm thick gold film. An array of circular holes with diameter of 260 nm and periodicity of 570 nm were used.

The 500 nm thick film showed the largest sensitivity for a hole-diameter of 260 nm and periodicity of 570 nm, with a resolution of 6×10^{-7} RIU (Figure 4.19). These parameter values are all in close-agreement with the simulation results. It is clear also that the thicker film gives better resolution, as expected from the simulations.

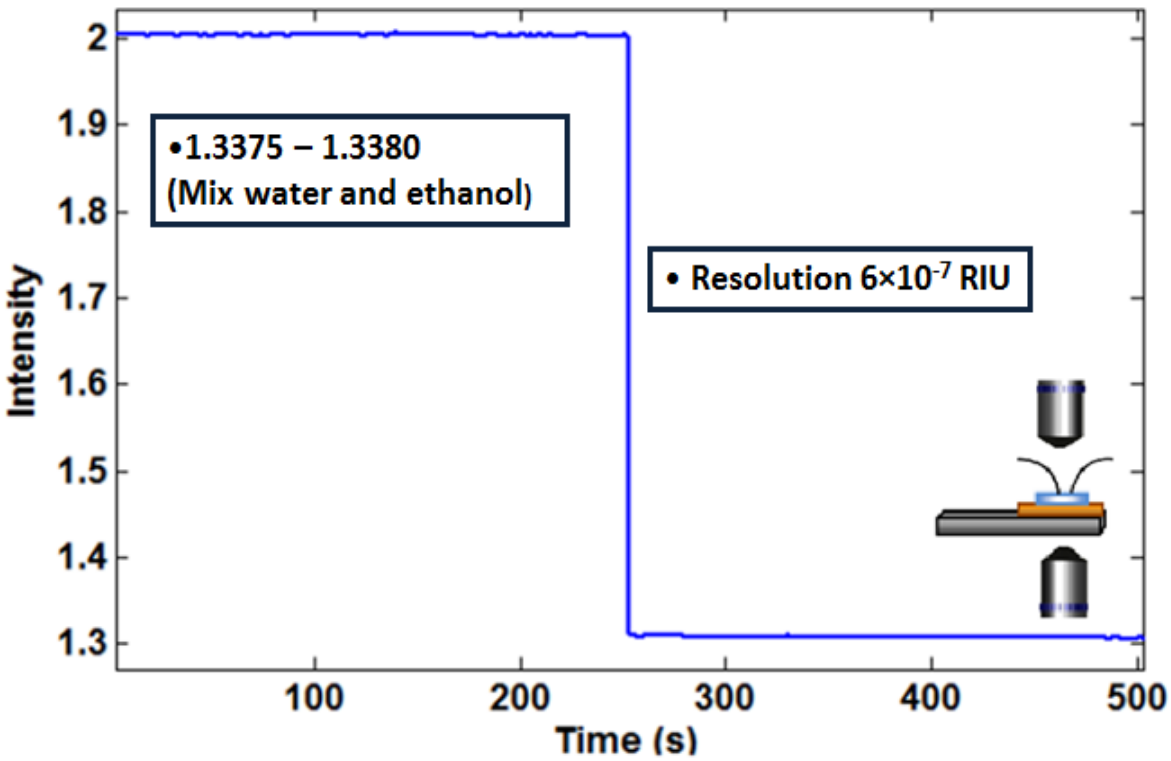

Figure 4.19 Experimental results for measuring the change in intensity at 655 nm wavelength for a 500 nm thick gold film. An array of circular holes with diameter of 260 nm and periodicity of 570 nm were used.

4.6 Improvement in bulk sensing

Miniaturization and low cost are some of the most essential requirements of a sensing device in addition to higher values of performance parameter. Laser sources are not cost effective and for commercial purposes it does not seem to be suitable. If a laser diode is used as a source the sensing device can be compact with an advantage of low cost. Laser diodes are able to give a more stable output intensity compared to lasers [56, 76].

Figure 4.19 showed that for a500 nm thick film of nanohole array with a diameter of 260 nm and periodicity of 570 nm had a resolution of 6×10^{-7} RIU using a 655 nm wavelength. We decided to replace the laser source for a laser diode with a high power (until 100 mW) so it will increase the intensity and replaced the camera by an advanced detector with faster data transmission rate (Prosilica GC).

Figure 4.20 shows a laser diode for a wavelength of 655 nm that illuminated the top surface of the sub-wavelength apertures. Again two objective lenses had been set up to measure the transmission of the nanohole arrays. First, the beam was focused using a microscope objective of 0.1 NA, and then it was collected with a microscope objective of 0.5 NA. A CCD camera (Prosilica GC) was used to record a video of the sub-wavelength structures while flowing solutions of slightly different refractive index over the sample. A syringe pump (Harvard apparatus 11 series) was used for a stable liquid flow rate of 7 µL/min.

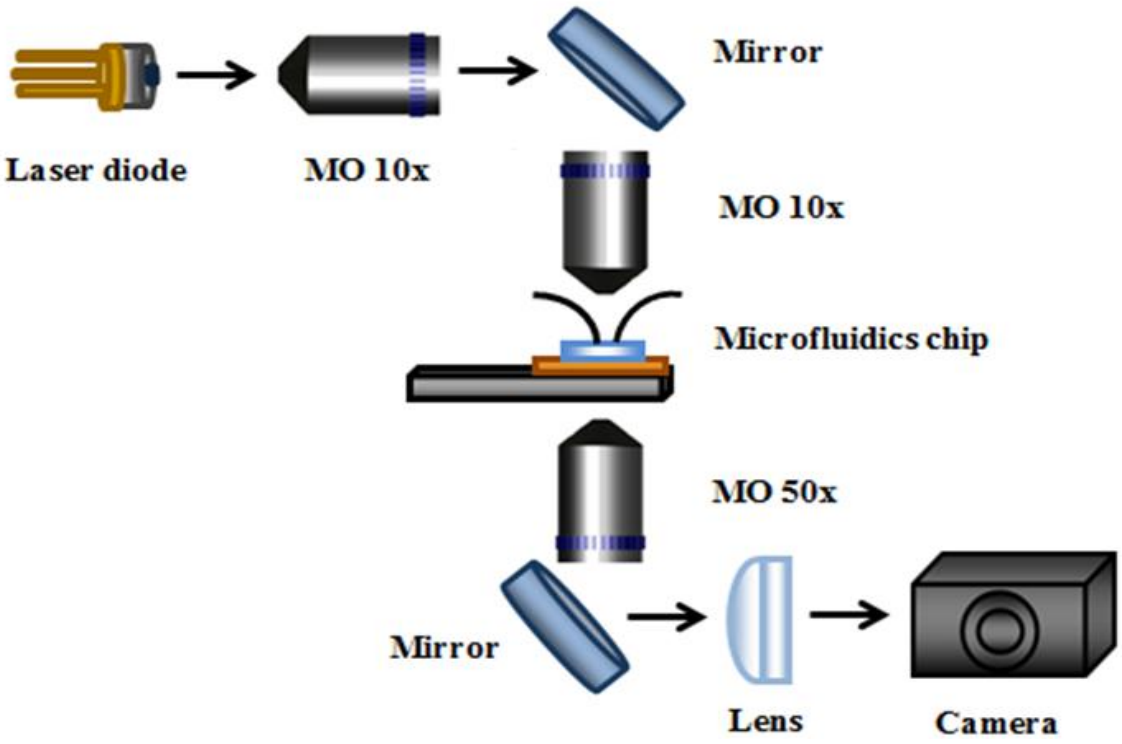

Figure 4.20 Schematic of optical setup used for measuring the change in intensity of the fabricated gold samples with a laser diode source.

Using the nanohole arrays with a diameter of 260 nm and periodicity of 570 nm in a 500 thick gold film had a resolution of 4.45×10^{-7} RIU (Figure 4.21).

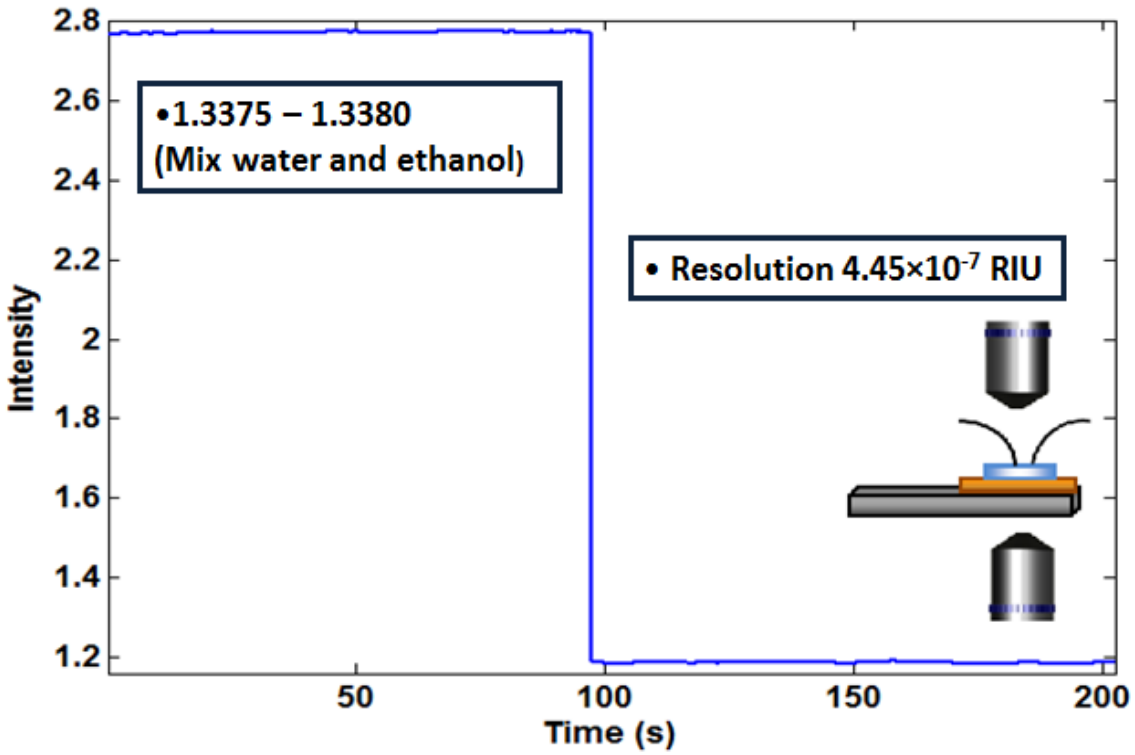

Figure 4.21 Experimental results for measuring the change in intensity at 655 nm wavelength for a 500 nm thick gold film using a laser diode source. An array of circular holes with diameter of 260 nm and periodicity of 570 nm were used.

4.7 Discussion

First we note that good agreement is seen between the simulation and the experiments. The achieved resolution of 4.45×10^{-7} RIU is a promising step towards competing with existing commercial SPR devices (10^{-7} resolution), while allowing for the integration, multiplexing and optofluidic advantages of nanohole SPR.

It is interesting to note that the optimum resolution found from the simulations was around 655 nm. This is believed to result from the gold dispersion for two reasons. First, gold has a low loss at 655 nm because this wavelength is past the interband absorption peak of gold (around 510 nm). Second, the magnitude of the relative permittivity at 655 nm is not too large (it is closer to the plasma frequency than further in the IR, for example), which allows for significant electromagnetic field penetration into the metal

and pronounced plasmonic effects. It is fortuitous that the optimal operation considering the material properties of gold coincides fairly well with the optimal sensitivity of the CCD camera used in this experiment (~600 nm), because this allows for higher photon collection efficiency, and therefore reduced shot-noise signal-to-noise ratio.

It is common to use the SP Bragg relation to determine the optimal periodicity for nanohole array sensing (Equation 2.4). This equation gives reasonable results for predicting the resonance wavelength for thinner films for the lowest order resonance. For example, the $i = 0$, $j = 1$ resonance of the 100 nm film with 425 nm periodicity on the water side is predicted to be 625 nm, and was observed to be 648 nm in the simulations. We see here, however, that larger periodicities are required for thicker films, and these do not seem to match the lowest order resonance. Indeed, they are closer to the $i = 1$, $j = 1$ resonance. The reason for this effect is still under investigation; however, this shows that future investigations should not simply chose the lowest order resonance wavelength as has been done in the past [77].

4.8 Conclusion

We optimized the resolution of circular nanohole arrays in metal films for refractive index sensing by increasing the sensitivity with modifications to the hole-array parameters (film thickness, periodicity and diameter), by determining the optimal wavelength of operation, and by reducing the noise of the sensor system (through increased collection efficiency, increased intensity and numerical filtering). We achieve a bulk resolution of 4.45×10^{-7} RIU. Due to the collinear microscope geometry, the potential for multiplexing of nanohole arrays and improved optofluidic functionality, these results are encouraging for future detection of chemical and biological species. For further improvement larger arrays can be designed to ensure high SNR operation. Bragg reflectors can be used to obtain higher sensitivity and isolate the arrays from crosstalk.

Chapter 5: Conclusions and future work

Periodic nanohole arrays as SPs sensors have the advantages of small footprint for dense integration, simplicity, and a high degree of multiplexing. Despite the several advantages of nanohole arrays as SPs sensors, their sensitivity and resolution are lower compared to conventional SPR devices.

In this work, we optimize the resolution of nanohole arrays in metal films for refractive index sensing by increasing the sensitivity with modifications to the hole-array parameters and by reducing the noise of the sensor system.

In this thesis, it was demonstrated the development of a SP sensor based on the concept of EOT. The sensor made use of nanohole arrays of different periodicities as the sensing element and a laser diode as the light source. A detail discussion on the fabrication of the nanohole arrays using FIB and the integration of a microfluidic chip was provided. An elaborate description of various components of the sensing setup to measure the change due to refractive index has been given in Chapter 4.

We optimized the resolution of circular nanohole arrays in metal films for refractive index sensing by increasing the sensitivity with modifications to the hole-array parameters (film thickness, periodicity and diameter), by determining the optimal wavelength of operation, and by reducing the noise of the sensor system (through increased collection efficiency, increased intensity and numerical filtering). Improvement in resolution of these nanohole sensors was achieved with a fast detector at optimized frame rate. By using spatial summing and temporal averaging the noise components were reduced.

Our results for nanohole arrays sensors have been presented in:

- Gabriela Andrea Cervantes Tellez, Aftab Ahmed, Reuven Gordon, "Optimizing the Resolution of Nanohole Arrays in Metal Refractive Index Sensing", META' 12 Conference, Paris-France (to appear in Applied Physics A).
- Gabriela Andrea Cervantes Tellez, Mandira Das, Reuven Gordon, "Enhanced sensitivity using rectangular nanohole arrays in metal for biosensing applications", 2011 11th IEEE International Conference on Nanotechnology, pp. 126-129.

For a nanohole array sensor a resolution of 10^{-7} RIU is desired in order to compete with commercial SPR sensors like Biacore. Possible improvement in the optical setup and further research in data acquiring techniques can be done. Further improvement in resolution requires the use of Bragg reflectors surrounding the nanohole arrays to eliminate the crosstalk of the nanohole arrays [60].

Bibliography

[1] A. J. deMello and A. T. Woolley, "Nanotechnology," *Current Opinion in Chemical Biology,* vol. 14, pp. 545-7, Oct 2010.

[2] R. H. Ritchie, "Plasma losses by fast electrons in thin films," *Physical Review,* vol. 106, pp. 875-881, 1957.

[3] J. Zhao, X. Zhang, C. R. Yonzon, A. J. Haes, and R. P. Van Duyne, "Localized surface plasmon resonance biosensors," *Nanomedicine,* vol. 1, pp. 219-28, Aug 2006.

[4] A. De Leebeeck, L. K. Kumar, V. de Lange, D. Sinton, R. Gordon, and A. G. Brolo, "On-chip surface-based detection with nanohole arrays," *Analytical Chemistry,* vol. 79, pp. 4094-100, Jun 1 2007.

[5] R. Gordon, D. Sinton, K. L. Kavanagh, and A. G. Brolo, "A new generation of sensors based on extraordinary optical transmission," *Accounts of Chemical Research,* vol. 41, pp. 1049-57, Aug 2008.

[6] K. M. Mayer and J. H. Hafner, "Localized surface plasmon resonance sensors," *Chemical Review,* vol. 111, pp. 3828-57, Jun 8 2011.

[7] K. A. Willets and R. P. Van Duyne, "Localized surface plasmon resonance spectroscopy and sensing," *Annual Review of Physical Chemistry,* vol. 58, pp. 267-97, 2007.

[8] A. V. Zayats, I. I. Smolyaninov, and A. A. Maradudin, "Nano-optics of surface plasmon polaritons," *Physics Reports,* vol. 408, pp. 131-314, 2005.

[9] W. L. Barnes, A. Dereux, and T. W. Ebbesen, "Surface plasmon subwavelength optics," *Nature,* vol. 424, pp. 824-30, Aug 14 2003.

[10] J. Homola, "Surface plasmon resonance sensors for detection of chemical and biological species," *Chemical Review,* vol. 108, pp. 462-93, Feb 2008.

[11] J. Homola, S. Yee, and G. Gauglitz, "Surface plasmon resonance sensors: review," *Sensor and Actuators B,* vol. 54, pp. 3-15, 1999.

[12] A. Otto, "Excitation of nonradiative surface plasma waves in silver by the method of frustrated total reflection," *Zeitschrift fur Physik,* vol. 216, pp. 398-410, 1968.

[13] E. Kretschmann and H. Raether, "Radiative decay of non-radiative surface plasmons excited by light," *Zeitschrift fur Naturforschung Section A* vol. 23, p. 2135, 1968.

[14] L. Novotny and B. Hecht, *Principles of Nano-Optics*: Cambridge University Press, 2006.

[15] J. Homola, H. Vaisocherova, J. Dostalek, and M. Piliarik, "Multi-analyte surface plasmon resonance biosensing," *Methods,* vol. 37, pp. 26-36, Sep 2005.

[16] H. A. Bethe, "Theory of diffraction by small holes," *Physical Review,* vol. 66, pp. 163-182, 1944.

[17] T. W. Ebbesen, H. J. Lezec, H. F. Ghaemi, T. Thio, and P. A. Wolff, "Extraordinary optical transmission through sub-wavelength hole arrays," *Nature,* vol. 391, pp. 667-669, 1998.

[18] C. Genet and T. W. Ebbesen, "Light in tiny holes," *Nature,* vol. 445, pp. 39-46, Jan 4 2007.

[19] K. L. van der Molen, K. J. Koerkamp, S. Enoch, F. B. Segerink, N. F. van Hulst, and L. Kuipers, "Role of shape and localized resonances in extraordinary transmission through periodic arrays of subwavelength holes: Experiment and theory," *Physical Review B,* vol. 72, p. 045421, 2005.

[20] H. F. Ghaemi, T. Thio, D. E. Grupp, T. W. Ebbesen, and H. J. Lezec, "Surface plasmons enhance optical transmission through subwavelength holes," *Physical Review B,* vol. 58, pp. 6779-6782, 1998.

[21] A. Degiron, H. J. Lezec, N. Yamamoto, and T. W. Ebbesen, "Optical transmission properties of a single subwavelength aperture in a real metal," *Optics Communications,* vol. 239, pp. 61-66, 2004.

[22] S. R. Nugen and A. J. Baeumner, "Trends and opportunities in food pathogen detection," *Analytical Bioanalytical Chemistry,* vol. 391, pp. 451-4, May 2008.

[23] B. Cherif, A. Roget, C. L. Villiers, R. Calemczuk, V. Leroy, P. N. Marche, T. Livache, and M. B. Villiers, "Clinically related protein-peptide interactions monitored in real time on novel peptide chips by surface plasmon resonance imaging," *Clinical Chemistry,* vol. 52, pp. 255-62, Feb 2006.

[24] J. A. Lofgren, S. Dhandapani, J. J. Pennucci, C. M. Abbott, D. T. Mytych, A. Kaliyaperumal, S. J. Swanson, and M. C. Mullenix, "Comparing ELISA and surface plasmon resonance for assessing clinical immunogenicity of panitumumab," *Journal of Immunology,* vol. 178, pp. 7467-72, Jun 1 2007.

[25] E. Mauriz, A. Calle, J. J. Manclus, A. Montoya, and L. M. Lechuga, "Multi-analyte SPR immunoassays for environmental biosensing of pesticides," *Analytical Bioanalytical Chemistry,* vol. 387, pp. 1449-58, Feb 2007.

[26] M. A. Cooper, "Optical biosensors in drug discovery," *Nature Review Drug Discovery,* vol. 1, pp. 515-28, Jul 2002.

[27] C. Nylander, B. Liedberg, and T. Lind, "Gas detection by means of surface plasmon resonance," *Sensors and Actuators,* vol. 3, pp. 79-88, 1982.

[28] D. C. Cullen, R. G. Brown, and C. R. Lowe, "Detection of immuno-complex formation via surface plasmon resonance on gold-coated diffraction gratings," *Biosensors,* vol. 3, pp. 211-25, 1987.

[29] J. Homola, I. Koudela, and S. Yee, "Surface plasmon resonance sensors based on diffraction gratings and prism couplers: sensitivity comparison," *Sensors and Actuators B,* vol. 54, pp. 16-24, 1999.

[30] Biacore. *www.biacore.com*.

[31] R. J. Fisher and M. Fivash, "Surface plasmon resonance based methods for measuring the kinetics and binding affinities of biomolecular interactions," *Current Opinion in Biotechnology,* vol. 5, pp. 389-95, Aug 1994.

[32] Y. Yao, B. Yi, J. Xiao, and Z. Li, "Surface plasmon resonance biosensors and its application," *Bioinformatics and Biomedical Engineering, 2007. ICBBE 2007. The 1st International Conference on,* pp. 1043-1046, 2007.

[33] W. L. Barnes, W. A. Murray, J. Ditinger, E. Devaux, and T. W. Ebbesen, "Surface plasmon polaritons and their role in the enhanced transmission of light through periodic arrays of subwavelength holes in metal film," *Physical Review,* vol. 92, p. 107401, 2004.

[34] A. Lesuffleur, H. Im, N. C. Lindquist, K. S. Lim, and S. H. Oh, "Laser-illuminated nanohole arrays for multiplex plasmonic microarray sensing," *Optics Express,* vol. 16, pp. 219-24, Jan 7 2008.

[35] R. Gordon, A. Brolo, D. Sinton, and K. L. Kavanagh, "Resonant optical transmission through hole-arrays in metal films: Physics and applications," *Laser and Photonics Review,* vol. 4, pp. 311-335, 2010.

[36] H. Gao, J. Henzie, and T. W. Odom, "Direct evidence for surface plasmon-mediated enhanced light transmission through metallic nanohole arrays," *Nano Letters,* vol. 6, pp. 2104-8, Sep 2006.

[37] Y. Liu and S. Blair, "Fluorescence enhancement from an array of subwavelength metal apertures," *Optics Letters,* vol. 28, pp. 507-9, Apr 1 2003.

[38] J. Ditinger, S. Klein, and T. W. Ebbesen, "Molecule-surface plasmon interaction in hole arrays: Enhanced absorption, refractive index changes, and all-optical switching," *Advanced Materials,* vol. 18, pp. 1267-1270, 2006.

[39] J. C. Sharpe, J. S. Mitchell, L. Lin, N. Sedoglavich, and R. J. Blaikie, "Gold nanohole array substrates as immunobiosensors," *Analytical Chemistry,* vol. 80, pp. 2244-9, Mar 15 2008.

[40] T. Allsop, R. Neal, E. M. Davies, C. Mou, P. Bond, S. Rehman, K. Kalli, D. J. Webb, P. Calverhouse, and I. Bennion, "Low refractive index gas sensing a surface plasmon resonance fibre device," *Measurement Science and Technology,* vol. 21, p. 094029, 2010.

[41] J. Ji, J. G. O'Connell, D. J. Carter, and D. N. Larson, "High-throughput nanohole array based system to monitor multiple binding events in real time," *Analytical Chemistry,* vol. 80, pp. 2491-8, Apr 1 2008.

[42] X. Shou, A. Agrawal, and A. Nahata, "Role of metal film thickness on the enhanced transmission properties of a periodic array of subwavelength apertures," *Optics Express,* vol. 13, pp. 9834-40, Nov 28 2005.

[43] P. R. Stark, A. E. Halleck, and D. N. Larson, "Short order nanohole arrays in metals for highly sensitive probing of local indices of refraction as the basis for a highly multiplexed biosensor technology," *Methods,* vol. 37, pp. 37-47, Sep 2005.

[44] K. L. Lee, S. H. Wu, and P. K. Wei, "Intensity sensitivity of gold nanostructures and its application for high-throughput biosensing," *Optics Express,* vol. 17, pp. 23104-13, Dec 7 2009.

[45] C. J. Alleyne, A. G. Kirk, R. C. McPhedran, N. A. Nicorovici, and D. Maystre, "Enhanced SPR sensitivity using periodic metallic structures," *Optics Express,* vol. 15, pp. 8163-9, Jun 25 2007.

[46] J. Homola, "Present and future of surface plasmon resonance biosensors," *Analytical Bioanalytical Chemistry,* vol. 377, pp. 528-39, Oct 2003.

[47] T. Akimoto, S. Sasaki, K. Ikebukuro, and I. Karube, "Refractive-index and thickness sensitivity in surface plasmon resonance spectroscopy," *Applied Optics,* vol. 38, pp. 4058-64, Jul 1 1999.

[48] A. Dhawan, M. D. Gerhold, and J. F. Muth, "Plasmonic structures based on subwavelength apertures for chemical and biological sensing applications," *IEEE Sensors Journal,* vol. 8, pp. 942-950, 2008.

[49] F. Eftekhari, C. Escobedo, J. Ferreira, X. Duan, E. M. Girotto, A. G. Brolo, R. Gordon, and D. Sinton, "Nanoholes as nanochannels: flow-through plasmonic sensing," *Analytical Chemistry*, vol. 81, pp. 4308-11, Jun 1 2009.

[50] C. Escobedo, A. G. Brolo, R. Gordon, and D. Sinton, "Flow-through vs flow-over: analysis of transport and binding in nanohole array plasmonic biosensors," *Analytical Chemistry*, vol. 82, pp. 10015-20, Dec 15 2010.

[51] C. Escobedo, A. G. Brolo, R. Gordon, and D. Sinton, "Optofluidic concentration: plasmonic nanostructure as concentrator and sensor," *Nano Letters*, vol. 12, pp. 1592-6, Mar 14 2012.

[52] A. G. Brolo, R. Gordon, B. Leathem, and K. L. Kavanagh, "Surface plasmon sensor based on the enhanced light transmission through arrays of nanoholes in gold films," *Langmuir*, vol. 20, pp. 4813-5, Jun 8 2004.

[53] A. Lesuffleur, H. Im, N. Lindquist, and S. H. Oh, "Periodic nanohole arrays with shape-enhanced plasmon resonance as real-time biosensors," *Applied Physics Letters*, vol. 90, p. 243110, 2007.

[54] L. Pang, G. M. Hwang, B. Slutsky, and Y. Fainman, "Spectral sensitivity of two-dimensional nanohole array surface plasmon polariton resonance sensor," *Applied Physics Letters*, vol. 91, p. 123112, 2007.

[55] K. A. Tetz, L. Pang, and Y. Fainman, "High-resolution surface plasmon resonance sensor based on linewidth-optimized nanohole array transmittance," *Optics Letters*, vol. 31, pp. 1528-30, May 15 2006.

[56] R. Slavik and J. Homola, "Optical multilayers for LED-based surface plasmon resonance sensors," *Applied Optics*, vol. 45, pp. 3752-9, Jun 1 2006.

[57] A. P. Blanchard-Dionne, L. Guyot, S. Patskovsky, R. Gordon, and M. Meunier, "Intensity based surface plasmon resonance sensor using a nanohole rectangular array," *Optics Express*, vol. 19, pp. 15041-6, Aug 1 2011.

[58] C. Escobedo, S. Vincent, A. I. K. Choudhury, J. Campbell, A. Brolo, D. Sinton, and R. Gordon, "Integrated nanohole array surface plasmon resonance sensing device using a dual-wavelength source," *Journal of Micromechanics and Michroengineering*, vol. 21, p. 115001, 2011.

[59] J. C. Yang, J. Ji, J. M. Hogle, and D. N. Larson, "Multiplexed plasmonic sensing based on small-dimension nanohole arrays and intensity interrogation," *Biosensors and Bioelectronics*, vol. 24, pp. 2334-8, Apr 15 2009.

[60] N. C. Lindquist, A. Lesuffleur, H. Im, and S. H. Oh, "Sub-micron resolution surface plasmon resonance imaging enabled by nanohole arrays with surrounding Bragg mirrors for enhanced sensitivity and isolation," *Lab on Chip*, vol. 9, pp. 382-7, Feb 7 2009.

[61] N. Lindquist, A. Lesuffleur, and O. S.H., "Lateral confinement of surface plasmons and polarization-dependent optical transmission using nanohole arrays with a surrounding rectangular Bragg resonator," *Applied Physics Letters*, vol. 91, p. 253105, 2007.

[62] SCK•CEN. Scanning electron microscopy. *http://www.sckcen.be/microstructure/Infrastructure/SEM/Infrastructure_SEM.htm* .

[63] I. Encyclopedia Brittanica. Scanning electron microscope. http://www.britannica.com/EBchecked/media/110970/Scanning-electron-microscope.

[64] H. H. T. Corporation. (2009) Lets familiarize ourselves with the SEM.

[65] IBM. Focussed ion beam. http://www.almaden.ibm.com/st/scientific_services/materials_analysis/fib/

[66] R. Zaouk, B. Y. Park, and M. J. Madou, "Introduction to microfabrication techniques," *Methods in Molecular Biology,* vol. 321, pp. 5-15, 2006.

[67] S. K. Sia and G. M. Whitesides, "Microfluidic devices fabricated in poly(dimethylsiloxane) for biological studies," *Electrophoresis,* vol. 24, pp. 3563-76, Nov 2003.

[68] D. C. Duffy, J. C. McDonald, O. J. Schueller, and G. M. Whitesides, "Rapid Prototyping of Microfluidic Systems in Poly(dimethylsiloxane)," *Analytical Chemistry,* vol. 70, pp. 4974-84, Dec 1 1998.

[69] K. S. Yee, "Numerical solution of initial boundary value problems involving Maxwell's equations in isotropic media," *IEEE Transactions on Antennas and Propagation,* pp. 302-307, 1966.

[70] FDTD. http://docs.lumerical.com/en/fdtd/FDTD_getting_started.pdf.

[71] P. B. Johnson and R. W. Christy, "Optical constants of the noble metals," *Physical Review B,* vol. 6, p. 4370, 1972.

[72] J. Homola, *Surface plasmon resonance based sensors*: Springer, 2006.

[73] M. Piliarik and J. Homola, "Surface plasmon resonance (SPR) sensors: approaching their limits?," *Optics Express,* vol. 17, pp. 16505-17, Sep 14 2009.

[74] CCD noise sources and signal to noise ratio: Concepts of digital imaging technology http://learn.hamamatsu.com/articles/ccdsnr.html.

[75] D. D. and H. P. Noise performance comparison of ICCD with CCD and EMCCD cameras. http://www.stanfordcomputeroptics.com/PDF/5563B-35-spie-apprvd.pdf.

[76] R. K. Verma and B. D. Gupta, "Surface plasmon resonance based fiber optic sensor for the IR region using a conducting metal oxide film," *Journal of Optical Society of America A-Optics Image Science and Vision,* vol. 27, pp. 846-51, Apr 1 2010.

[77] A. Krishnan, T. Thio, T. J. Kim, H. J. Lezec, T. W. Ebbesen, P. A. Wolff, J. Pendry, L. Martin Moreno, and F. J. Garcia Vidal, "Evanescently coupled resonance in surface plasmon enhanced transmission," *Optics Communications,* vol. 200, pp. 1-7, 2001.

Appendix A

Matlab code for taking the spectrum of the nanohole arrays

```
lem=[500:5:780];
t1=10;   % Number of seconds for each wavelength
dlem=lem(1,length(lem))-lem(1);
steps=dlem/5;

fname='array4_spectrumethanol.avi';
info=aviinfo(fname);
fplem=round(info.NumFrames/steps);

for j=1:steps
   for i=10:fplem-10
      a1=aviread(fname,(i+(j-1)*fplem)); %---menos 1
      im1=frame2im(a1);
      b1=double(im1(:,:,1));
      sum1=sum(b1);
      sum2(i)=squeeze(sum(sum1));
   end
   std_eth(j)=std(sum2(1,length(sum2)-15:length(sum2)));
   avgint(j)=mean(sum2);
end

tlem=lem(1,2:length(lem)); %---2
figure;subplot(2,2,1,'fontsize',14);
plot(tlem,avgint,'linewidth',2);
xlabel('Wavelength (nm)');
ylabel('Intensity ethanol');
```

```
t1=10;  %Number of seconds for each wavelength
dlem=lem(1,length(lem))-lem(1);
steps=dlem/5;  %5

skip=2;  %skip the first "skip" frames
fname='array4_spectrum.avi';
info=aviinfo(fname);
fplem=round(info.NumFrames/steps);

for j=1:steps
   for i=10:fplem-10
      a1=aviread(fname,(i+(j-1)*fplem)); %---menos 1
      im1=frame2im(a1);
      b1=double(im1(:,:,1));
      sum1=sum(b1);
      sum3(i)=squeeze(sum(sum1));
   end
   avgint1(j)=mean(sum3);
   std_water(j)=std(sum3(1,length(sum3)-15:length(sum3)));
end
tlem=lem(1,2:length(lem)); %---2
subplot(2,2,2,'fontsize',14);
plot(tlem,avgint1,'red','linewidth',2);
xlabel('Wavelength (nm)');
ylabel('Intensity water');
d=avgint1-avgint;

subplot(2,2,3,'fontsize',14);
plot(tlem,abs(d),'linewidth',2);
xlabel('Wavelength (nm)');
ylabel('Difference water and ethanol');
```

```
subplot(2,2,4,'fontsize',14);
plot(tlem,avgint1,'red','linewidth',2);
hold on;
plot(tlem,avgint,'linewidth',2);
xlabel('Wavelength (nm)');
ylabel('Intensity water and ethanol');
```

Appendix B

Spectrum of different nanohole arrays (experimental results)

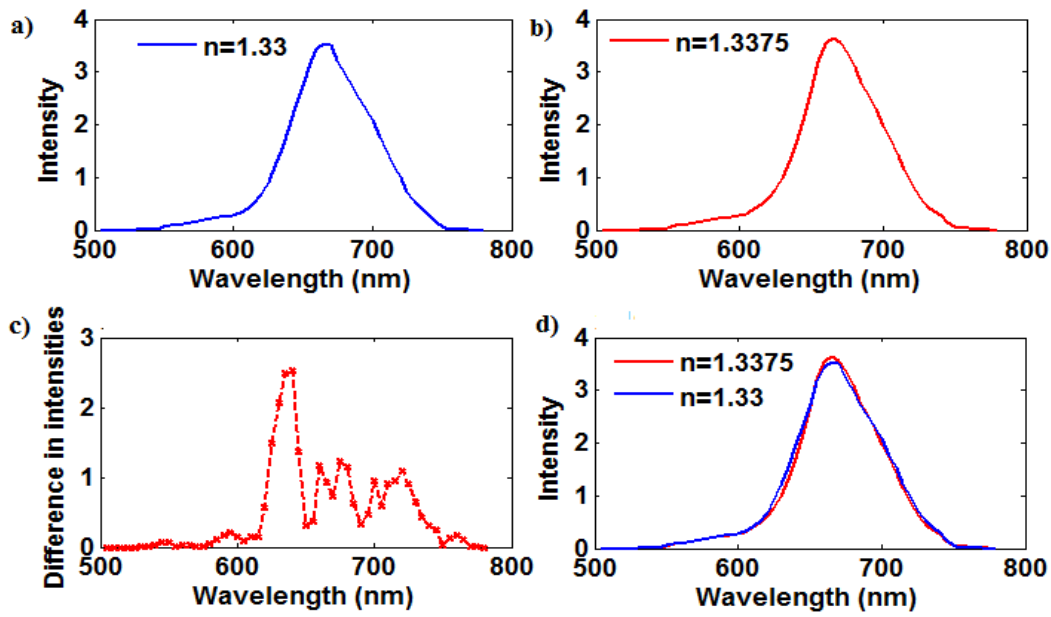

Figure B.1 Spectrum of a circular nanohole array with a diameter of 240 nm in a 500 nm thick gold film for two different refractive index solutions.

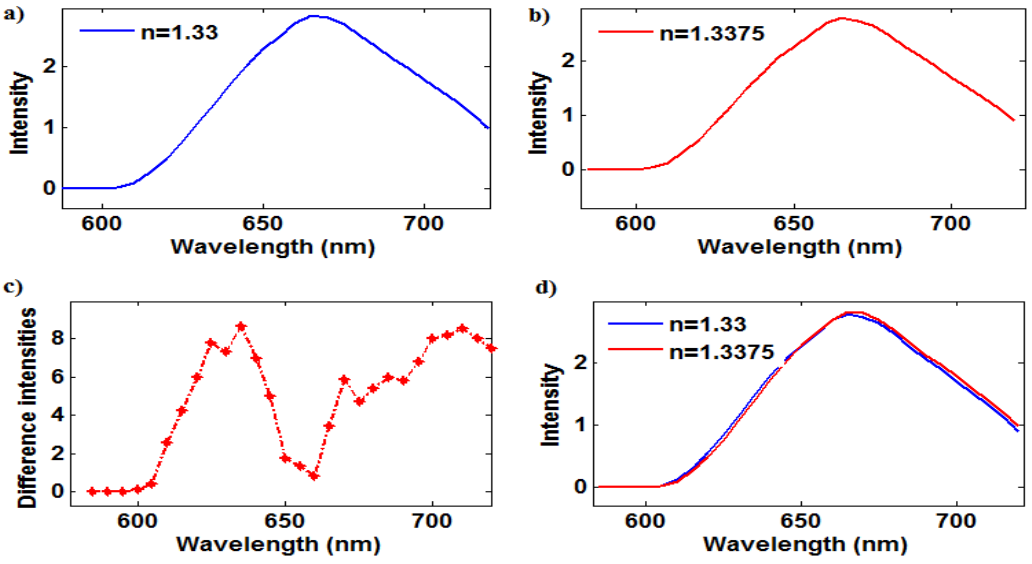

Figure B.2 Spectrum of a circular nanohole array with a diameter of 250 nm in a 300 nm thick gold film for two different refractive index solutions.

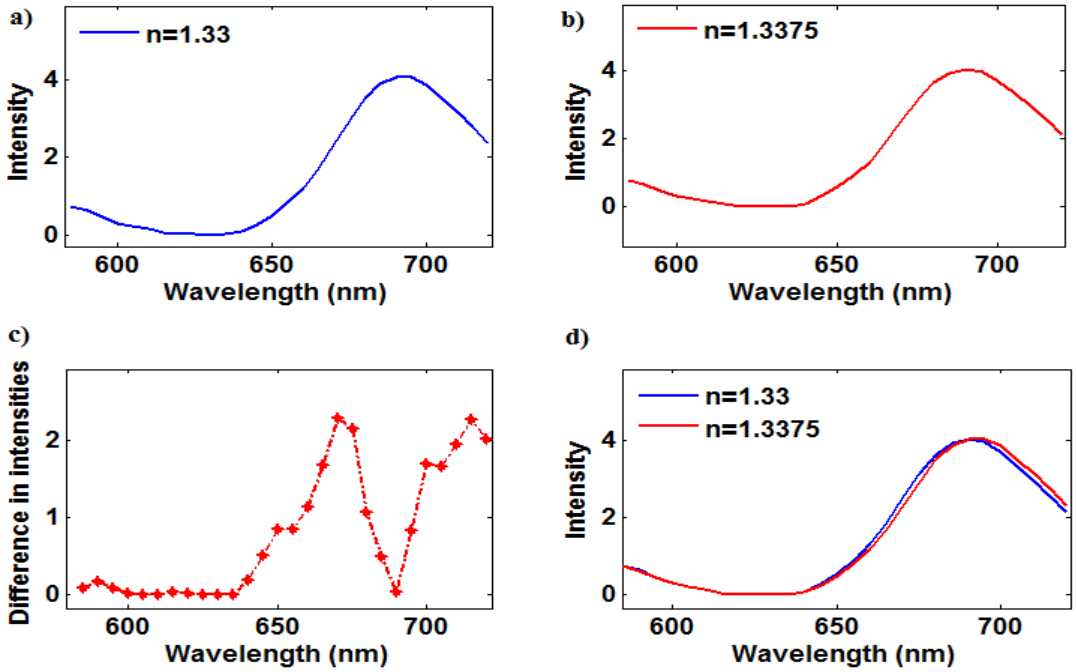

Figure B.3 Spectrum of a circular nanohole array with a diameter of 250 nm in a 500 nm thick gold film for two different refractive index solutions.

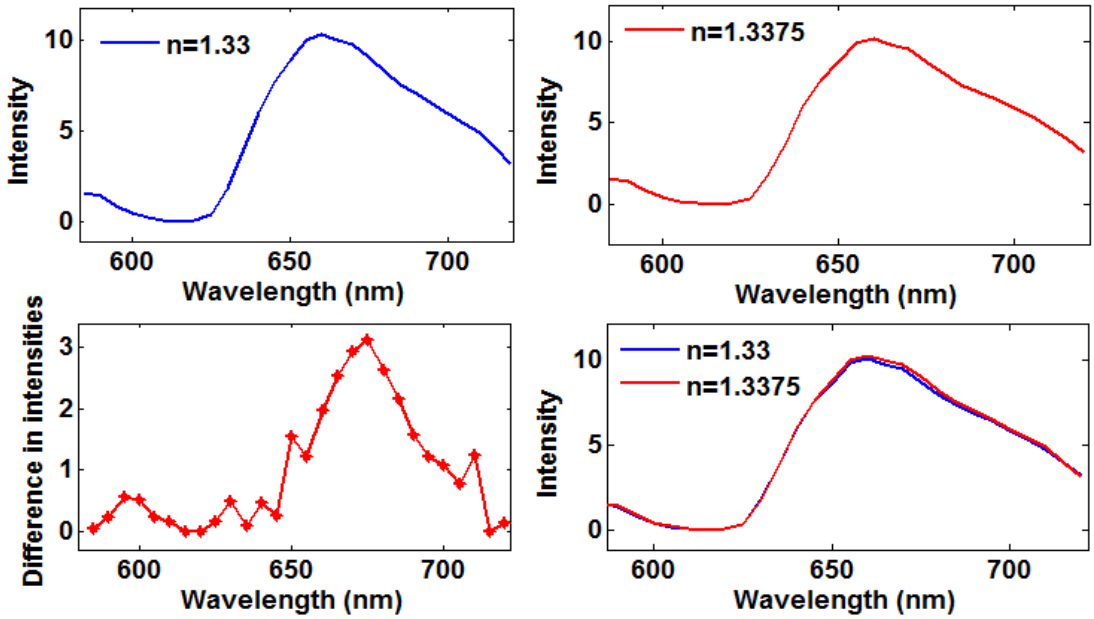

Figure B.4 Spectrum of a circular nanohole array with a diameter of 210 nm in a 100 nm thick gold film for two different refractive index solutions.

Appendix C

Matlab code for taking the intensity of a nanohole array from a video

```
fileinfo=aviinfo('13385_13394_51_r4.avi');

N=1;  %Number of frames to be added
k=1;  % Number of frames being skipped
for i=k:k:fileinfo.NumFrames
   a1=aviread('13385_13394_51_r4.avi',i);
   im1=frame2im(a1);
   b1=double(im1(:,:,1));
   sum1=sum(b1);
   int(i/k)=sum(sum1);
end
%------------------- Before filtering ----------------
pause;
p1=201:1300;
p2=8801:9900;

bef1=int(1,p1);
aft1=int(1,p2);
intbf=[bef1 aft1];
bstd1=std(bef1);
astd1=std(aft1);

bm1=mean(bef1);
am1=mean(aft1);
dn=1.3394-1.3385;

dm1=bm1-am1;
```

```
SNR1=(dm1)/((bstd1+astd1)/2);
r1=dn/SNR1;

figure(1);
subplot(1,2,1,'fontsize',14);
plot([1:length(intbf)-599]*1,intbf(1,300:length(intbf)-300),'linewidth',2);
title(['before filtering, R=',num2str(r1)]);
%------ Fir kaiser --------
fpr=fileinfo.FramesPerSecond;  %Sampling f
N    = 250;        % Order
wcut=.005;       %Cut off
Beta = 0.5;        % Window Parameter
% Create the window vector for the design algorithm.
win = kaiser(N+1, Beta);
% Calculate the coefficients using the FIR1 function.
b = fir1(N, wcut, 'low', win);
Hd = dfilt.dffir(b);
figure;freqz(b,1);

temp2=filter(b,1,bef1);  % FIR linear phase
temp3=filter(b,1,aft1);

bef2=temp2(1,300:length(temp2));
aft2=temp3(1,300:length(temp3));
intaf=[bef2 aft2];

bstd2=std(bef2);
astd2=std(aft2);
bm2=mean(bef2);
am2=mean(aft2);
```

```
dn=1.3394-1.3385;
dm2=bm2-am2;
SNR2=(dm2)/((bstd2+astd2)/2);
r2=dn/SNR2;
%----------- Plotting results ----------
time=[1:length(intbf)];
figure(1);
subplot(1,1,1,'fontsize',14);
plot(time,intbf,'linewidth',2);
title(['R=',num2str(r1)]);
xlabel('No of samples');
ylabel('Intensity');
```